PRIMA DDL & AOS Project

ARC
EPFL
CSEM
MPIA Heidelberg
Observatoire de Genève
Landessternwarte Heidelberg

Astrometric Survey for Extra-Solar Planets with PRIMA

Astrometric Error Budget

Doc. No. VLT-TRE-AOS-15753-0001
Issue 1.2.039
Date February 8, 2007

Prepared	Robert N. Tubbs, Richard J. Mathar	February 8, 2007	Signature
Approved	Denis Mégevand	February 8, 2007	Signature
Released	Didier Queloz	February 8, 2007	Signature

Change Record

Issue	Date	Contents affected	Reason / Initiation / Documents / Remarks
0.1	7-Sep-2004	all	created (rnt)
0.11	18-Nov-2004	1, 15, 21	minor additions concerning baseline definitions (rnt)
0.12.028	28-Jan-2005	all	removed some empty sections and references to these (rjm)
0.8.067	8-Mar-2005		issue number 0.12.067→0.8.067 to realign with PDR list (rjm)
0.95.116	26-Apr-2005		issue 0.9.116→0.95.116 to realign with PDR list (rjm)
0.99.130	10-May-2005		secondary issue number increased for PDR (rjm)
1	17-May-2005	Sec. 1.7	temporarily for PDR: full titles and dates(rjm)
1.1.160	9-Jun-2006	Fig. 49	updated (rjm)
		Sec. 3.2.1	added 2 ABCD equations (rjm)
1.1.162	11-Jun-2006	Ref. [170]	added (rjm)
1.1.177	26-Jun-2006	Fig. 39	added (rjm)
1.1.179	28-Jun-2006	Sec. 18.4	added (rjm)
1.1.185	4-Jul-2006	Sec. 21.3	added Ref [164] (rjm)
1.1.186	5-Jul-2006	Tab. 1	removed entry for effective star color (rjm)
1.1.227	15-Aug-2006	Sec. 26.4	added remark on field angles (rjm)
		Ref. [123]	added
1.1.230	18-Aug-2006	Ref. [77, 97]	added (rjm)
1.1.243	31-Aug-2006	Fig. 46	added (rjm)
		Fig. 39	extended plotting range (rjm)
1.1.264	21-Sep-2006	Fig. 49	updated (rjm)
1.1.267	24-Sep-2006	Fig. 46	replotted (rjm)
1.1.270	27-Sep-2006	Ref. [28, 48, 83, 146]	added (rjm)
1.1.272	29-Sep-2006	Tab. 3	added (rjm)
1.1.274	1-Oct-2006	Ref. [17, 122]	added (rjm)
1.1.275	2-Oct-2006	Ref. [178]	added (rjm)
1.1.277	4-Oct-2006	Fig. 26	added (rjm)
1.1.303	30-Oct-2006	Ref. [194]	added (rjm)
1.2.021	21-Jan-2007	Ref. [10]	added (rjm)
1.2.039	8-Feb-2007	Figs. 35,36	changed 1.0m to 1.8m diameter (rjm)

Contents

List of Figures

List of Tables

1 OVERVIEW

1.1 Scope of the Document

This represents a first overview of an error budget for PRIMA narrow angle astrometry. Only a few error terms are discussed. The definition of "error" encompasses any variable related to the physical environment, hardware and software which reduces the capability to deduce astrometric angles [78, 171]. Here, even terms that would be prime targets for astrophysical research on their own (Sections 30 and 31) qualify as errors, as well as any intrinsic property of the atmosphere which hardly would be called an "error" in lawyer's terms.

Errors can be classified as representing zero-mean variables that stress the instrument performance with respect to efficiency and limiting magnitude; others less gently introduce biases/drifts and call for "active" correction. Most of the variables related to turbulence are of the first kind, but may create residuals of the second kind if they are forced through filters in time, space or frequency.

A generic problem of this astrometric error budget is to detail what could be phrased as "putting error bars on the entries of variance matrices:" the layout of hardware and software (including the calibration procedures) is keen to be differential in as many dimensions as possible. This capability of reducing and subtracting some "obvious" or "known" first-order errors leaves behind the hard errors which evade precise modeling or blind, short-term statistical averaging. Putting price tags on some of those is equivalent to modeling the VLTI, the earth, the universe and everything beyond, and not in the scope of this document. An unavoidable side effect of the inter-opration of the physical effects is that errors of these higher order differentials are only evident if *all* these expansion parameters have been assigned their values. A prototypical example are the residuals of the PRIMET wavelength transformation after the horizontal temperature and/or humidity gradients have been cancelled by looking at results of beam-swapped operations: these are expressed as the triple product of the OPD by the sum over the individual contributions from horizontal temperature and humidity gradients by their change in time during the beam swap. A second example: The only correct answer to the question whether an error of 5 nm is equivalent to a (systematic) error of 10 μas in the star separation is: "it depends."—Both variables only become coupled if they refer to some specific baseline length and some specfic angle between the star separation vector and the plane of the projected baseline (Fig. 47).

In fulfillment of AI #5 of [41], the summary and the table in it have been moved from the last up to the early Section 2. The top worries list has also been compiled in [152]. As requested by AIs #1 and #2 of the PDR [41], additional summaries have been spawned in [116] and [117]. One intrinsic side effect of such spreading of information is that overview will be lost.

This text is available at the URLs `http://www.strw.LeidenUniv.nl/~mathar/public/mathar15753-0001.pdf` and `http://obswww.unige.ch/Instruments/PRIMA/documentation/documentation.html`.

1.2 Work Breakdown

The margins between errors that allow the instrument to work within specified requirements or not to reach these goals can be specified in terms of the pair angle on the sky, and then be broken down to three derived master parameters (which are differential delay, baseline length and global sky position, Eq. (59)). A specification of 10 μas accuracy on the differential angle on the sky has been given in [40, p. 14], a goal of 10 nm in the differential OPD on page 24 and Table 5–8 of [40]. Requirements on the fringe tracking or the imaging mode of PRIMA are not necessarily relevant to the astrometric mode; in fact, the requirements on faint star tracking on one hand and accurate astrometry on the other seem to lead to different requests of spectral resolution in the FSU.

Judiciously, the astrometric mode is complementary to other modes of the same instrument, and also complementary to other VLTI instruments: Determination of visibilities is of no importance in the astrometric mode; small visibilities are indicative of smaller S/N and effect the accuracy of the phase measurements indirectly. The native astrometric mode requires both stars to be unresolved, otherwise the definition of the "observed" star positions themselves becomes fuzzy. (The astrometric mode is *not* meant to measure the distance of two objects of 50 μas in diameter to 10 μas accuracy. . .)

1.3 Critical Issues

1. The definition of the baseline relevant for narrow-angle astrometry observations. This is defined by an image of the field selector mirror, situated in the STS. The location, tilt and curvature of this image and the corresponding image plane of the stellar beams are crucial to the baseline determination. This model of the dual-beam interferometer is re-defined here to the conceptually more simple problem of monitoring the equivalent change in the intermediate stretch of optical path length accumulation between the entrance pupil until arrival on the actual mirror.
2. Numerical simulations indicate that wavefront corrugations across the telescopes may make fringe tracking very difficult with the PRIMA FSUs (see Section 27).
3. The dependence of the spectral sensitivity of PRIMA on the seeing conditions due to the effect of spatial filtering, will have to be studied in detail. A standard model of the FSU spatial filters predicts strong sensitivity to the seeing (see Section 21).

1.4 Identified show-stoppers

Any of the items listed in Section 1.3 could be a show-stopper.

1.5 Tools and Technologies Required

The critical issues primary involve the effects of wavefront corrugations across the aperture plane, so tools will have to be developed to investigate these in detail.

The dependence of the phase output in the two beams in STS calibration mode on atmospheric seeing and refraction effects has been the fundamental calibration for PRIMA astrometry. A brief discussion is included in Sections 4 and 6. This calibration mode of placing a single star in the middle of M10 of the STS produces complicated diffraction patterns and phase screens across the pupil (Figs. 13 and 16) which will unlikely generate a smooth "first order" OPD signal at transit from one side of M10 to the other. The change in the appropriate observing strategy is to use the derotator to move the calibrator from one position to the symmetrical opposite position on the other face and define the metrology zero as the algebraic mean at these positions.

1.6 Questions and Requests

Further details of the design of the FSUs (spectral sensitivity, fringe tracking algorithms etc), the STS (optical quality, sharpness of roof mirror etc) and the STRAP units (Strehl ratio performance, power spectra of tip-tilt jitter etc) will be essential in producing a more realistic error budget.

1.6.1 Review Item Comment

Considering that the astrometric mode will be almost exclusively run on ATs, we mention that

- the apertures of the FSU optics [19, p 48] consider laboratory angles derived from UT, not AT magnification factors,
- fringe tracking algorithms have been previously examined for UTs equipped with AO [63], not for ATs,
- fluxes assumed for FSU development [127, Tab. 1] refer to UT's, not ATs.

1.6.2 Review Item Question

1. Will the metrology readings stored in the acsFITS files [58] have been corrected with respect to the finite-beam diameter effect described in Section 18.1?
2. Within which FOV does the Coudé table and guiding software allow off-axis tracking that would help to build an OPD map of the AT optics as a function of the tip/tilt of the incoming light?
3. Will the metrology system loose lock if a fast sweep (including the corresponding pace of the VLTI DL) is used to hop to another reference star during baseline calibration (as opposed to standard tracking velocities of some cm/s)?

1.7 References

[1] Abramowitz, M., and I. A. Stegun (eds.), 1972, *Handbook of Mathematical Functions* (Dover Publications, New York), 9th edition, ISBN 0-486-61272-4.

[2] Aime, C., J. Borgnino, F. Martin, R. Petrov, and G. Ricort, 1986, J. Opt. Soc. Am. A **3**, 1001.

[3] Alenia SPAZIO, 2003, *Fringe Sensor Unit, Final Design Review*, Technical Report.

[4] Altarac, S., P. Berlioz-Arthaud, E. Thiébaut, R. Foy, Y. Y. Balega, J. C. Dainty, and J. J. Fuensalida, 2001, Month. Not. Roy. Astron. Soc. **322**(1), 141.

[5] AMOS, 2003, *ATS*, VLT-TRE-AMO-151100-092.

[6] Andolfato, L., and R. Karban, 2003, *VLTI PRIMA Fringe Sensor Unit Control Software Requirements Specification (Workstation)*, VLT-SPE-ESO-15736-3115.

[7] Andolfato, L., and R. Karban, 2003, *VLTI PRIMA FSU Instrument Software Requirements Description*, VLT-SPE-ESO-15736-3179.

[8] Andolfato, L., and R. Karban, 2005, *VLTI PRIMA Supervisor Software Interface Control Document*, VLT-ICD-ESO-15736-3060.

[9] Andolfato, L., and R. Karban, 2006, *VLTI PRIMA Star Separator Control Software, System Design Description*, VLT-SPE-ESO-15736-3186.

[10] Anglada-Escudé, G., S. A. Klioner, M. Soffel, and J. Torra, 2007, Astron. Astrophys. **462**, 371.

[11] Argomedo, J., 2004, *Auxiliary Telescopes Operation Quick Reference*, VLT-MAN-ESO-10200-3441.

[12] Arguijo, P., and M. S. Scholl, 2003, Appl. Opt. **42**(16), 3284.

[13] Bahethi, O. P., and R. S. Fraser, 1980, Appl. Opt. **19**(8), 1323.

[14] Bauvier, B., 2006, *VLT, FINITO Piezo Fiber Modulator, Control Software Detailed Design*, VLT-SPE-ESO-15430-2788.

[15] Bauvir, B., and H. Bonnet, 2006, *VLT, FINITO Beam Acquisition and Stabilization Technical Specification*, VLT-SPE-ESO-15430-4021.

[16] Beck, C., R. Schlichenmaier, M. Collados, L. B. Rubio, and T. Kentischer, 2005, Astron. Astrophys. **443**(3), 1047.

[17] Berton, R. P. H., 2006, J. Opt. A: Pure Appl. Opt. **8**(10), 817.

[18] Boehm, J., and H. Schuh, 2003, in *16th Working Meeting on European VLBI for Geodesy and Astrometry*, edited by W. Schwegmann and V. Thorandt (Bundesamt für Kartographie und Goedäsie), volume 16, pp. 131–143.

[19] Bogo, W., A. Busso, S. Mottini, G. Nicolini, and G. Massone, 2003, *PRIMA FSU, Design and analysis report*, VLT-TRE-ALS-15740-0004. The abscissa units in Fig 4.3-11 should be μm, not nm.

[20] Bonaccini, D., W. Hackenberg, and L. Taylor, 2003, The Messenger **114**, 15.

[21] Bos, M. S., and H.-G. Scherneck, 2005, The free ocean tide loading provider, URL `http://www.oso.chalmers.se/~loading`.

[22] Brasunas, J. C., 2002, Appl. Opt. **41**(13), 2481.

[23] Bruce, C. F., 1955, Aus. J. Phys. **8**(2), 224.

[24] Buscher, D., 1988, Month. Not. Roy. Astron. Soc. **235**, 1203.

[25] Buscher, D. F., 1988, *Getting the most out of C.O.A.S.T.*, Ph.D. thesis, Cambridge University.

[26] Capitaine, N., P. T. Wallace, and J. Chapront, 2005, Astron. Astrophys. **432**(1), 355.

[27] Capitaine, N., P. T. Wallace, and D. D. McCarthy, 2003, Astron. Astrophys. **406**(3), 1135.

[28] Cavagnero, G., G. Mana, and E. Massa, 2006, J. Opt. Soc. Am. A **23**(8), 1951.

[29] Chang, M. P. J. L., and D. F. Buscher, 1998, in *Astronomical Interferometry*, edited by R. D. Reasenberg (Int. Soc. Optical Engineering, Kona), volume 3350 of *Proc. SPIE*, pp. 2–13.

[30] Chang, S., and A. Prata, 2005, J. Opt. Soc. Am. A **22**(11), 2454.

[31] Chiozzi, G., P. Duhoux, and R. Karban, 2001, *AT Control Software, Requirements Specification*, VLT-SPE-ESO-15151-1712.

[32] Conan, R., A. Ziad, J. Borgnino, F. Martin, and A. Tokovinin, 2000, in *Interferometry in Optical Astronomy*, edited by P. J. Lena and A. Quirrenbach (Int. Soc. Optical Engineering), volume 4006 of *Proc. SPIE*, pp. 963–973.

[33] Cresci, G., R. I. Davies, A. J. Baker, and M. D. Lehnert, 2005, Astron. Astrophys. **438**(2), 757.

[34] Dai, G.-m., 1995, J. Opt. Soc. Am. A **12**(10), 2182.

[35] Daigne, G., and J.-F. Lestrade, 2003, Astron. Astrophys. **406**(3), 1167.

[36] d'Arcio, L., 1995, *Differential anisoplanatic OPDs and OPD spectra for the VLTI at Cerro Paranal from PARSCA 1992 Balloon Data*, VLT-TRE-ESO-15000-0835.

[37] D'Arcio, L. A., 1999, *Selected aspects of wide-field stellar interferometry*, Ph.D. thesis, Technische Universiteit Delft.

[38] Davis, J., and A. Richichi, 2003, *The Spectral Sensitivity Curve and Effective Wavelength for the VLTI with VINCI*, VLT-TRE-ESO-15810-3033.

[39] Delabre, B., 1992, *Specification for the optical layout of the VLT Auxiliary Telescopes*, VLT-SPE-ESO-15100-0299.

[40] Delplancke, F., 2003, *PRIMA, the Phase Referenced Imaging and Microarcsecond Astrometry facility: High Level Requirements & System Description*, VLT-SPE-ESO-15700-3051.

[41] Delplancke, F., 2005, *Minutes of Meeting, PAOS Preliminary Design Review*, TSD-05/42.

[42] Delplancke, F., S. Lévêque, P. Kervella, A. Glindemann, and L. d'Arcio, 2000, in *Interferometry in Optical Astronomy*, edited by P. J. Lena and A. Quirrenbach (Int. Soc. Optical Engineering), volume 4006 of *Proc. SPIE*, pp. 365–376.

[43] Di Folco, E., B. Koehler, P. Kervella, M. Sarazin, V. Coudé du Foresto, M. Schöller, and M. Wittkowski, 2003, in *Interferometry for Optical Astronomy II*, edited by W. A. Traub (Int. Soc. Optical Engineering), volume 4838 of *Proc. SPIE*, pp. 1115–1126.

[44] Dimmler, M., 2004, *AT#1 Commissioning: Tracking, Test Report*, VLT-TRE-ESO-15000-3465.

[45] Duhoux, P., 2001, *VLT Software - CCS-LCU Time Interface Module Driver User Manual*, VLT-MAN-ESO-17210-0431.

[46] Duhoux, P., 2003, *VLTI PRIMA Metrology control software System Design Description*, VLT-SPE-ESO-15736-2998.

[47] Dyer, S. D., and D. A. Christensen, 1999, J. Opt. Soc. Am. A **16**(9), 2275.

[48] Énard, D., 1991, J. Optics (Paris) **22**(2), 33.

[49] Felkel, R., 2005, Kompensation der atmosphärischen turbulenz in einer optischen antennengruppe.

[50] Femenía, B., M. Carbillet, S. Esposito, and A. Riccardi, 2000, in *Interferometry in Optical Astronomy*, edited by P. J. Lena and A. Quirrenbach (Int. Soc. Optical Engineering), volume 4006 of *Proc. SPIE*, pp. 1116–1127.

[51] Ferrari, M., 1997, *VCM Pupil Transfer Inside the Delay Line Cat's Eye*, VLT-TRE-ESO-15220-1509.

[52] Ferrari, M., and F. Derie, 1998, in *Astronomical Interferometry*, edited by R. D. Reasenberg (Int. Soc. Optical Engineering, Kona), volume 3350 of *Proc. SPIE*, pp. 830–838.

[53] Ferrari, M., G. Lemaître, S. Mazzanti, P. Lanzoni, F. Derie, P. Gitton, and S. Ménardi, 2000, in *Interferometry in Optical Astronomy*, edited by P. J. Lena and A. Quirrenbach (Int. Soc. Optical Engineering), volume 4006 of *Proc. SPIE*, pp. 104–115.

[54] Flebus, C., P. Gloesener, O. Pirnay, N. Ninane, and B. Koehler, 2003, in *Interferometry for Optical Astronomy II*, edited by W. A. Traub (Int. Soc. Optical Engineering), volume 4838 of *Proc. SPIE*, pp. 759–773.

[55] Folco, E. D., and B. Koehler, 2002, *VLTI Commissioning Part I: OPD stability, Test Report*, VLT-TRE-ESO-15000-2902.

[56] Folgueira, M., and J. Souchay, 2005, Astron. Astrophys. **432**, 1101.

[57] Fomalont, E. B., 2004, arXiv:astro-ph/0404080 .

[58] Frahm, R., 2004, *VLTI PRIMA Metrology Control Software, Detailed Design Description*, VLT-SPE-ESO-15736-3384.

[59] Fried, D. L., 1965, J. Opt. Soc. Am. **55**(11), 1427, E: [60].

[60] Fried, D. L., 1966, J. Opt. Soc. Am. **56**(3), 410E.

[61] Fusco, T., G. Rousset, D. Rabaud, E. Gendron, D. Mouillet, F. Lacombe, G. Zins, P.-Y. Madec, A.-M. Lagrange, J. Charton, D. Rouan, N. Hubin, *et al.*, 2004, J. Opt. A **6**, 585.

[62] Gai, M., 2001, *FINITO Overall description*, VLT-SPE-OAT-15430-0001.

[63] Gai, M., 2004, PRIMA FSU—effects of residual atmospheric turbulence on GD measurement, WN041210.

[64] Galliano, E., M. Schöller, M. Fischer, C. Hummel, S. Morel, F. Rantakyrö, and M. Vannier, 2004, in *New Frontiers in Stellar Interferometry*, edited by W. A. Traub (Int. Soc. Optical Engineering), volume 5491 of *Proc. SPIE*, pp. 1540–1548.

[65] Ganci, S., 1996, J. Mod. Opt. **43**(12), 2543.

[66] García-Lorenzo, B., J. J. Fuensalida, C. Muñoz-Tuñon, and E. Mendizabal, 2005, Month. Not. Roy. Astron. Soc. **356**, 849.

[67] Gerrard, A., and J. M. Burch, 1975, *Introduction to Matrix Methods in Optics* (John Wiley).

[68] Gitton, P., 2003, *VLTI Commissioning Part II: Effect of internal optical path on UT image stability, Test Report*, VLT-TRE-ESO-15000-3083.

[69] Gitton, P., M. Cantzler, B. Koehler, and P. Kervella, 2003, in *Interferometry for Optical Astronomy II*, edited by W. A. Traub (Int. Soc. Optical Engineering), volume 4838 of *Proc. SPIE*, pp. 1182–1192.

[70] Gitton, P., B. Koehler, S. Lévêque, and A. Glindemann, 2000, in *Astronomical Telescopes and Instrumentation: Ground-Based Telescopes*, edited by W. A. Traub (Int. Soc. Optical Engineering), volume 4004 of *Proc. SPIE*, pp. 222–245.

[71] Gitton, P., S. Lévêque, G. Avila, and T. P. Duc, 2004, in *New Frontiers in Stellar Interferometry*, edited by W. A. Traub (Int. Soc. Optical Engineering), volume 5491 of *Proc. SPIE*, pp. 944–953.

[72] Gitton, P., R. Wilhelm, A. Glindemann, and F. Paresce, 2003, *Determination of the field and pupil rotation in the VLTI laboratory*, VLT-TRE-ESO-15000-3092.

[73] Goldberg, K. A., and J. Bokor, 2001, Appl. Opt. **40**(17), 2886.

[74] Gorham, P. W., 1998, in *Astronomical Interferometry*, edited by R. D. Reasenberg (Int. Soc. Optical Engineering, Kona), volume 3350 of *Proc. SPIE*, pp. 116–127.

[75] Guyon, O., 2002, Astron. Astrophys. **387**(1), 366.

[76] Hardin, R. H., N. J. A. Sloane, and W. D. Smith, 1997, Tables of spherical codes, URL `http://www.research.att.com/~njas/packings/`.

[77] Hirt, C., 2006, Astron. Astrophys. **459**(1), 283.

[78] Hog, E., and P. K. Seidelmann (eds.), 1995, *Astronomy and Astrophysics objectives of submilliarcsecond optical astrometry*, volume 166 of *IAU Symposium* (Kluwer, Dordrecht).

[79] Hrynevych, M. A., E. R. Ligon, and M. M. Colavita, 2004, in *New Frontiers in Stellar Interferometry*, edited by W. A. Traub (Int. Soc. Optical Engineering), volume 5491 of *Proc. SPIE*, pp. 1649–1660.

[80] Huxley, A., 2004, *Seismic Monitoring System, Software Design and User Manual*, VLT-MAN-ESO-17441-3044.

[81] Innocenti, C., and A. Consortini, 2005, J. Mod. Opt. **52**(5), 671.

[82] Johnston, K. J., and C. de Vegt, 1999, Annu. Rev. Astron. Astrophys. **37**, 97.

[83] Junchang, L., C. Vialle, and J. Merlin, 1993, J. Optics (Paris) **24**(5), 193.

[84] Kaplan, G. H., 2006, arXiv:astro-ph/0602086 .

[85] Karban, R., and K. Wirenstrand, 2004, *AT#1 Commissioning: Chopping, Test Report*, VLT-TRE-ESO-15100-3466.

[86] Karban, R., and K. Wirenstrand, 2004, *AT#1 Commissioning: Pointing, Test Report*, VLT-TRE-ESO-15100-3464.

[87] Karban, R., and K. Wirenstrand, 2005, *AT#2 Commissioning: Chopping, Test Report*, VLT-TRE-ESO-15100-3586.

[88] Karban, R., and K. Wirenstrand, 2005, *AT#2 Commissioning: Pointing, Test Report*, VLT-TRE-ESO-15100-3584.

[89] Keen, J. W., D. F. Buscher, and P. J. Warner, 2001, Month. Not. Roy. Astron. Soc. **326**(4), 1381.

[90] Khristoforova, M., 2003, *Analysis of VINCI Photometric Data for the estimation of atmospheric parameters*, VLT-TRE-ESO-15810-3070.

[91] Koehler, B., M. Kraus, J. M. Moresmau, K. Wirenstrand, M. Duchateau, P. Duhoux, R. Karban, C. Flebus, E. Gabriel, and O. Pirnay, 2004, in *New Frontiers in Stellar Interferometry*, edited by W. A. Traub (Int. Soc. Optical Engineering), volume 5491 of *Proc. SPIE*, pp. 600–610.

[92] Koehler, B., S. Lévêque, and P. Gitton, 2003, in *Interferometry for Optical Astronomy II*, edited by W. A. Traub (Int. Soc. Optical Engineering), volume 4838 of *Proc. SPIE*, pp. 846–857.

[93] Köhler, R., J. A. de Jong, S. Reffert, and W. J. Jaffe, 2005, *Astrometric Survey for Extra-Solar Planets with PRIMA, Data Reduction System, Specifications*, VLT-TRE-AOS-15752-0002.

[94] Kolmogorov, A. N., 1941, Comptes rendus (Doklady) de l'Académie des Sciences de l'U.R.S.S. **32**, 16.

[95] Kolmogorov, A. N., 1941, Comptes rendus (Doklady) de l'Académie des Sciences de l'U.R.S.S. **30**, 301.

[96] Lambert, S., 2003, *Analyse et modelisation de haute precision pour l'orientation de la terre*, Ph.D. thesis, L'Observatoire de Paris.

[97] Lambert, S. B., 2006, Astron. Astrophys. **457**(2), 717.

[98] Lane, B. F., and M. M. Colavita, 2003, Astron. J. **125**(3), 1623.

[99] Lane, B. F., and M. W. Muterspaugh, 2004, arXiv:astro-ph/0407280 .

[100] Lane, B. F., and M. W. Mutterspaugh, 2004, in *New Frontiers in Stellar Interferometry*, edited by W. A. Traub (Int. Soc. Optical Engineering), volume 5491 of *Proc. SPIE*, pp. 47–55.

[101] Launhardt, R., 2005, *Dispersion in DDL vacuum windows*, MPIA-TRE-DDL-15722-0003.

[102] Launhardt, R., S. Frink, D. Segransan, and J. Setiawan, 2003, *Astrometric survey for extra-solar planets with PRIMA: Scientific proposal*, Planets-PRI-SCI-0001.

[103] LeBouquin, J.-B., 2005, *Imagerie par synthèse d'ouverture optique, application aux étoiles chimiquement particulières*, Ph.D. thesis, Université Joseph Fourier - Grenoble I.

[104] LeBouquin, J.-B., P. Labeye, F. Malbet, L. Jocou, F. Zabihian, K. Rousselet-Perraut, J.-P. Berger, A. Delboulbé, P. Kern, A. Glindeman, and M. Schöller, 2006, Astron. Astrophys. **450**(3), 1259.

[105] Lévêque, S., 2000, *Results of environmental tests for the VLTI at Paranal, May 11–21/00*, VLT-TRE-ESO-15000-2259.

[106] Lévêque, S., and B. Koehler, 1998, in *Astronomical Interferometry*, edited by R. D. Reasenberg (Int. Soc. Optical Engineering, Kona), volume 3350 of *Proc. SPIE*, pp. 380–388.

[107] Lévêque, S., Y. Salvadé, R. Wilhelm, and D. Rabeling, 2002, *PRIMA Metrology Test Campaign 27/4/02 to 5/5/02*, VLT-TRE-ESO-15730-2827.

[108] Lewis, A. J., 1993, *Absolute length measurement using multiple-wavelength phase-stepping interferometry*, Ph.D. thesis, University of London.

[109] Lieske, J. H., and V. K. Abalakin (eds.), 1989, *Inertial Coordinate Systems on the Sky*, volume 141 of *IAU Symposium* (Kluwer, Dordrecht).

[110] Lindegren, L., 1980, Astron. & Astrophys. **89**, 41.

[111] von der Lühe, O., 1995, *Fried Parameter* r_0*, Isoplanatic Angle* ϑ_0 *and Correlation Lifetime* τ_0 *at Cerro Paranal from PARSCA 1992 Balloon Data*, VLT-TRE-ESO-10000-0783.

[112] Ma, L.-H., D.-C. Liao, and Y.-B. Han, 2006, Chin. J. Astron. Astrophys. **6**, 769.

[113] Mathar, R. J., 2001, *Acromag Real-Time Tests*, Technical Report.

[114] Mathar, R. J., 2002, *DL LCU–ROE Connectivity Tests*, Technical Report.

[115] Mathar, R. J., 2004, Appl. Opt. **43**(4), 928.

[116] Mathar, R. J., 2005, *Astrometric Survey for Extra-Solar Planets with PRIMA, Requirements on Differential AT Mirror Surface Localizations*, VLT-TRE-AOS-15753-0004.

[117] Mathar, R. J., 2005, *Astrometric Survey for Extra-Solar Planets with PRIMA, Requirements on Medium-Term Stability of Air Parameters in VLTI Ducts and Delay Lines*, VLT-SPE-AOS-15753-0003.

[118] Mathar, R. J., 2005, Baltic Astronomy **14**(2), 277.

[119] Mathar, R. J., 2006, *Astrometric Survey for Extra-Solar Planets with PRIMA, Astrometric dispersion correction*, UL-TRE-AOS-15753-0010.

[120] Mathar, R. J., 2006, *Astrometric Survey for Extra-Solar Planets with PRIMA, Choice of Detector Spectral Band Widths*, UL-TRE-AOS-15753-0012.

[121] Mathar, R. J., 2006, *MIDI Optical path differences and phases*, Technical Report.

[122] Mathar, R. J., 2006, *PRIMA Non-Astrometric Modes, External Fringe Tracking for MIDI*, UL-ICD-DDL-15728-0009.

[123] Mathar, R. J., 2006, arXiv:astro-ph/0608273 .

[124] Mathar, R. J., 2006, arXiv:astro-ph/0605304 .

[125] McCarthy, D. D., and G. Petit, 2003, *IERS Technical Note No 32*, Technical Report, IERS Convention Centre, http://www.iers.org/iers/publications/tn/tn32/, URL `http://www.iers.org/iers/publications/tn/tn32/`.

[126] Mège, P., F. Malbet, and A. Chelli, 2003, in *Interferometry for Optical Astronomy II*, edited by W. A. Traub (Int. Soc. Optical Engineering), volume 4838 of *Proc. SPIE*, pp. 329–337.

[127] Ménardi, S., and A. Gennai, 2001, *Technical Specification for the PRIMA Fringe sensor unit*, VLT-SPE-ESO-15740-2210.

[128] Menardi, S., and A. Wallander, 2005, *VLT, Technical Report on FINITO Autocollimation, Results from Paranal Tests March, 2005*, VLT-TRE-ESO-15430-3595.

[129] Milman, M. H., 2005, J. Opt. Soc. Am. A **22**(12), 2774.

[130] Montilla Garcia, M. I., 2004, *Michelson wide-field stellar interferometrie*, Ph.D. thesis, Technische Universiteit Delft.

[131] Murakawa, K., and R. J. Mathar, 2005, *Astrometric Survey for Extra-Solar Planets with PRIMA, Polarization Effects*, AS-TRE-AOS-15753-0011.

[132] Muterspaugh, M. W., 2005, *Binary Star Systems and Extrasolar Planets*, Ph.D. thesis, Massachusetts Institute of Technology.

[133] Nijenhuis, J. R., 2003, *PRIMA Star Separater (STS), Design and Analysis Report*, VLT-TRE-TNO-15710-0001.

[134] Ninane, N., 2001, *VLT The Auxiliary Telescope System, Az axis test report for AT#1*, VLT-TRE-AMO-151100-223.

[135] Ninane, N., 2002, *VLT The Auxiliary Telescope System, AT#1: Altitude axis alignment w.r.t. Azimuth Axis*, VLT-TRE-AMO-151100-224.

[136] Parratt, L. G., 1961, *Probability and experimental errors in science* (John Wiley, New York, London).

[137] Percheron, I., M. Wittkowski, R. Donaldson, E. Fedrigo, C. Lidman, S. Morel, F. Rantakyro, M. Schöller, and A. Wallander, 2006, in *Advances in Stellar Interferometry*, edited by J. D. Monnier, M. Schöller, and W. Danchi (Int. Soc. Optical Engineering), volume 6268, pp. 1268–1275.

[138] Phan Duc, T., and P. Gitton, 2005, *VLTI Software, Infra-red Image Sensor, Control Software Design Description*, VLT-SPE-ESO-15450-3196.

[139] Pirnay, O., 2002, *VLT The Auxiliary Telescope System, AT#1: Altitude axis run-out test report*, VLT-TRE-AMO-151100-237.

[140] Pirnay, O., 2002, *VLT The Auxiliary Telescope System, OPL Stability Test report*, VLT-TRE-AMO-151100-255.

[141] Pirnay, O., 2002, *VLT The Auxiliary Telescope System, Telescope Structural Deflection Test Report*, VLT-TRE-AMO-151100-265.

[142] Pirnay, O., 2004, *VLT The Auxiliary Telescope System, AT #3 Alt Axis alignment wrt Azimuth Axis*, VLT-TRE-AMO-151100-356.

[143] Pirnay, O., 2004, *VLT The Auxiliary Telescope System, AT #3 Altitude Axis Run-out Test Report*, VLT-TRE-AMO-151100-358.

[144] Pirnay, O., 2004, *VLT The Auxiliary Telescope System, Az axis test report for AT #3*, VLT-TRE-AMO-151100-355.

[145] Pradel, N., P. Charlot, and J.-F. Lestrade, 2006, Astron. Astrophys. **452**(3), 1099.

[146] Pu, J., 1993, J. Optics (Paris) **24**(3), 141.

[147] Puech, F., and P. Gitton, 2005, *Interface Control Document between VLTI and its Instruments*, VLT-ICD-ESO-15000-1826. On page 110, f_c^{-2} should read $f_c^{-8/3}$, $f < f$ should read $f < f_c$, and $1.38\,10^{-3}$ should read 1.38×10^{-3}.

[148] Puech, F., S. Lévq̂ue, M. Sarazin, and R. J. Mathar, 2006, in *Advances in Stellar Interferometry*, edited by J. D. Monnier, M. Schöller, and W. Danchi (Int. Soc. Optical Engineering), volume 6268, pp. 1244–1255.

[149] Raspollini, P., P. Ade, B. Carli, and M. Ridolfi, 1998, Appl. Opt. **37**(17), 3697.

[150] Ravensbergen, M., 1993, *VLT Time Reference System Specification*, VLT-SPE-ESO-17300-0376.

[151] Ravensbergen, M., 1995, *VLT Time Reference System, Time Interface Module, Technical Manual*, VLT-MAN-ESO-17300-473.

[152] Reffert, S., A. Quirrenbach, W. J. Jaffe, and R. J. Mathar, 2007, *Astrometric Survey for Extra-Solar Planets with PRIMA, Operation and Calibration Strategy*, VLT-TRE-AOS-15754-0001.

[153] Rice, S. O., 1954, *Mathematical Analysis of Random Noise* (Dover), pp. 133–294, reprinted from Bell System Journals 23, 24.

[154] Roddier, F., J. M. Gilli, and G. Lund, 1982, J. Optics **13**(3), 263.

[155] Roddier, F., and P. Lena, 1984, J. Optics (Paris) **15**(6), 363.

[156] Roddier, N., 1990, Opt. Eng. **29**(10), 1174.

[157] Ruilier, C., 1998, in *Astronomical Interferometry*, edited by R. D. Reasenberg (Int. Soc. Optical Engineering), volume 3350 of *Proc. SPIE*, pp. 319–329.

[158] Saint-Jacques, D., 1998, *Astronomical Seeing in Space and Time*, Ph.D. thesis, Cambridge University.

[159] Sarazin, M., and A. Tokovinin, 2001, in *Beyond Conventional Adaptive Optics*, edited by R. Ragazzoni, N. Hubin, and S. Esposito (ESO), volume 58 of *ESO Conference and Workshop Proceedings*, p. 321.

[160] Saunders, E. S., T. Naylor, and A. Allan, 2006, Astron. Astrophys. **455**(2), 757.

[161] Schlüter, W., and N. R. Vandenberg, 2003, in *16th Working Meeting on European VLBI for Geodesy and Astrometry*, edited by W. Schwegmann and V. Thorandt (Bundesamt für Kartographie und Goedäsie), volume 16, pp. 3–13.

[162] Schuhler, N., 2003, *Second harmonic generation and iodine spectroscopy for the frequency stabilization of an Nd:YAG Laser emitting at 1.319 μm*, Master's thesis, Université Louis Pasteur, Strasbourg.

[163] Shaklan, S. B., and F. Roddier, 1987, Appl. Opt. **26**(11), 2159.

[164] Shaklan, S. B., and F. Roddier, 1988, Appl. Opt. **27**(11), 2334.

[165] Shao, M., and M. M. Colavita, 1992, Astron. Astrophys. **262**, 353.

[166] Shao, M., and D. H. Staelin, 1977, J. Opt. Soc. Am. **67**(1), 81.

[167] Shapiro, I. I., J. J. Wittels, C. C. Counselman, D. S. Robertson, A. R. Whitney, H. F. Hintegergger, C. A. Knight, A. E. E. Rogers, T. A. Clark, L. K. Hutton, and A. E. Niell, 1979, Astron. J. **84**(10), 1459.

[168] Smart, W. M. (ed.), 1958, *Combination of Observations* (Cambridge University Press, Cambridge).

[169] Sosnowska, D., and A. Huxley, 2005, *Astrometric Survey for Extra-Solar Planets with PRIMA, Differential Delay Lines Control, Software Requirements, Design and Interfaces*, VLT-TRE-DDL-15728-3353.

[170] Sovers, O. J., J. L. Fanselow, and C. S. Jacobs, 1998, Rev. Mod. Phys. **70**(4), 1391.

[171] Sozzetti, A., 2005, Publ. Astron. Soc. Pac. **117**(836), 1021.

[172] Stam, D. M., and J. W. Hovenier, 2005, Astron. Astrophys. **444**(1), 275.

[173] Stanghellini, S., and A. Michel, 1998, The Messenger **94**, 10.

[174] Stolen, R. H., 1975, Appl. Opt. **14**(7), 1533.

[175] Tanaka, K., 1985, J. Optics (Paris) **16**(6), 251.

[176] Tatarskii, V. I., 1961, *Wave Propagation in a Turbulent Medium* (McGraw-Hill).

[177] Thornton, B. S., 1955, Aus. J. Phys. **8**(2), 241.

[178] Toyoshima, M., 2006, J. Opt. Soc. Am. A **23**(9), 2246.

[179] Tubbs, R. N., 2005, arXiv:astro-ph/0506140 .

[180] Tubbs, R. N., 2005, Applied Optics **44**(29), 6253.

[181] Turyshev, S. G., 2003, Appl. Opt. **42**(1), 71.

[182] Venema, L. B., *et al.*, 2003, *Astrometric Survey of Extra-Solar Planets with PRIMA, Technical Proposal*, Planets-PRI-TEC-0002.

[183] Wagner, R. E., and W. J. Tomlinson, 1982, Appl. Opt. **21**(15), 2671.

[184] Wallace, P. T., 2005, *IPHASE, Interferometer Optial-Path-Length Analysis System*, http://www.tpsoft.demon.co.uk.

[185] Wallander, A., 2005, *Raw data format for PRIMA Astrometric Instrument*, TSD-05/072.

[186] Wallander, A., J. Argomedo, P. Ballester, B. Bauvir, M. Comin, R. Donaldson, P. Duhoux, A. Gennai, B. Gilli, N. Housen, A. Huxley, R. Karban, *et al.*, 2003, in *Astronomical Telescopes and Instrumentation 2002* (Int. Soc. Optical Engineering), volume 4848 of *Proc. SPIE*, no. 11.

[187] Wallander, A., B. Bauvier, M. Dimmler, and S. Menardi, 2004, *VLT, Technical Report on Finito and Fringe Tracking, Results from Paranal Tests 27/3–7/4, 2004*, VLT-TRE-ESO-15430-3303.

[188] Wang, J. Y., and J. K. Markey, 1978, J. Opt. Soc. Am. **68**(1), 78, a factor $1/(\pi D^2)$ is missing on the r.h.s. of (28), the l.h.s. of (29) and two times in (33). A factor πD^2 is missing on the r.h.s. of (36). A factor π is missing on the r.h.s. of (37). The uppermost case in (43) should be dropped the condition in the middle case be simplified to "if $p = p'$". Fig. 5 shows $\sqrt{2}K_1^0$, not K_1^0.

[189] Whittet, D. C. B., 2004, in *Astrophysics of Dust*, edited by A. N. Witt, G. C. Clayton, and B. T. Draine (ASP), volume 309 of *ASP Conference Series*, pp. 65–75.

[190] Wilhelm, R., B. Koehler, and P. Gitton, 2002, *Functional Description of the VLTI*, VLT-ICD-ESO-15000-1918. The radii of curvature of M2, M5 and M7 in Table 4-1 are wrong. See [173] for M2.

[191] Wyant, J. C., 1975, Appl. Opt. **14**(12), 2622.

[192] Zernike, F., 1934, Physica **1**, 689.

[193] Zernike, F., 1934, Month. Not. Roy. Astron. Soc. **94**(5), 377.

[194] Zhang, Y., B. Zhang, and Q. Wen, 2006, Opt. Commun. **226**(2), 407.

[195] Ziad, A., M. Schöck, G. A. Chanan, M. Troy, R. Dekany, B. F. Lane, J. Borgnino, and F. Martin, 2004, Appl. Opt. **43**(11), 2316.

1.8 Acronyms

AI	Action Item
AMOS	Advanced Mechanical and Optical Systems `http://www.amos.be/index.htm`
AO	Adaptive Optics
ARC	Ecole d'ingenieurs de l'arc Jurassie `http://www.eiaj.ch/`
ASM	Astronomical Site Monitor `http://www.eso.org/gen-fac/pubs/astclim/paranal/asm/`
ASTRON	Stichting Astronomisch Onderzoek in Nederland `http://www.astron.nl`
AT	Auxiliary Telescope (of the VLTI) `http://www.eso.org/projects/vlti/AT/index_at.html`
BC	Beam Combiner
CMM	Configuration Management Module http://www.eso.org/projects/vlt/sw-dev/wwwdoc/dockit.html
COAST	Cambridge Optical Aperture Synthesis Telescope `http://www.mrao.cam.ac.uk/telescopes/coast/`
CPU	Central Processing Unit
DDL	Differential Delay Line `http://www.mpia-hd.mpg.de/PRIMA-DDL/`
DL	Delay Line
DOPD	differential OPD
DRS	Data Reduction System

EPFL	École Polytechnique Fédérale de Lausanne `http://www.epfl.ch`
ESO	European Southern Observatory `http://www.eso.org`
FEM	Finite Element Method
FFT	Fast Fourier Transform
FITS	Flexible Image Transport System `http://fits.gsfc.nasa.gov`
FOV	field of view
FSM	Field Selector Mirror (of the STS)
FSU	Fringe Sensing Unit
FTS	Fourier Transform Spectrometer
GPD	geometric path difference
GPS	Global Positioning System
GS	Guide Star
IERS	International Earth Rotation and Reference Systems Service `http://www.iers.org`
IOTA	Infrared Optical Telescope Array `http://www.cfa.harvard.edu/cfa/oir/IOTA/`
IR	Infrared
IRIS	Infrared Image Sensor `http://www.eso.org/projects/vlti/iris/`
LCU	Local Control Unit
LST	Local sidereal time
MACAO	Multiple Application Curvature Adaptive Optics System
MDL	main delay line `http://www.eso.org/outreach/press-rel/pr-2000/phot-26-00.html`
MIDI	Mid-Infrared Interferometric Instrument `http://www.mpia.de/MIDI`
NACO	NAOS-CONICA `http://www.mpia.de/NACO/`
NOVA	Nederlandse Onderzoekschool voor Astronomie `http://www.strw.leidenuniv.nl/nova/`
OPD	optical path difference
OPL	optical path length
OTF	optical transfer function
PDR	Preliminary Design Review
PRIMA	Phase-Reference Imaging and Microarcsecond Astrometry `http://obswww.unige.ch/Instruments/PRIMA`

PRIMET	PRIMA Metrology `http://www.eso.org/projects/vlti/instru/prima/description_lms_prima.html`
PS	primary star
PSD	power spectral density
PSF	point spread function
PW	plain wave
PWV	precipitable water vapor
RAM	Random Access Memory
RMS	Root of Mean Squared
rms	root mean-squared
ROE	Readout Electronics
ROS	Relay Optics Structure
S/N	signal-over-noise ratio
SS	secondary star
STRAP	System for Tip-tilt removal with Avalanche Photodiodes
STS	star separator
SUSI	Sydney University Interferometer `http://www.physics.usyd.edu.au/astron/astron.html`
SW	software
TAD	transverse atmospheric dispersion
URL	Universal Resource Locator
UT	Unit Telescope (of the VLTI) `http://www.eso.org/projects/vlt/unit-tel/`
UTC	Universal Time Coordinated
VCM	variable curvature mirror
VINCI	VLT Interferometer Comissioning Instrument
VITRUV	proposal of a 2nd generation VLTI instrument `http://de.wikipedia.org/wiki/Vitruv`
VLBI	Very Long Baseline Interferometry
VLTI	Very Large Telescope Interferometer `http://www.eso.org/vlti`
VTT	Vacuum Tower Telescope `http://www.kis.uni-freiburg.de/kiswwwe2.html`
WFE	wave front error

1.9 Notations

a,	angle between baseline and (mean) star direction, elevation angle of baseline pointing
A, ΔA	azimuth angle, area, differential azimuth
α	right ascension
b	baseline length
c	speed of light in vacuum
d	aperture diameter
δ	declination
D, D_Φ	OPD, structure function
ΔD	differential OPD
$\epsilon(\ldots)$	(absolute) error of ...
f	focal length
φ	star pair orientation angle
ϕ	phase, azimuthal pointing direction of baseline
Φ	geographical latitude
g	gravitational constant
h	atmospheric layer height, hour angle
i	imaginary unit
I	intensity
J_1	Bessel Function
$\mathbf{k}$, k	wave vector and its modulus $2\pi/\lambda$
L	path length
λ	wavelength, geographical longitude
m	(Zernike) azimuth mode parameter; mass
M	IR metrology reading
N	number of sky positions for baseline calibration
n	refractive index
ν	frequency
P	projected baseline
ψ	electric field amplitude
r_0	Fried parameter
R	spectral resolution, molar gas constant
ρ	molecular density, distance between aperture points, earth radius
$\mathbf{s}$	unit vector into star direction
σ^2,σ	variance, standard deviation
t	time
τ	star separation angle
ϑ	azimuth angle of the pupil coordinate system
θ	obliquity angle
U, V, W	Paranal platform coordinates
v	(wind) velocity
V	volume
ω	angular velocity
X	GPD added by the DDL
z, Δz	zenith angle, differential zenith angle, atmospheric turbulence

2 SUMMARY

The large variety of effects can be put into two categories, the first one comprising the errors where either only the size of the correction is known, but not the residual error after correction, or no numbers have been assigned at all, the second comprising errors with a known cap. Therefore in roughly decreasing order of worry the non-negligible systematic errors known at the time of writing:

1.
   - The fringe tracker performance at the given configuration of one center pixel from 2.05 to 2.45 μm, two side pixles one of which buried under background noise, starting at 2.45μm with no cold filter, remains undocumented.
   - The TAD (angular color separation on entry to the telescopes) leads to additional coupling efficiency losses into the fiber of $< 5\%$ relative to 2.25 μm for wavelengths from 1.9 to 2.6 μm and zenith distances up to 60 deg; the residual effects on the DOPD in conjunction with different colors of the stars remain unclassified up to now.
2.
   - At a reference star separation of $1'$, sideways motions of M1, M2, M5 and M7 on the scale of 0.2 μm into some highly sensitive directions generate 5 nm of DOPD, if not matched by symmetrical effects on the other telescope. A very high sensitivity also w.r.t. tilts in some specific direction on the scale of $0.01''$ exists for M1 (at a PSF of $0.3''$) and M7. This contribution is not sensed by PRIMET. A measurement of the hysteresis of the deflection between M1 and M2 of AT#3 when moving through the standard altitude range reached up to $2.4''$ and could therefore exceed this allowance by typically a factor of 100. The only known simple measure to reduce this error is to chose smaller angular separations between the PS and the SS.
   - The effect of lensing by the earth atmosphere on the baseline (length up to 0.5 mm and direction up to 0.5 arcsec), the OPD (up to 100 μm, some μm dispersion in the K band) and differential OPD (up to 300 nm at 200 m baselines, 55 deg zenith angle and star separation of 2 arcmin) have been modeled, but experimental verification with exiting MIDI data turns out to be fruitless. An error of one kilometer in the atmospheric scale height would introduce a 10% error in the correction.
   - Group delay algorithms that ignore the actual curvature of the air dispersion in the K band can be off by 250 nm. However, this is not a serious concern, because the fringe tracker is not forced to ignore the second-order derivatives, and the DRS can use independent, advanced models as long as the tracker does not suffer from fringe jumps and the ABCD data are made available to the DRS.
   - A difference in the beam temperatures of 1°C, for example caused by lateral heating in the ducts, contributes up to 30 nm to the DOPD. The effect can be annihilated by off-line averaging of beam switched pairs of observations.
   - The ellipticity of the VLTI mirror train is expected to be of the order of 10°, more than the effect of a DOPD of 5 nm at a wavelength of 2.2 μm corresponding to 1°. The measured values cannot be reproduced by combining incidence angles (as a function of parallactic angle) and complex refractive indices on the mirror surfaces on a calculational basis because the measured reflection coefficients of the mirrors are off by a factor of three from Silver literature data. If this situation persists, a hardware solution with an additional (by definition erroneous) polarization analyzer is valuable.
   - Non-intersection of the Alt-Az axis pairs introduce a “wobble” of ≈ 50 μm in the baseline length as a function of azimuth.

- Differential axis runouts of $\approx 20\ \mu$m are expected to generate add ≈ 30 nm of spurious DOPD.
- Supposed that this orientation of the star pair is well-resolved, the error in the angle (relative pointing direction) between the global star position and the baseline direction contributes to the error in the astrometric angle multiplied by a factor of up to $5 \cdot 10^{-4}$. For an error of 10 μas in astrometry, this becomes a requirement on the accuracy of the star positions of $0.02'' = 9.7 \cdot 10^{-8}$ rad and on the accuracy on the baseline positions of 9.7μm per 100 m baseline.
- If the DDL's are in the evacuated mode, some one-time calibration w.r.t. doubly-differential chromatic window thickness is needed to account for a typical 500 nm in the DOPD, and beam switching to remove terms of the order 20 nm. The alternative is *not* to evacuate the DDL's (ie, to remove the windows with their inherently large material dispersion) such that, even under drastic changes in the environmental parameters of the air in the DDL vessels, the chromatic corrections cannot change by more than 4 nm.
- Each error of 1000 K in the differential star temperature implies an error in the effective wave number of the central pixel which adds typically 7 nm to the error in the differential OPD caused by the typical tunnel air dispersion.
- The absolute error in the astrometric angle equals the absolute error in the ratio of the differential OPD over the baseline divided by the cosine of an angle that specifies how far the pair orientation angle is misaligned w.r.t. the direction specified by the projected baseline, which defines the plane of "high interferometric resolution." The importance of this effect is highly variable, but may be controlled to a high degree by pairing baselines and schedules such that the axis of the pair of stars gets "well resolved" at the time of observation (by moving schedules). The worst case is limited to $1.2\lambda/d \approx 0.31''$ of the single-telescope PSF.
- Slight achromatic effects within the K prism of the FSU introduce phase shifts of the order of $\pm 0.5°$ within the K band, which is small compared to the aforementioned ellipticity.
- The transverse atmospheric dispersion across the K band leads to equivalent beam tilts in the delay line tunnel, which transform into a maximum of 0.2 nm correction per 100 m delay over the K band spectrum. The effect on the differential delay is presumably smaller.
- For an error of 40 μm per 100 m baseline one needs to visit approximately 5–7 stars (measure 5–7 delays) if their positions are known to $0.2''$ or approximately 30 stars if their positions are known to $0.4''$.
- The performance of the metrology system is not an issue. If it should loose lock in slewing modes, it seems to be advisable to bridge these gaps by cross-coupling the reading to the positions of the VLTI DL carriage by software during post-processing, which converts this into a software issue.
- Standard tidal motion (as opposed to earth quakes) on single cm scales can be processed as baseline rotations and is equivalent to tiny baseline corrections of ~ 100 nm.

This list refers to what is said elsewhere in this manuscript here and to the contents of [101, 119, 131]; to maintain its readability, references have not repeated.

The limiting magnitude of PRIMA will depend critically on the fringe tracking performance, or on the ability to perform passive astrometric measurements without fringe phase tracking.

Finally, Tab. 1 is another version of the most important of the same facts. At this level of condensation, contents is almost entirely lost and ought not be used as a reference. Most errors are highly dependent on the observational parameters as explicitly described in the manuscript's sections and in the references cited. To avoid misinterpretation, only estimates of upper limits are given in these cases.

Effect	variable	Magnitude	After Calibr. or Corr.	Reference
AT mirror motion	ΔD	< 450 nm	?	Sect. 13.4, [116]
atmospheric lensing	ΔD	< 400 nm	< 20 nm	[118, 119]
atmospheric lensing	b	< 0.5 mm	?	[118, 119]
dispersion model of tracker SW	D	< 500 nm	0	[119]
horiz. temp. gradient	ΔD	< 30 nm	TBD	[117, 119]
error differential star temp. (per 1000 K)	ΔD	< 10 nm	NA	[119]
mirror polarization	ϕ	$< 10^\circ$	$< 1^\circ$	[131]
evacuated DDL windows	ΔD	20 nm	0	[101]
axis runouts	b	50 μm	0	11.4.3
axis runouts	ΔD	< 30 nm	0	Sect. 13.5.5
global star pair position (per $0.1''$)	τ	$\sim 10^{-6}$	NA	Sect. 28.3
baseline vector orient. (per 10μm per 100 m)	τ	$\sim 10^{-7}$	NA	Sect. 28.3.2
star pair orientation	τ	0–10 mas	0	Sect. 28.3.2

Table 1: Paraphrasal of the most important pieces of the itemized list that starts at page 19, including systematic errors only. The variable's notation is according to Sect. 1.9. Error estimates in the "Magnitude" column without units are relative to the variable in question (here: τ).

3 INTRODUCTION

3.1 Background

Producing an error budget for PRIMA astrometric observations will be a long and complicated process. In order to break up the work, the error calculation has been separated into a number of principle terms, with each term getting a section (or appendix) in this document. Each of these sections provides an introduction to the error term. A little more detail has been provided for some of the error terms, where that information was already available in existing documents. A substantial amount of further work will be required in order to complete the error budget.

One of the most difficult tasks has been to find the interdependencies of each of the different error terms. If one term in the error budget calculation is changed, this list of interdependencies can be used to work out which other components of the error budget calculation will be effected by the change. These include both direct dependencies (the terms in the error budget which are directly effected by a change) and indirect dependencies (those terms which are effected indirectly through a change in an intermediate term in the calculations).

In order to introduce the terminology used in this report I will first give an introduction to atmospheric turbulence and interferometry. In the standard classical theory, light is treated as an oscillation in a field ψ. For monochromatic plane waves arriving from a distant point source with wave-vector $\mathbf{k}$:

$$\psi_u\left(\mathbf{r},t\right) = A_u e^{i\left(\phi_u + 2\pi\nu t + \mathbf{k}\cdot\mathbf{r}\right)} \tag{1}$$

where ψ_u is the complex field at position $\mathbf{r}$ and time t, with real and imaginary parts corresponding to the electric and magnetic field components, ϕ_u represents a phase offset, ν is the frequency of the light determined by $\nu = c\left|\mathbf{k}\right|/\left(2\pi\right)$, and A_u is the amplitude of the light.

The photon flux in this case is proportional to the square of the amplitude A_u, and the optical phase corresponds to the argument of the complex variable ψ_u. As wavefronts pass through the Earth's atmosphere they may be perturbed by refractive index variations in the atmosphere. Figure 1 shows schematically a turbulent layer in the Earth's atmosphere perturbing planar wavefronts before they enter a telescope. The perturbed wavefront ψ_p may be related at any given instant to the original planar wavefront $\psi_u\left(\mathbf{r},t\right)$ in the following way:

$$\psi_p\left(\mathbf{r},t\right) = \left(\chi_p\left(\mathbf{r},t\right) e^{i\phi_p\left(\mathbf{r},t\right)}\right)\psi_u\left(\mathbf{r},t\right) \tag{2}$$

where $\chi_p\left(\mathbf{r},t\right)$ represents the fractional change in wavefront amplitude and $\phi_p\left(\mathbf{r},t\right)$ is the change in wavefront phase introduced by the atmosphere. From here on in this document, $\phi_p\left(\mathbf{r},t\right)$ will be called the optical phase (although strictly it is the *perturbation* in the optical phase in comparison to an unperturbed light beam). Similarly, in discussions of atmospheric effects $\chi_p\left(\mathbf{r},t\right)$ will be called the wavefront amplitude although it is actually a normalised form of the amplitude.

A description of the nature of the wavefront perturbations introduced by the atmosphere is provided by the Kolmogorov model developed by Tatarksi ([176]) and Kolmogorov ([94, 95]). This model is supported by a variety of experimental measurements and is widely used in simulations of astronomical instruments. The model assumes that the wavefront perturbations are brought about by variations in the refractive index of the air. These refractive index variations lead directly to phase fluctuations described by $\phi_p\left(\mathbf{r},t\right)$, but any amplitude fluctuations are only brought about as a second-order effect while the perturbed wavefronts propagate from the perturbing atmospheric layer to the telescope. The performance of interferometers is dominated by the phase fluctuations $\phi_p\left(\mathbf{r},t\right)$,

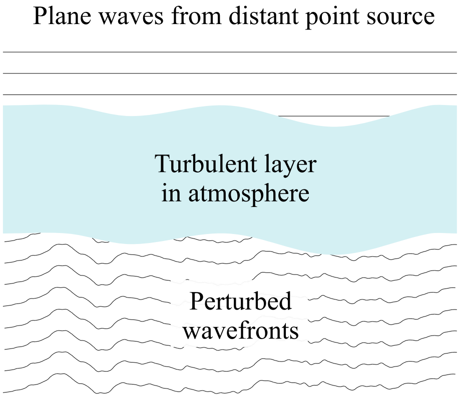

Figure 1: Schematic diagram illustrating how optical wavefronts from a distant star may be perturbed by a turbulent layer in the atmosphere. The vertical scale of the wavefronts plotted is highly exaggerated.

although the amplitude fluctuations described by $\chi_p(\mathbf{r},t)$ introduce intensity variations (scintillation) in the interferometric signal.

The spatial phase fluctuations at an instant in time in a Kolmogorov model are usually assumed to have a Gaussian random distribution with the following second order structure function:

$$D_{\phi_p}(\rho) = \left\langle \left|\phi_p(\mathbf{r}) - \phi_p(\mathbf{r}+\rho)\right|^2 \right\rangle_{\mathbf{r}} \tag{3}$$

where $D_{\phi_p}(\rho)$ is the atmospherically induced variance between the phase at two parts of the wavefront separated by a distance ρ in the aperture plane, and $\langle \ldots \rangle$ represents the ensemble average.

The structure function of [176] can be described in terms of a single parameter r_0:

$$D_{\phi_p}(\rho) = 6.88 \left(\frac{|\rho|}{r_0}\right)^{5/3} \tag{4}$$

r_0 indicates the "strength" of the phase fluctuations as it corresponds to the diameter of a circular telescope aperture at which atmospheric phase perturbations begin to seriously limit the image resolution. Typical r_0 values for K band (2.2 μm wavelength) observations at good sites are 40—90 cm. Fried ([59]) noted that r_0 also corresponds to the aperture diameter d for which the variance σ^2 of the wavefront phase averaged over the aperture comes approximately to unity:

$$\sigma^2 = 1.0299 \left(\frac{d}{r_0}\right)^{5/3} \tag{5}$$

Equation 5 represents a commonly used definition for the atmospheric coherence length r_0.

3.2 Interferometry

An interferometer typically consists of a number of sub-apertures positioned in a plane. Movements of the sub-apertures are used to produce a larger synthesized aperture plane. The aim of an interferometer is to measure the cross-correlation between the electric field measured at different points in the synthesized aperture plane. Light is collected with two or more sub-apertures (typically telescopes or siderostats) and a wavelength range is selected using optical filters. The simplest form of cross-correlation for an interferometer with two sub-apertures (and the fundamental goal of a measurement with a PRIMA FSU) is the correlated flux C from the star:

$$C = \psi_{u1}\psi_{u2}^{*} \tag{6}$$

where ψ_{u1} and ψ_{u2} are the complex electric field amplitudes from the two sub-apertures produced by the star, and * indicates the complex conjugate. In VLTI/PRIMA the wavefronts from the star are spatially filtered (see [47, 75, 89, 126] for a discussion of spatial filtering). This means that the flux from a single point in the image plane of each sub-aperture is selected, in contrast to the optical field as a function of position in the aperture plane described by $\psi_u(\mathbf{r}, t)$ in Equation 1. In reality C varies with time due to the change in projected baseline as the Earth rotates. In this discussion I will ignore the effects of Earth rotation on the projected baseline, which is adequate when describing a short astronomical observation.

The Earth's atmosphere introduces rapid fluctuations in the optical path length from an astronomical source to the two apertures, as discussed in Section 3.1. For monochromatic observations these optical path fluctuations can be described in terms of phase rotations $\phi_{p1}(t)$ and $\phi_{p2}(t)$ to ψ_{u1} and ψ_{u2} respectively in Equation 6 (in a similar way to Equation 2 in the aperture plane description). These phase rotations result in fluctuations in the phase of the correlated flux C. Again the amplitude fluctuations can be described by $\chi_{p1}(t)$ and $\chi_{p2}(t)$. Our description of the atmospherically perturbed correlated flux $C'(t)$ then looks like this:

$$\begin{aligned} C'(t) &= C\left(\chi_{p1}(t)\, e^{i\phi_{p1}(t)}\right)\left(\chi_{p2}(t)\, e^{i\phi_{p2}(t)}\right)^{*} && (7)\\ &= CA(t)\, e^{i\theta(t)} && (8)\end{aligned}$$

where $i = \sqrt{-1}$ and t is the time. $A(t)$ and $\theta(t)$ describe the amplitude and phase fluctuation introduced into the (complex) correlated flux by the atmosphere, and are given by:

$$\begin{aligned} A(t) &= \chi_{p1}(t)\,\chi_{p2}(t) && (9)\\ \theta(t) &= \phi_{p1}(t) - \phi_{p2}(t) && (10)\\ & && (11)\end{aligned}$$

The timescale over which the RMS change in the phase $\theta(t)$ at any given point is ~ 1 radian is called the coherence time t_c of the interference fringes. Each measurement of $C'(t)$ must be made within one coherence time in order to avoid the measurements being corrupted by phase fluctuations.

VLTI PRIMA can observe two different stars simultaneously. One PRIMA FSU measures the correlated flux $C'_{PS}(t)$ from the Primary Star (PS), and the other the correlated flux $C'_{SS}(t)$ on the Secondary Star (SS).

3.2.1 Narrow angle astrometry

The aim of the PRIMA astrometry program is to accurately measure the angular separation of stars which have small angular separations. This is possible using an interferometer as the atmosphere applies similar perturbations to both stars when the angular separation is small. For example the first star (PS) could have a correlated flux C_{PS} and atmospheric phase perturbation $\theta(t)$ and the second star (SS) a correlated flux C_{SS} and atmospheric phase perturbation $\theta(t) + \Delta\theta(t)$, giving atmospherically perturbed correlated fluxes of:

$$\begin{aligned} C'_{PS}(t) &= C_{PS}A_{PS}(t)\exp\left(i\theta(t)\right) && (12)\\ C'_{SS}(t) &= C_{SS}A_{SS}(t)\exp\left(i\left[\theta(t) + \Delta\theta(t)\right]\right) && (13)\end{aligned}$$

Note that $\Delta\theta\left(t\right)$ fluctuates randomly with zero mean. If the variance over time of $\Delta\theta$, $\left\langle\left|\Delta\theta\left(t\right)\right|^2\right\rangle_t < 1$ we are said to be in the isoplanatic regime (where the fringe differential phase is small). The mean difference in the phase of the correlated fluxes for the two stars is then related directly to the astrometric separation of the stars. If the isolated phases θ and $\theta + \Delta\theta$ were seperately generated from two sets of ABCD values [124, 166, 191],

$$\tan\theta = \frac{D_{PS} - B_{PS}}{A_{PS} - C_{PS}}, \quad \tan(\theta + \Delta\theta) = \frac{D_{SS} - B_{SS}}{A_{SS} - C_{SS}}, \tag{14}$$

the phase difference could be recovered from [1, 4.4.34]

$$\Delta\theta = \arctan\frac{(D_{SS} - B_{SS})(A_{PS} - C_{PS}) - (D_{PS} - B_{PS})(A_{SS} - C_{SS})}{(A_{SS} - C_{SS})(A_{PS} - C_{PS}) + (D_{SS} - B_{SS})(D_{PS} - B_{PS})}. \tag{15}$$

However, the need for an independent reduction of the two phases to geometric delays at two different effective wavenumbers (two different star colors), Eq. (6) in [120], renders the phase difference $\Delta\theta$ practically useless as an intermediate data product.

There are two general approaches to long baseline interferometry which I will call phase stabilised interferometery and non-phase stabilised interferometery.

3.2.2 Non phase-stabilised interferometry

Many existing interferometers (e.g. SUSI, COAST, IOTA, VINCI) are not phase stabilised. These interferometers measure observables which are not affected by atmospheric phase changes, so that it is not necessary to track the atmospheric phase fluctuations. The principle benefit of this is that a bright reference star is *not* required as the observables can be integrated over many fringe coherence times. Example observables include the visibility amplitude and the bispectrum or “triple-produce” (the phase of the bispectrum known as the closure phase is more often discussed, but the bispectrum is the fundamental observable).

3.2.3 Non phase-stabilised operation of PRIMA

In order to perform non phase-stabilised operation we must measure an observable which is not strongly affected by atmospheric phase changes. The simplest example is $C'_{PS}C'^{*}_{SS}$:

$$\begin{aligned} C'_{PS}C'^{*}_{SS} &= C_{PS}A_{PS}\left(t\right)\exp\left(i\theta\left(t\right)\right)C_{SS}A_{SS}\left(t\right)\exp\left(-i\left[\theta\left(t\right) + \Delta\theta\left(t\right)\right]\right) & (16)\\ &= C_{PS}C_{SS}A_{PS}\left(t\right)A_{SS}\left(t\right)\exp\left(-i\Delta\theta\left(t\right)\right) & (17)\end{aligned}$$

In the isoplanatic regime, $\left\langle\left|\Delta\theta\left(t\right)\right|^2\right\rangle_t < 1$ and varies randomly about zero, so we can obtain an accurate measurement of $C_{PS}C^{*}_{SS}$ by integrating $C'_{PS}C'^{*}_{SS}$ over many fringe coherence times. $C_{PS}C^{*}_{SS}$ is of great interest, as the phase of this number can be used to calculate the separation of the stars (the phase of $C_{PS}C^{*}_{SS}$ is commonly called the *astrometric phase*, although it is the complex number $C_{PS}C^{*}_{SS}$ which is the principle observable – a similar situation to the case of the bispectrum). The integration of $C_{PS}C^{*}_{SS}$ can be improved by weighting each measurement of $C'_{PS}C'^{*}_{SS}$ by an estimate of the S/N for that measurement.

In order to obtain a measurement of $C'_{PS}C'^{*}_{SS}$ with good S/N in a reasonable period of time, both stars must provide a S/N ratio of $\gtrsim 0.1$ for measurements of the correlated flux C.

3.2.4 Phase-stabilised interferometry

The NPOI and PTI interferometers actively track and compensate for atmospheric phase fluctuations. A bright reference star is required in order to do this typically providing a S/N of $\gtrsim 10$ for measurements of the correlated flux C_{PS} on the PS. Once the fringes are stabilised, faint signals which are phase-correlated with the fringes can be coherently integrated.

3.2.5 Phase-stabilised operation of PRIMA

Measurements of the atmospherically induced phase perturbations can be made on a bright star ($\theta\left(t\right)$ in Equations 12 and 16) and then the optical path length from the both stars can be physically adjusted (typically using movable mirrors) to remove the term $\theta\left(t\right)$ from the phase perturbations from both stars. For star (SS) we get:

$$C'_{SS} = C_{SS} \exp\left(i\Delta\theta\left(t\right)\right) \tag{18}$$

In the isoplanatic regime, $\left\langle\left|\Delta\theta\left(t\right)\right|^{2}\right\rangle_{t} < 1$ so the fringes on star (SS) will remain stable to within ~ 1 radian over long periods of time. This means that the fringe signal for star (SS) can be integrated on the detector over many atmospheric coherence times. In practice the maximum integration time in the infrared is limited by detector saturation from the thermal background, but the S/N for fringe measurements on the faint star (SS) will be a few times larger than for the non phase-stabilised case discussed in Section 3.2.3.

In this mode of operation, $C'_{PS}C'^{*}_{SS}$ can be calculated in the same way as in Section 3.2.3, providing information about the angular separation of the stars. Note that the phase of $C'_{PS}C'^{*}_{SS}$ (the *astrometric phase*) is only a useful parameter when the S/N ratio of $C'_{PS}C'^{*}_{SS}$ is greater than unity, so that for faint (SS) stars $C'_{PS}C'^{*}_{SS}$ must be integrated as a complex number until the S/N ratio is greater than one *before* the astrometric phase is calculated. This has important implications for the software running the PRIMA FSUs.

3.2.6 Limitations due to PRIMA hardware

The current design of the PRIMA FSU hardware should be compatible with both phase-stabilised operation (Section 3.2.5) and non phase-stabilised operation (Section 3.2.3). The low spectral resolution of the FSUs is slightly better optimised for phase-stabilised operation, however. If the data transfer architecture at the VLTI precludes the use of $C'_{PS}C'^{*}_{SS}$ as the primary observable for PRIMA, non phase-stabilised operation will be impossible and the limiting magnitude for phase-stabilised operation will be slightly poorer. For the remainder of this document I will assume that astrometric measurements are based on $C'_{PS}C'^{*}_{SS}$ provided from both phase-stabilised operations and non phase-stabilised operations of PRIMA.

3.2.7 Extension to a finite bandpass

Sections 3.2.1 to 3.2.5 are only strictly applicable at a single wavelength (i.e. for a monochromatic observation). The PRIMA FSUs utilize one broad channel and two narrow channels which together cover the K band (from $\sim 1.95\ \mu$m to $\sim 2.45\ \mu$m). Due to the refractive properties of the atmosphere, each wavelength within the K band follows a slightly different path through the atmosphere. Light of different wavelengths reaching the aperture plane will have passed through slightly different parts of the turbulent layers in the atmosphere. The optical phase offset ϕ at each wavelength depends on both the mean phase across each telescope aperture and on the corrugations in the phase across each of the telescope apertures. The phase rotation $\phi\left(\mathbf{r},t,\lambda\right)$ (cf. Equation 2) in the aperture plane induced by a high-altitude atmospheric layer, at a given wavelength λ and at a given time t and position $\mathbf{r}$ in the AT aperture are dependent on the fluctuation in delay induced by the atmospheric turbulence $\Delta z\left(\mathbf{r}'+\mathbf{\Delta r}'\left(\lambda\right),t,\lambda\right)$ as follows:

$$\phi\left(\mathbf{r},t,\lambda\right)=\frac{\Delta z\left(\mathbf{r}'+\mathbf{\Delta r}'\left(\lambda\right),t,\lambda\right)}{\lambda} \tag{19}$$

where $\mathbf{r}'$ is the projection of $\mathbf{r}$ along the line of sight towards the star up to the layer of turbulence, and $\mathbf{\Delta r}'\left(\lambda\right)$ is the wavelength-dependent offset from this path induced by bulk atmospheric refraction (the time delay for light propagation can be ignored).

In order to make measurements with high S/N ratio, the gradient of phase with wavelength must be minimised in the PRIMA FSU spectral channels. The phase difference between the correlated fluxes in the spectral channels at the edges of the K band is minimised through adjustments of the VLTI delay lines (group delay tracking). Note that it is the phase of $C_{PS}C_{SS}^{*}$ for the central spectral channel which will be used for astrometry (i.e. the phase difference between the fringes on the two stars in the central spectral channel). The group delay will not be used for astrometric measurements as it cannot be measured as accurately as the phase of $C_{PS}C_{SS}^{*}$, and because existing models for the refractive index of air provide lower accuracy when converting the group delay into the separation of the stars.

4 NUMERICAL COLORED SPECKLE SIMULATIONS

4.1 Introduction

Apart from a few simple cases such as an interferometer with pointlike apertures (see e.g. [24, 25]) or an interferometer with ideal AO correction (e.g. [37, 158]), the only approach which can be used to analyse the temporal properties of interferometric fringes is that of numerical simulation. Numerical simulations are also required to investigate specialised components in interferometers such as spatial filters (e.g. [89]). For this reason, numerical studies have often played an important role in studies of interferometer performance or design (e.g. [25]).

Numerical simulations were required in the preliminary stages of the error budget preparation for PRIMA in order to obtain order-of-magnitude estimates for many of the complicated error terms and highlight those which might be problematic. In order to minimise the time invested, existing atmospheric simulations were used with the minimum modification required for useful estimates of terms in the PRIMA error budget. More realistic simulations may be required at a later date to study in detail error terms which are expected to have a significant impact on the overall performance of PRIMA.

4.2 Simulation method

The simulations utilised a wind-scatter model of the atmosphere (see e.g. [154]) using two Taylor screens of frozen Kolmogorov turbulence with large ($> 1000 r_0$) outer scale. Fluctuations in air and water vapour spectral dispersion were not modelled, and the Taylor screens introduced equal fluctuations in the wavefront delay at all wavelengths.

In the simulations, the Taylor screens were blown past the simulated telescopes at constant wind velocities. The timescale for changes in the light intensity measured with a large diameter telescope is proportional to the parameter $(r_0/\Delta v)$ (see [2, 154]) where Δv is the standard deviation of the distribution of the wind velocities for the screens, weighted by the turbulence C_N^2 for each screen:

$$\Delta v = \left[\frac{\int_0^\infty |\mathbf{v}(h)|^2 C_N^2(h)\, \mathrm{d}h}{\int_0^\infty C_N^2(h)\, \mathrm{d}h} - \left| \frac{\int_0^\infty \mathbf{v}(h) C_N^2(h)\, \mathrm{d}h}{\int_0^\infty C_N^2(h)\, \mathrm{d}h} \right|^2 \right]^{1/2} \tag{20}$$

and using the same definitions for the layer height h, the wind velocity $\mathbf{v}$ and the turbulence strength C_N^2 as Roddier ([154]).

The Taylor screens were moved across the telescope aperture at the appropriate wind speeds along one axis of the rectangular Taylor screen array. A section of each Taylor screen was extracted at each time point and then rotated according to the wind direction angle and re-sampled to have at least twice as many pixels per r_0 using linear interpolation to minimise pixel aliasing. The resulting screens were summed and converted to complex wavefronts at a range of different wavelengths. After truncating the wavefronts with a circular telescope aperture, an image plane representation of the wavefronts was generated at each wavelength using an FFT. The atmospheric model used throughout this documents had two Taylor screens of equal strength moving at equal wind speed with wind angles differing by 120°. The time unit used when describing the simulations corresponds to the time taken for each of the Taylor screens to move by the coherence length r_0 for the wavefronts in the telescope aperture plane (after the wavefronts had been perturbed by both atmospheric layers).

Seven discrete wavelength channels were simulated, with equal spacings in wavelength between 1.97 μm and 2.43 μm. The correlated fluxes in the seven wavelength channels were then linearly combined to give three channels with wavelengths and bandpasses approximately matching the channels on the real PRIMA FSUs.

In some of the simulations, bulk atmospheric refraction and/or scintillation were also modelled. For these studies one of the Taylor screens was assigned an altitude of 500 m above the telescope and the other 5000 m. For refraction studies Snell's law was used to model the variation of the light ray position and tilt with wavelength and altitude, ensuring that the correct part of each Taylor screen was used for each wavelength channel. This was calculated using the approach introduced in Section 3.2.7.

The fluctuation in delay induced by the atmospheric turbulence ($\Delta z\left(\mathbf{r}' + \mathbf{\Delta r}'\left(\lambda\right), t, \lambda\right)$ from Equation 19) has only a small direct dependence on wavelength λ (due to dispersion), so the induced phase rotation is well approximated across the K band by:

$$\phi\left(\mathbf{r}, t, \lambda\right) = \frac{\Delta z\left(\mathbf{r}' + \mathbf{\Delta r}'\left(\lambda\right), t, \lambda_{cen}\right)}{\lambda} \tag{21}$$

where $\Delta z\left(\mathbf{r}' + \mathbf{\Delta r}'\left(\lambda\right), t, \lambda_{cen}\right)$ is the delay induced by atmospheric fluctuations at the centre of the K band (wavelength λ_{cen}) at position $\mathbf{r}' + \mathbf{\Delta r}'\left(\lambda\right)$ and time t. This approximation was utilised in all the numerical simulations of the effects of seeing on astrometric performance presented in this document. Note that in accurate calculations of the effect of atmospheric refraction and dispersion these simplifications should *not* be used.

For the simulations, the air density as a function of altitude was based on the Glenn Research Center's *Earth Atmosphere Model*, and the refractive index was calculated from the density using a cubic spline fit to K-band data from [115]. The optical ray displacement was calculated and integrated at 50 m intervals through the atmosphere.

For the scintillation studies a first-order approximation to the optical propagation was performed. The effect of each Taylor screen was investigated independently, with the amplitude fluctuation ($\chi_p\left(\mathbf{r}, t\right)$ from Equation 2) in the AT aperture plane estimated by applying phase changes in the conjugate plane to re-image the Taylor screen to the appropriate altitude. The amplitude fluctuations from the two Taylor screens were then combined multiplicatively without taking account of any second-order terms resulting from the interaction of the wavefront fluctuations induced by the two Taylor screens. The phase changes resulting from optical propagation from the turbulent layers to the telescopes were also ignored.

The spatial sampling of the electric field was kept constant in the image plane for all the simulations which necessarily required wavelength-dependent spatial sampling in the pupil plane.

4.3 Simulation Results

The simulations discussed in this section are widely used throughout the remainder of the document. A few very basic results are presented here to provide a better understanding of the simulations and of the variation of the optical wavefront properties with position in the image plane.

Figure 2 shows the short exposure image quality expected when using an AT to look at a point source 30° above the horizon under mediocre conditions. The effects of atmospheric refraction were ignored when generating this image. Note that the image is *coloured* – this means that the spectral energy distribution reaching the detectors will depend strongly on the position of the FSU spatial filter (or

Figure 2: Simulated short exposure image through an AT pointing at the zenith with $4r_0$ across the aperture diameter.

Figure 3: Identical to Figure 2 but including the effects of atmospheric refraction for a zenith angle of 60 degrees.

The three FSU spectral channels are shown in red, green and blue.

in other words on the tip-tilt error). If the STS is put into calibration mode, the light from one half of the PSF will be sent to one FSU, and the light from the other half of the PSF will be sent to the other PSF. The colour of the light sent to the two FSUs will be different, and hence the astrometric measurements on the two FSUs will also be different. The average colour of the light reaching the FSUs will vary with the seeing conditions and with the performance of the STRAP unit (as the size and shape of the mean PSF is strongly wavelength dependent).

Figure 3 is identical to Figure 2 except that atmospheric refraction has been "switched on" (including both the lateral shift of the beam in the atmosphere and the change in the angle-of-arrival with wavelength). Note that the colours are slightly different to the case with atmospheric refraction switched off (Figure 2). As the angle of refraction remains relatively constant with time during an observation, this colour shift will be systematically applied to a whole observation. If the STS is put into calibration mode, the two FSUs will receive light which has systematically different colours (and hence systematically different astrometric observables). As the flux distribution in the image depends on the seeing, the magnitude of the colour difference between the two channels will vary with the seeing conditions (i.e. on timescales of minutes and hours). This will lead to drifts in the differential phase between the two beams on similar timescales. In order to calibrate out this effect, the atmospheric seeing, STRAP unit performance, air density and humidity may have to be monitored at the ATs, particularly when using the STS calibration mode. A good knowledge of the coupling of the FSU spatial filter as a function of image-plane position and wavelength will be required for such a simulation. If the STS roof mirror is aligned with the direction of the bulk atmospheric dispersion the systematic effects may be substantially reduced.

Another area where numerical simulations are essential is in the assessment of fringe tracking performance when there are wavefront corrugations across the AT apertures. In early optical interferometers the apertures were usually stopped-down in order to keep the variance in the wavefront phase across the aperture below ~ 1 radian. With the introduction of spatial filters larger aperture sizes have come into common usage, and hence the variance of the wavefront phase is often much larger than 1 radian. It will be important to assess the effect of these wavefront corrugations on the temporal properties of the interferometric fringes and hence determine the expected fringe tracking performance. In order to highlight the detrimental effect of wavefront corrugations, maps of the optical phase and intensity in the image plane of a single telescope are shown for a large $(9r_0)$ aperture in Figure 4 for a series of closely-spaced time-steps. Each speckle in the image plane has a different (random) phase, and the speckles in the image change rapidly. If a spatial filter was used to select light from one speckle and use it in an interferometer, the phase of the light would vary as quickly as the phases of the speckles in the image plane. This is in stark contrast to the piston mode component (see e.g. [37]) which in this case does not change significantly from one time-step to the next, and thus contributes little to the high-frequency fluctuations in the fringe phase.

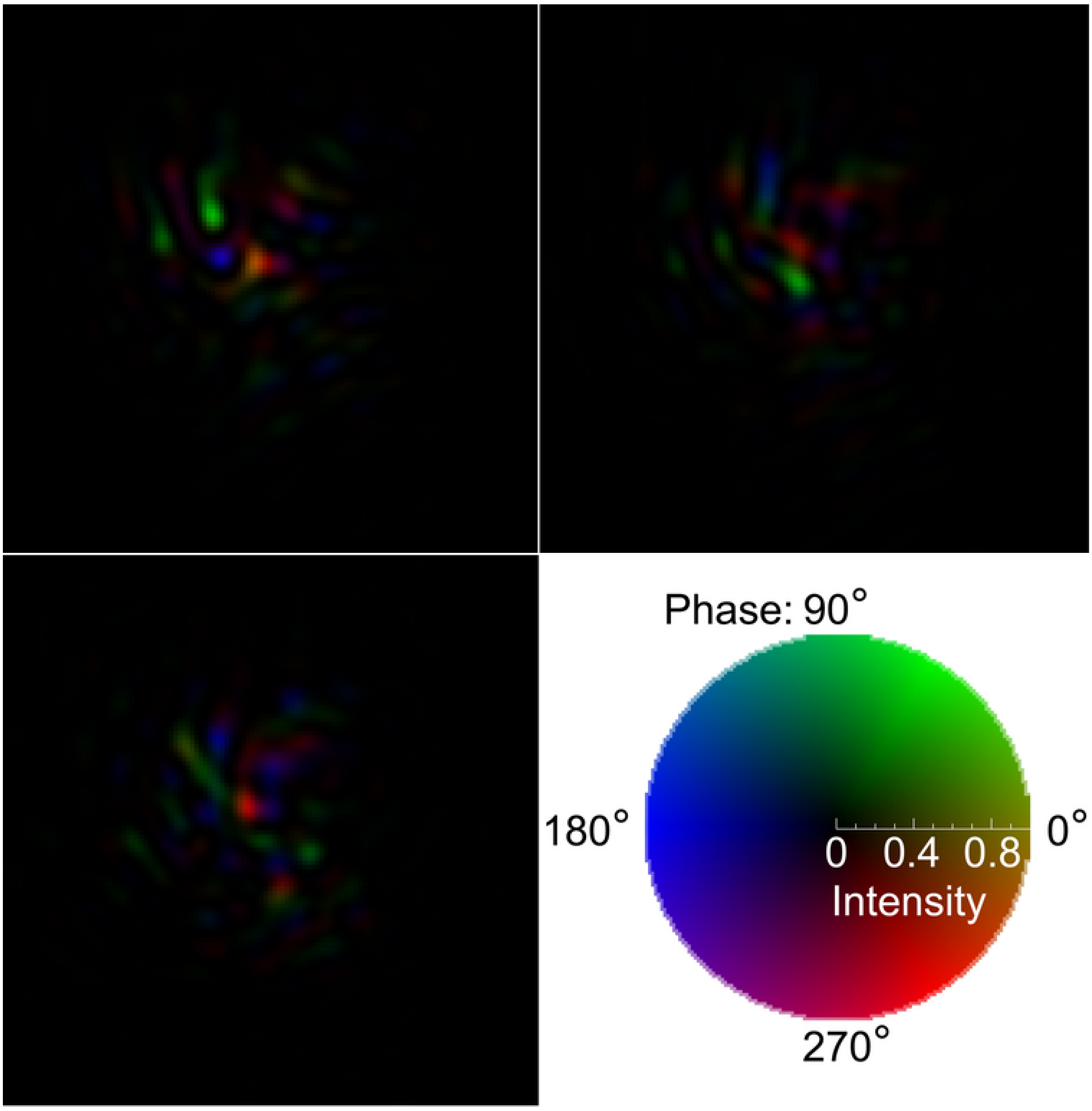

Figure 4: Phase and light intensity as a function of position in the image plane for a $9r_0$ diameter aperture. Three closely-separated time-points are shown starting on the top row (the piston mode changes by < 1 radian over the total time shown). The legend at the lower right indicates the dependence of *hue* and *brightness* on optical phase and intensity respectively.

5 WAVEFRONT AMPLITUDE AND PHASE FLUCTUATIONS ABOVE M1

5.1 Introduction

This section of the error budget intends to describe the optical wavefront amplitude and phase immediately before M1 sufficiently well that the simulations of the internal properties of the VLTI can be de-coupled from simulations of the atmosphere. Also included in this section is a discussion of the beam walk at high altitude resulting from bulk atmospheric refraction, as this can be separated from the details of the atmospheric seeing simulations.

The simulations described in Section 4 were used to investigate the approximate level of perturbation introduced into the optical wavefronts by the atmosphere. One of the main complexities in the design and operation of PRIMA is the wavelength dependence of the wavefront corrugations across the telescope pupil, and the resulting wavelength-dependent perturbations to the fringe phase induced by atmospheric seeing (further details of this can be found in Section 27). This results from the wavelength dependence of the phase perturbations caused by atmospheric seeing which are described as a function of position in the AT aperture plane by Equation 19.

In order to illustrate the wavelength dependence of seeing effects, I have plotted various wavefront properties in the first timestep of the simulations. The wavefronts at M1 were not directly output from the simulations, only the resulting wavefronts after tip-tilt correction had been performed (subtracting the tip-tilt Zernike modes). Figures 5 and 6 show the delay applied to the wavefronts by the atmosphere after the tip-tilt correction. Figure 5 shows the case for 1.97 μm wavelength and Figure 6 the case for 2.43 μm wavelength. Note that apart from the pixel sampling in the images there is no obvious difference. This is because the delay Δz from Equation 21 has only a weak dependence on wavelength.

A larger difference appears when the atmospheric delays are converted into optical amplitude and phase. The amplitude and phase in the pupil plane are shown in Figures 7 and 8 for the same timestep as used for Figures 5 and 6. Figure 7 shows the amplitude and phase at 1.97 μm wavelength plotted as a function of position in the AT aperture plane. The discontinuities in the phase occur when the phase wraps around by 2π radians. The same plots are shown in Figure 8 for 2.43 μm wavelength. It is clear that the phase perturbations are much more severe at 1.97 μm due to the inverse relationship of the phase ϕ with wavelength seen in Equation 21.

Example plots from 4 later timesteps of the simulations are shown in Figures 11 and 12.

Figure 11 shows the delay imposed on the wavefronts by the simulated atmosphere as a function of position in one of the AT aperture planes. The tip-tilt within the AT aperture has been corrected by perfectly compensating the tip and tilt Zernike modes, resulting in a discontinuity at the edges of the aperture in this plot. The four images show four timesteps with the atmospheric phase screens moving by $r_0/4$ in consecutive images in the directions described in Section 4. Each atmospheric layer has an equal effect on the wavefront phase.

Figure 12 shows the optical amplitude as a function of position in the same AT aperture plane. It is clear that the amplitude fluctuations are dominated by one of the layers moving from the lower left to the upper right. The dominant layer is the higher one (5 km above the telescope – see Section 4.2).

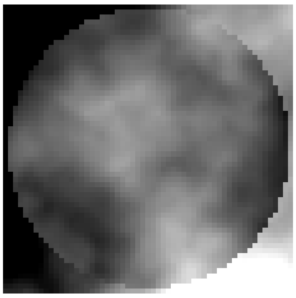

Figure 5: Atmospherically induced optical delay at one timepoint as a function of position in one AT aperture plane at 1.97 μm wavelength.

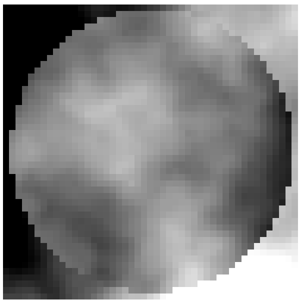

Figure 6: Optical delay at 2.43 μm wavelength at the same timepoint.

In both plots the tip-tilt Zernike modes have been corrected across the telescope aperture, resulting in a discontinuity at the edge of the aperture.

5.2 Dependencies

5.2.1 Error terms effected by this

Error term	Relevant subsection
Fringe jumps and group tracking errors	27.4
Wavefront corrugations before and after the STS	6.3
Atmospheric scintillation and thermal background fluctuations	25.3
Effect of aberrations in image plane optical components	14.3
Effect of aberrations in pupil plane optical components	16.3
VLTI baseline geometry	11.4

5.3 Detailed contributions

The largest contribution from atmospheric seeing on the measured astrometric parameters will be a zero mean process. Isoplanaticity will be the principle limitation on the separation of target star and reference star. Systematic errors in the astrometry can be generated in the STS calibration mode through a combination of seeing fluctuations and atmospheric refraction away from the zenith. This would encourage the use of an observing strategy where the PS and SS were switched regularly between alternate FSUs.

Atmospheric seeing is introduced through the combination of:

1. Atmospheric turbulence, typically between shearing wind layers

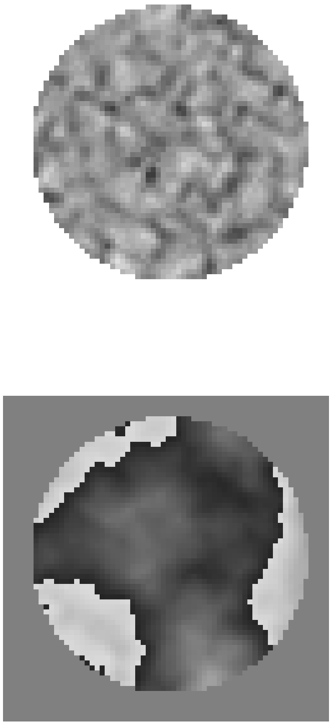

Figure 7: Optical amplitude (upper panel) and phase in the AT aperture plane at 1.97 μm wavelength. The discontinuities in the phase are due to the phase wrapping through 2π radians.

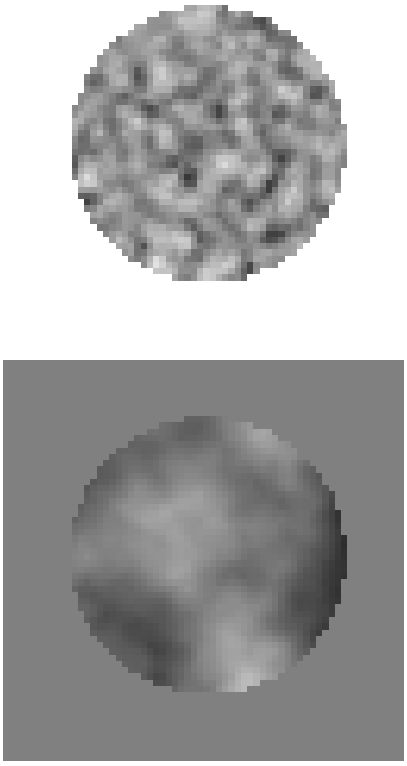

Figure 8: Optical amplitude and phase in the AT aperture plane at 2.43 μm wavelength.

These plots were produced from the wavefront corrugations shown in Figures 5 and 6. Note that larger amplitudes appear darker in the greyscale plots.

Figure 9: Intensity in the image plane at 1.97 μm wavelength

Figure 10: Intensity in the image plane at 2.43 μm wavelength

These plots were produced from the amplitude and phase data in Figures 7 and 8.

2. Fluctuations in the density of air or in the density of water vapour, due to changes in temperature, humidity and to a much lesser extent pressure

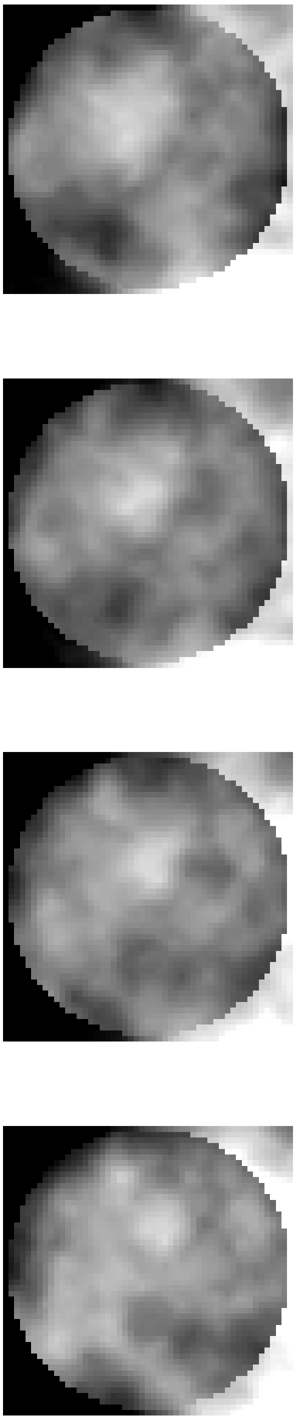

Figure 11: The delay in the wavefront in the AT aperture at four timesteps after the tip and tilt Zernike modes have been corrected.

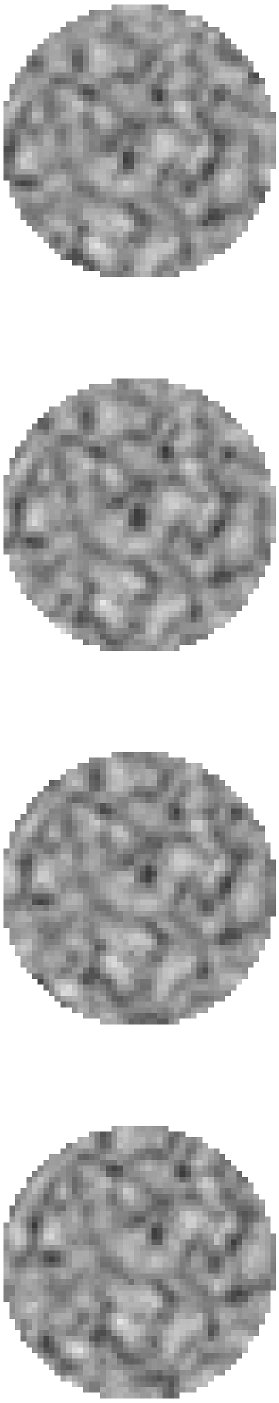

Figure 12: The corresponding optical amplitude in the AT aperture plane.

6 WAVEFRONT CORRUGATIONS BEFORE AND AFTER THE STS

6.1 Introduction

At several places in the VLTI some form of spatial filtering is performed, whereby the light from certain parts of the image plane is selected to continue along one path through the VLTI, and other light is rejected or sent along a different path. Spatial filtering processes such as this couple the Zernike piston mode to high-order Zernike modes, meaning that the piston mode in the interferometric beam is modulated according to the wavefront corrugations across the aperture plane, as well as modifying the spectral sensitivity distribution (see Section 4.3 for further details of both these effects). As a result, it is necessary to study in detail the expected wavefront corrugations immediately before each VLTI component which performs spatial filtering, which requires numerical simulations of the optical wavefronts at these locations. The first of these components is the STS, which separates the light from one star into two beams when operating in calibration mode. The separation of the beams is done using a roof mirror in the image plane which produces the same effect as a knife-edge test or Schlieren type wavefront detector (see [65, 192, 193]) in the individual output beams (with each output beam having the knife-edge on the opposite side of the image plane). The amplitude and phase of the output beams are thus strongly (and non-linearly) coupled to the wavefront corrugations in the input beam.

The STS calibration mode relies on both of the output beams from a single star having the same phase. In order investigate the expected performance of this calibration procedure it will be necessary to assess the amount of difference in the wavefront amplitude and phase expected in the two outputs from the STS.

6.2 Dependencies

The wavefront corrugations in the pupil plane immediately before the STS are expected to be closely related to the corrugations found immediately before M1 (see Section 5). The principle difference will be the tip-tilt correction from STRAP [147, §3.2.7.3], the effects of internal seeing within the AT, vibration of the optical components and the additional optical propagation distance.

6.2.1 This error term is effected by

Error term	Relevant subsection
Wavefront amplitude and phase fluctuations above M1	5.3
Internal vibration in the VLTI	22.3.1
Internal seeing within the VLTI	23.3

6.2.2 Error terms effected by this

Error term	Relevant subsection
Atmospheric scintillation and thermal background fluctuations	25.3
Fringe jumps and group tracking errors	27.4

6.3 Detailed contributions

For simulations of the STS calibration mode will be important to accuratly model the dependence of tip-tilt angle on wavelength and on the level of wavefront corrugation across the aperture plane in order to determine the following:

1. The mean and RMS differential phase between the two output channels in STS calibration mode, and the dependence of these parameters on the seeing and the atmospheric refraction and dispersion. This is very complicated, as the phase varies rapidly as a function of position in the image plane both before the STS splitting and in the output beams. Generally each speckle in the image has a arbitrary phase between 0 and 2π radians, independent of the other speckles in the image (see Section 4.3 for examples of this).
2. The mean and RMS colour difference between the light leaving the two output channels in STS calibration mode, and the dependence of these parameters on the seeing and the atmospheric refraction and dispersion. Again, the colour of the light varies as a function of position in the image plane of the STS.

Both of these factors depend on the detailed nature of the wavefront corrugation, and thus depend on all the seeing parameters and the STRAP performance.

Although knife-edge or Schlieren wavefront phase detectors are widely used in astronomy (and microscopy), the effect of such a system on the optical phase at the image plane focus is not well documented. The phase perturbations introduced by the atmosphere will be partially converted into amplitude fluctuations in the pupil plane wavefront. Where the amplitude is very low, substantial changes in the wavefront phase may also be observed. Chopping off a variable piece of the PSF $\sim J_1(2\pi r)/r$, is—after inverse Fourier Transform to reach the next pupil plane— modifying the real part of the effective image pupil as shown in Figure 13. The real part is even w.r.t. a sign flip in y, the imaginary part odd. (The fact that the image would not be formed on a plane surface has been ignored.) Passing all the light would reconstruct the full circular entrance pupil. The upper left example is equivalent to the "calibration" mode that cuts the star by half at $y = 0$, the other three examples limit the Airy disk to $y < \pm 0.4$ or $y < -0.8$.

The energy in the two axial sections outside the circular centric envelope would neither move on in the beam of the PS nor in the beam of the SS but soon be clipped by the finite apertures of the following VLTI optics. As a consequence shown with Figure 14, the value over the central part of the pupil flux for the "symmetric" edge at $y = 0$ is less than half of its value for the limit $y \to -\infty$. The dashed line is the fit

$$I \propto \mathrm{erfc}(3.4076(y + 0.0732)) \tag{22}$$

to the numerical data. Color effects appear because the dimensionless $y = \theta d/(2\lambda)$ is a function of the wavelength λ for a fixed off-axis angle θ and telescope diameter d. The derivative of the complementary error function in the previous equation is an exponential, which allows quick estimates of the effect. The summary in Figure 15 shows that the symmetric knife edge is not chromatic (as long as aligned with the atomspheric dispersion), whereas the other positions favor the "blue" over the "red" energy for the channel that gets the peak of the Airy disk [194].

The residual wiggles in the phase screen for varying distance of the knife edge from the center of the Airy disk are shown in Fig. 16. At a distance of $y = 1$, or 1.6 disk radii, the residual phase reaches up to $0.015 \cdot 2\pi$ (top graph). Moving the the edge away twice or three times as much (3.3 or 4.9 Airy disk radii) as shown at the middle and bottom of Fig. 16 introduces wiggles of smaller size, but keeps

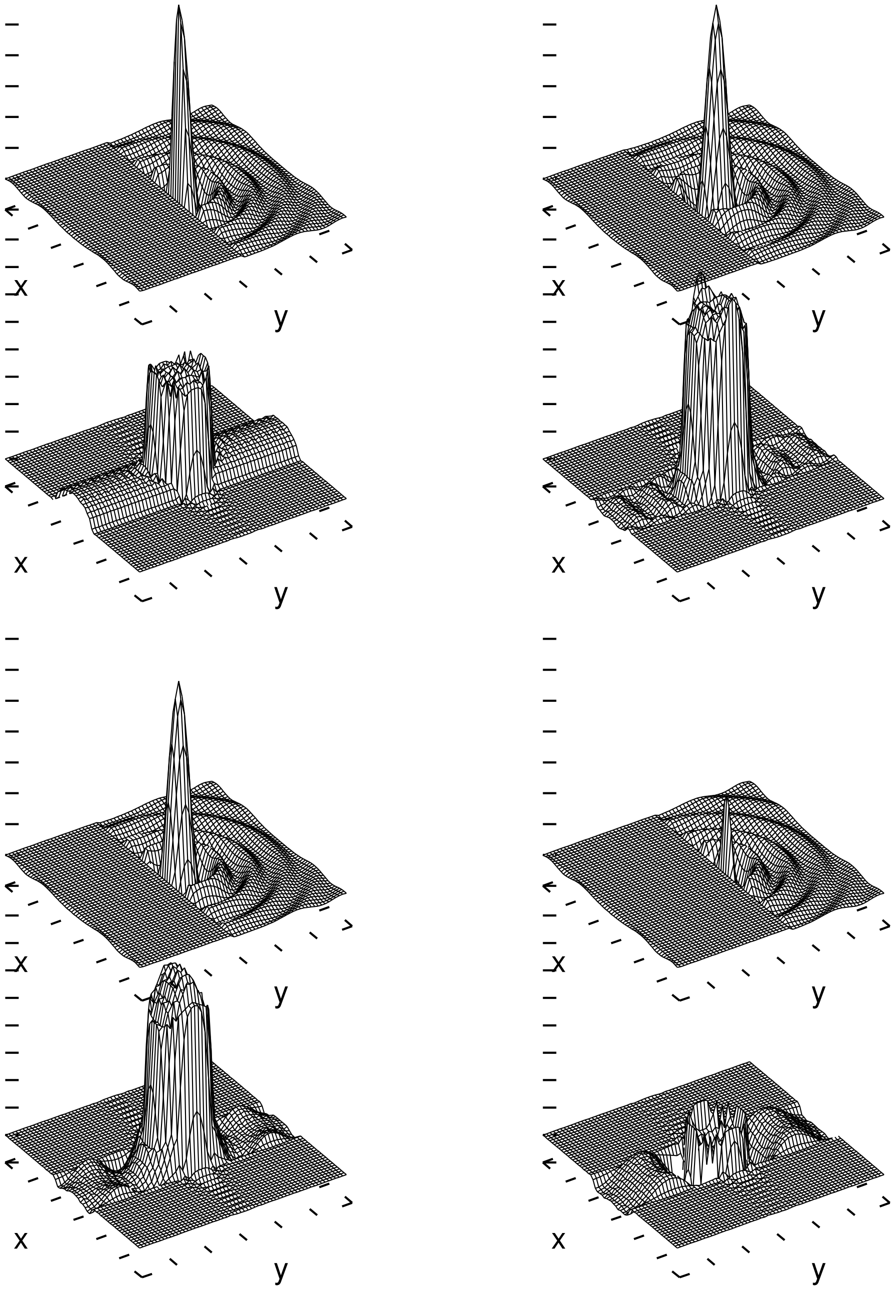

Figure 13: The diffraction effect of removal of some of the amplitude of the PSF by the STS on the original circular pupil image, shown as the real part of the inverse Fourier Transform of the cropped PSF.

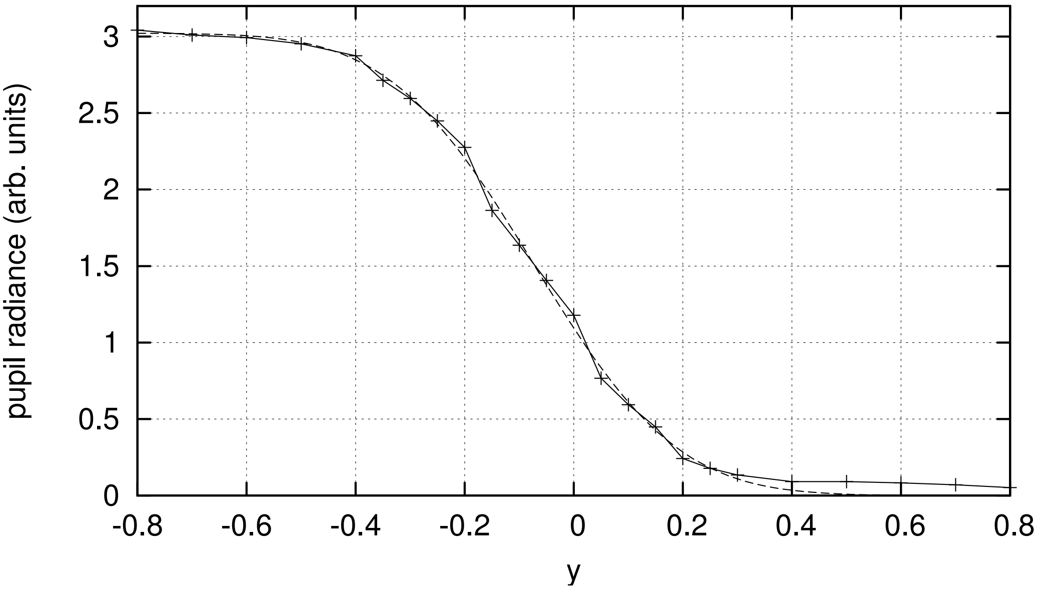

Figure 14: The integral over the squared modulus (the energy) remaining in the central circle of the re-imaged pupils of Fig. 13 as a function of the knife edge position. $y = \pm 0.61$ are the well-known limits of full inclusion or rejection of the central Airy peak.

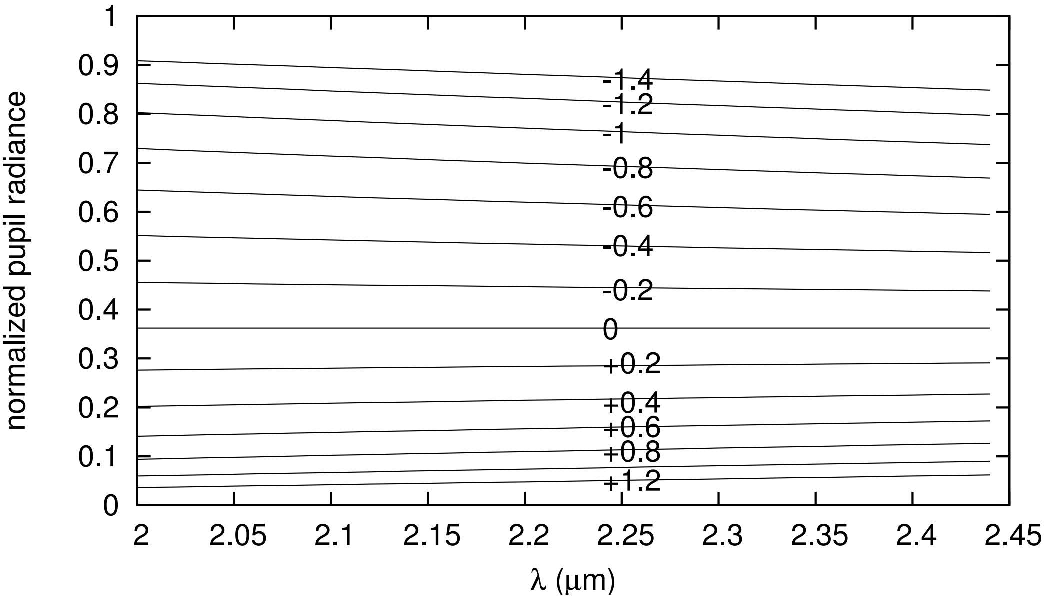

Figure 15: The energy I that remains in the original circular center of the pupil after the knife edge according to (22) for θd between -1.4μm and 1.2μm.

the size of the outermost buldge at about the same magnitude and pushes it outwards nearer to the edge of the geometrical pupil radius. This could be anticipated from the general performance of the Gibb's phenomenon of modeling discrete structures (here, the sharp edge of the original amplitude with perfect contrast across the pupil) through waves limited in the Fourier domain. One Airy disk radius is ≈ 100 μm on M10 of the STS (Sect. 14.1), or about 0.4 % of the mirror radius of 25 mm.

In order to assess the impact of the STS roof mirror on interferometric observations, the simulations discussed in Section 4 were modified to include a knife-edge in the image plane. The pupil plane wavefront properties before and after the knife-edge in one timestep from the simulations can be seen in Figures 17 to 22. Figures 17 and 20 show wavefronts entering the STS for this timestep (identical to Figures 7 and 8, although the amplitude is plotted with a different greyscale). The effect of the wavefront corrugations in the input beam on the wavefront amplitude in the output beams is very strong – this is not surprising as the principle use of image plane knife-edges is in visualising wavefront corrugations (see e.g. [83, 192, 193]). These amplitude fluctuations are much larger than those produced by atmospheric scintillation, and may impede the fringe-tracking performance. Note that the knife-edge also diffracts a significant amount of light out of the beam.

It is clear that detailed simulations will be required in order to determine the expected optical phase and colour differences between the two beams output from the STS when it is operating in calibration mode. The two output beams will be swapped periodically using the de-rotator, so it will be important to look for effects which couple the differential phase in the output beams to the angle of the de-rotator.

6.4 Conclusion

The definition "*dual feed. An optical system, at a telescope focus, capable to select two narrow field-of-view beams: a primary one on-axis and a secondary one off-axis within a certain maximum radius.*" on page 11 of [31] does not apply to PRIMA which better avoids an asymmetric treatment of the two stars.

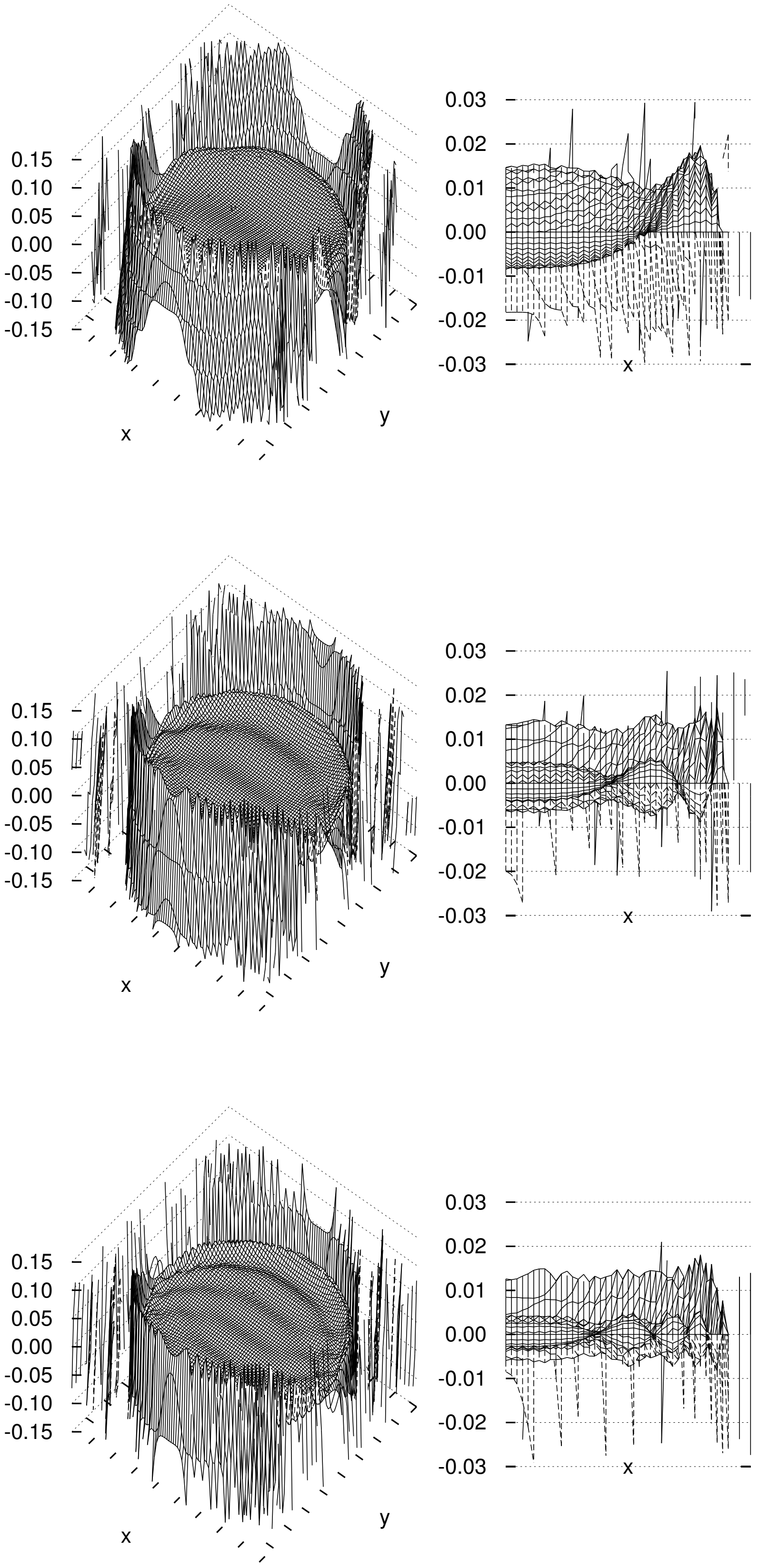

Figure 16: Phases across the pupil in units of 2π left over if the knife edge is $y = 1$ (top), 2 (middle) or 3 (bottom) units away from the Air disk center. Outside the circular pupil, the wrapped phases are more or less chaotic.

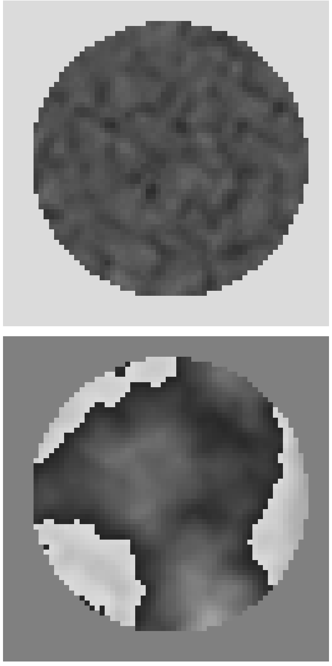

Figure 17: Optical amplitude (upper panel) and phase at 1.97 μm wavelength in the aperture plane before the STS.

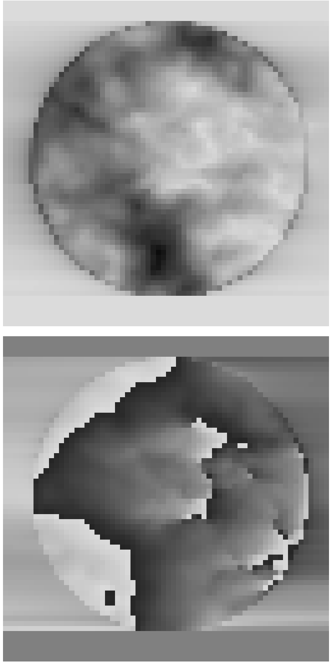

Figure 18: Optical amplitude (upper panel) and phase at 1.97 μm in the aperture plane after an image-plane knife-edge.

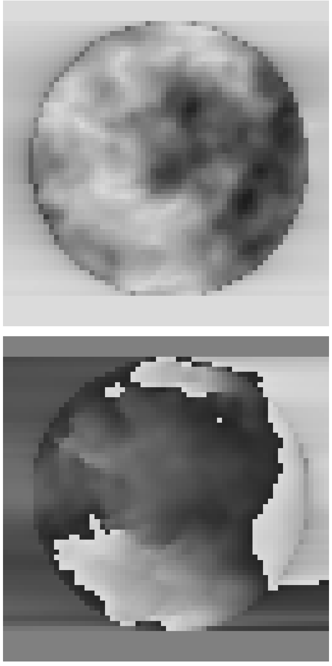

Figure 19: Optical amplitude and phase with the opposite knife-edge (corresponding to the other beam from the STS).

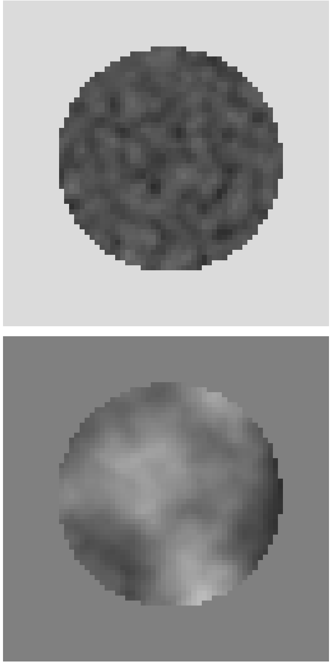

Figure 20: Optical amplitude (upper panel) and phase at 2.43 μm wavelength in the aperture plane before the STS.

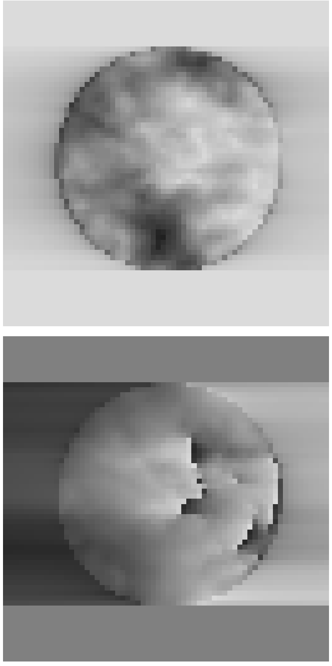

Figure 21: Optical amplitude (upper panel) and phase at 2.43 μm in the aperture plane after an image-plane knife-edge.

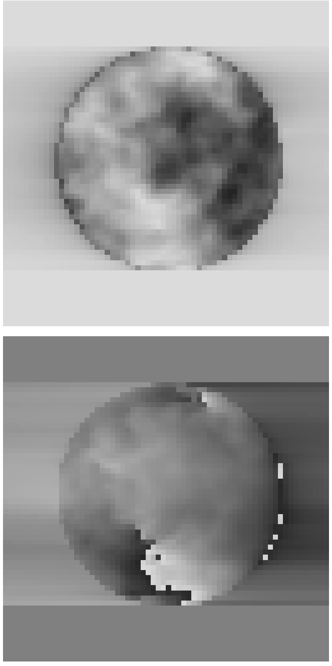

Figure 22: Optical amplitude and phase with the opposite knife-edge (corresponding to the other beam from the STS).

7 WAVEFRONT CORRUGATIONS BEFORE VCM

7.1 Introduction

The VCM in the VLTI [51, 52, 53] couple the Zernike piston mode to high-order Zernike modes, meaning that the piston mode in the interferometric beam is modulated according to the wavefront corrugations across the aperture plane. This may cause the astrometric phase to depend on the seeing conditions, the performance of the STRAP units or the effects of vibration. For this reason the wavefront corrugations expected immediately before the VCM will be investigated in detail here.

7.2 Dependencies

7.2.1 This error term is effected by

Error term	Relevant subsection
Wavefront corrugations before and after the STS	6.3
Internal vibration in the VLTI	22.3.1
Internal seeing within the VLTI	23.3

7.2.2 Error terms effected by this

Error term	Relevant subsection
Effect of aberrations in image plane optical components	14.3

8 WAVEFRONT CORRUGATIONS BEFORE FSU SPATIAL FILTER

8.1 Introduction

At several places in the VLTI some form of spatial filtering is performed, whereby the light from certain parts of the image plane is selected to continue along one path through the VLTI, and other light is rejected or sent along a different path. Spatial filtering processes such as this couple the Zernike piston mode to high-order Zernike modes, meaning that the piston mode in the interferometric beam is modulated according to the wavefront corrugations across the aperture plane, as well as modifying the spectral sensitivity distribution (see Section 4.3 for further details of both these effects). As a result, this document will study in detail the expected wavefront corrugations immediately before each VLTI component which performs spatial filtering. The second of these components is the FSU spatial filter, which selects the light from one speckle in the telescope image plane, see Section 21.3.

Previous studies of the temporal properties of interferometric fringes indicate that the high-frequency fringe motion is dominated by the effects of wavefront corrugations across the aperture plane when the variance in the wavefront phase across the aperture is $\gtrsim 1$ radian. For this reason it will be essential to simulate the level of wavefront corrugation expected in order to determing the performance of the fringe tracker.

Error term	Relevant subsection
Internal vibration in the VLTI	22.3.1
Internal seeing within the VLTI	23.3

8.1.1 Error terms effected by this

Error term	Relevant subsection
Fringe jumps and group tracking errors	27.4
Systematic errors in the FSU phase	19.3
Atmospheric scintillation and thermal background fluctuations	25.3
Effect of aberrations in image plane optical components	14.3

9 REFRACTIVE INDEX OF AIR AND COLOUR OF CORRELATED FLUX

9.1 Introduction

The variation of refractive index with wavelength in the ducts, tunnels and laboratory, and the dependence of the measured astrometric phase on the colour of the correlated flux.

This document gives an order-of-magnitude calculation for the impact of air in the VLTI on differential astrometry. Both the main delay line and differential delay line are assumed to be filled with air. Some error terms are larger per metre air path offset of the DDL than per metre air path offset of the main delay line (notably errors from the uncertainty in the environmental conditions in the VLTI, and uncertainty in empirical/theoretical models for the dispersion in air and water vapour in the near infrared). Other error terms are larger per metre air path offset of the main delay line than per metre air path offset of the DDL (notably errors due to the uncertainty in the stellar wavelength/temperatures).

Errors resulting from the uncertainty in the environmental conditions in the VLTI are found to be negligible, while the errors due to the uncertainty in the stellar temperatures are found to be too large to allow accurate astrometric measurement unless the spectral resolution of PRIMA is enhanced, or a novel method is found for determining the centroid of the correlated flux from each star.

The PRIMA facility is intended to measure differential OPD to an accuracy of 5nm in order to allow astrometric detection of the motion of stars due to orbiting planets [102, 182]. The light from astronomical sources will be passed along air-filled ducts and tunnels in the VLTI, and the primary OPD correction will be performed in an air-filled delay line. In order to calculate the performance of the VLTI it will be necessary to know the refractive index of air in the VLTI in the observing bandpass and at the wavelength of the metrology lasers. Recent studies of the refractive index of air at near infrared wavelengths agree within $5 \cdot 10^{-8}$ in the K band concerning the influence of airbourne water vapour, but this modeling is futile unless the knowledge on the time-dependent and inhomogeneous gas concentrations in the light paths does not match that precision [119].

9.2 Dependencies

9.2.1 Error terms effected by this

Error term	Relevant subsection
Fringe jumps and group tracking errors	27.4

9.3 Detailed contributions

If both the main delay line and differential delay line are filled with air, then the measured distances within the VLTI must be converted to OPD at the observing wavelength for each star. The observing wavelength for each star is the centroid of the correlated flux detected for that star [124]. If the observing wavelength of the primary star is λ_{ps}, the observing wavelength of the secondary star is λ_{ses} and the metrology wavelength is λ_m, then the coarse OPD measured by one metrology arm is $n_{\lambda_m} D$, by the other laser arm $n_{\lambda_m}(D + X)$, where D is the GPD introduced by the main delay line and X the GPD added by the DDL. The metrology phase meter reports the difference $M = n_{\lambda_m} X$ between these at high resolution. The two OPDs sensed by the two detectors are $n_{\lambda_{ps}}D$ and $n_{\lambda_{ses}}(D+X)$. The astrometric variable of interest is the difference between these two, which equals the difference in the GPDs above the atmosphere, if the lensing effects of Section 26.1 are put aside:

$$\begin{aligned} n_{\lambda_{ses}}(D+X)-n_{\lambda_{ps}}D &= n_{\lambda_{ses}}\left(D+\frac{M}{n_{\lambda_m}}\right)-n_{\lambda_{ps}}D \qquad (23)\\ &\approx M+M\left(n_{\lambda_{ses}}-n_{\lambda_m}-[n_{\lambda_{ses}}-1][n_{\lambda_m}-1]\right)+D\left(n_{\lambda_{ses}}-n_{\lambda_{ps}}\right). \qquad (24)\end{aligned}$$

The second term on the right hand side of Equation 24 corresponds to the effect of the air in the DDL, but becomes more complicated with the vacuum option [101]; the third term correponds to the effect of the air in the main delay line. The approximation up to second powers in the refractivities in Equation 24 is fully valid for this error analysis due to the low refractivity of air. Note that there is *no* correction term $\propto D(n_{\lambda_m}-n_{\lambda_{ps}})$ or $\propto D(n_{\lambda_m}-n_{\lambda_{ses}})$.

We wish to measure ΔD:

$$\Delta D = M+M\left(n_{\lambda_{ses}}-n_{\lambda_m}-[n_{\lambda_{ses}}-1][n_{\lambda_m}-1]\right)+D\left(n_{\lambda_{ses}}-n_{\lambda_{ps}}\right). \tag{25}$$

The conversion from M would be done using the best estimates of $n_{\lambda_{ses}}$ and $n_{\lambda_{ps}}$ available. The error $\epsilon\left(\Delta D\right)$ in the differential OPD measurement ΔD can be separated into a number of principle terms:

$$\epsilon\left(\Delta D\right)=\epsilon\left(M\right)+M\epsilon\left(n_{\lambda_{ses}}-n_{\lambda_m}\right)+D\epsilon\left(n_{\lambda_{ses}}-n_{\lambda_{ps}}\right) \tag{26}$$

where

$$\epsilon\left(n_{\lambda_{ses}}-n_{\lambda_m}\right) \tag{27}$$

is the error in estimation of $n_{\lambda_{ses}}-n_{\lambda_m}$,

$$\epsilon\left(n_{\lambda_{ses}}-n_{\lambda_{ps}}\right) \tag{28}$$

is the error in estimation of $n_{\lambda_{ses}}-n_{\lambda_{ps}}$ and

$$\epsilon\left(M\right) \tag{29}$$

is the (hopefully insignificant) error in the ability of the metrology system to count laser wavelengths. The value of $M[n_{\lambda_{ses}}-1][n_{\lambda_m}-1]$ is less than 7 nm with negligible error.

The error terms in Equations (27) and (28) can be further broken down by taking partial derivatives. Error terms from time derivatives (clocks) are described separately in App. 29.

$$\begin{aligned} Z &= XY \qquad (30)\\ \Delta Z &= \Delta X\frac{\partial\left(XY\right)}{\partial X}+\Delta Y\frac{\partial\left(XY\right)}{\partial Y} \qquad (31)\end{aligned}$$

Applying this approach to Equation (27) yields:

$$\epsilon\left(n_{\lambda_{ses}}-n_{\lambda_m}\right) = \left\{\begin{array}{l} \epsilon\left(\rho_a\right)\frac{\partial\left(n_{\lambda_{ses}}-n_{\lambda_m}\right)}{\partial\rho_a}+\epsilon\left(\rho_w\right)\frac{\partial\left(n_{\lambda_{ses}}-n_{\lambda_m}\right)}{\partial\rho_w}\\ +\epsilon\left(\lambda_{ses}\right)\frac{\partial\left(n_{\lambda_{ses}}-n_{\lambda_m}\right)}{\partial\lambda_{ses}}+\epsilon\left(\frac{\Delta(n_\lambda)}{\Delta\lambda}\right)\left(n_{\lambda_{ses}}-n_{\lambda_m}\right)\end{array}\right. \tag{32}$$

$$\epsilon\left(n_{\lambda_{ses}}-n_{\lambda_{ps}}\right) = \left\{\begin{array}{l} \epsilon\left(\rho_a\right)\frac{\partial\left(n_{\lambda_{ses}}-n_{\lambda_{ps}}\right)}{\partial\rho_a}+\epsilon\left(\rho_w\right)\frac{\partial\left(n_{\lambda_{ses}}-n_{\lambda_{ps}}\right)}{\partial\rho_w}\\ +\epsilon\left(\lambda_{ses}\right)\frac{\partial\left(n_{\lambda_{ses}}-n_{\lambda_{ps}}\right)}{\partial\lambda_{ses}}+\epsilon\left(\lambda_{ps}\right)\frac{\partial\left(n_{\lambda_{ses}}-n_{\lambda_{ps}}\right)}{\partial\lambda_{ps}}\\ +\epsilon\left(\frac{\Delta(n_\lambda)}{\Delta\lambda}\right)\left(n_{\lambda_{ses}}-n_{\lambda_{ps}}\right)\end{array}\right. \tag{33}$$

Table 2: Individual components of the error terms listed in Equation 32

Term	Typical value	Units
$\epsilon\left(\rho_a\right)$	0.002	fractional error
$\frac{\partial\left(n_{\lambda_{ses}}-n_{\lambda_m}\right)}{\partial\rho_a}$	5×10^{-7}	$\frac{\text{fractional change}}{\text{fractional change}}$
$\frac{\partial\left(n_{\lambda_{ses}}-n_{\lambda_{ps}}\right)}{\partial\rho_a}$	5×10^{-9}	$\frac{\text{fractional change}}{\text{fractional change}}$
$\epsilon\left(\rho_w\right)$	0.01	fractional error
$\frac{\partial\left(n_{\lambda_{ses}}-n_{\lambda_m}\right)}{\partial\rho_w}$	2×10^{-8}	$\frac{\text{fractional change}}{\text{fractional change}}$
$\frac{\partial\left(n_{\lambda_{ses}}-n_{\lambda_{ps}}\right)}{\partial\rho_w}$	8×10^{-11}	$\frac{\text{fractional change}}{\text{fractional change}}$
$\epsilon\left(\lambda_{ses}\right)$	2	nm
$\frac{\partial\left(n_{\lambda_{ses}}-n_{\lambda_m}\right)}{\partial\lambda_{ses}}$	2.5×10^{-10}	$\frac{\text{fractional change}}{\text{nm}}$
$\frac{\partial\left(n_{\lambda_{ses}}-n_{\lambda_{ps}}\right)}{\partial\lambda_{ses}}$	2.5×10^{-10}	$\frac{\text{fractional change}}{\text{nm}}$
$\epsilon\left(\lambda_{ps}\right)$	2	nm
$\frac{\partial\left(n_{\lambda_{ses}}-n_{\lambda_{ps}}\right)}{\partial\lambda_{ps}}$	2.5×10^{-10}	$\frac{\text{fractional change}}{\text{nm}}$
$\epsilon\left(\frac{\Delta(n_\lambda)}{\Delta\lambda}\right)$	Unknown in the near infrared	

where ρ_a is the air density and ρ_w is the water vapour density in the VLTI. $\epsilon\left(\frac{\Delta(n_\lambda)}{\Delta\lambda}\right)$ is the uncertainty in the model for dispersion of the air and water vapour in the VLTI between two wavelengths.

A term in (33) that originates from a refractive index bias associated with horizontal temperature differences is not written down here but discussed in [119]. It is less serious as it can be suppressed by beam switching, with estimated residual errors summarized in [117].

Typical values of the components making up these error terms are listed in Table 2. The transition of $\epsilon(\lambda)$ to star temperatures could be made utilizing the last page of [38].

From Table 2 we can calculate approximate magnitudes for the error terms listed in Equation 32 for the air path in the DDL:

Term	Description	m ΔOPD per m DDL air
$\epsilon\left(\rho_a\right)\frac{\partial\left(n_{\lambda_{ses}}-n_{\lambda_m}\right)}{\partial\rho_a}$	The effect of 0.2% uncertainty in the density of the air in the DDL, due to uncertainties in temperature (and, negligible, in pressure)	1×10^{-9}
$\epsilon\left(\rho_w\right)\frac{\partial\left(n_{\lambda_{ses}}-n_{\lambda_m}\right)}{\partial\rho_w}$	The effect of 1% uncertainty in the density of the water vapour in the DDL, due to uncertainties in relative humidity (0.2% out of 20%), and to lesser extent temperature and pressure	2×10^{-10}
$\epsilon\left(\lambda_{ses}\right)\frac{\partial\left(n_{\lambda_{ses}}-n_{\lambda_m}\right)}{\partial\lambda_{ses}}$	The effect of a 2 nm uncertainty in the centroid wavelength of the correlated flux from secondary star	5×10^{-10}
$\epsilon\left(\frac{\Delta(n_\lambda)}{\Delta\lambda}\right)\left(n_{\lambda_{ses}}-n_{\lambda_m}\right)$	The reliability of the refractive index models. It represents incomplete accounting of H_2O resonances in the near infrared of extrapolated experimental results [119].	$< 1.4\times10^{-8}$

The term $\epsilon\left(\frac{\Delta(n_\lambda)}{\Delta\lambda}\right)(n_{\lambda_{ses}} - n_{\lambda_m})$ dominates the OPD error per metre air path in the DDL; it corresponds to 1.7 nm error for 12 cm of air path in the DDL. The term is to be replaced by a similar calculation for the DDL windows [101] if the DDL is evacuated.

From Table 2 we can also calculate approximate magnitudes for the error terms listed in Equation 33 for the air path in the main delay lines and AT ducts which is balancing vacuum path (distance of the main delay line from that of equal OPD to the two telescopes):

Term	Description	m ΔOPD per m air
$\epsilon(\rho_a)\frac{\partial\left(n_{\lambda_{ses}}-n_{\lambda_{ps}}\right)}{\partial\rho_a}$	The effect of 0.2% uncertainty in the density of the air in the main delay line, due to uncertainties in temperature and pressure	1×10^{-11}
$\epsilon(\rho_w)\frac{\partial\left(n_{\lambda_{ses}}-n_{\lambda_{ps}}\right)}{\partial\rho_w}$	The effect of 1% uncertainty in the density of the water vapour in the main delay line, due to uncertainties in relative humidity, temperature and pressure	8×10^{-13}
$\epsilon(\lambda_{ses})\frac{\partial\left(n_{\lambda_{ses}}-n_{\lambda_{ps}}\right)}{\partial\lambda_{ses}}$	The effect of a 2 nm uncertainty in the centroid wavelength of the correlated flux from secondary star	5×10^{-10}
$\epsilon(\lambda_{ps})\frac{\partial\left(n_{\lambda_{ses}}-n_{\lambda_{ps}}\right)}{\partial\lambda_{ps}}$	The effect of a 2 nm uncertainty in the centroid wavelength of the correlated flux from primary star	5×10^{-10}

with an additional term $\propto \epsilon\left(\frac{\Delta(n_\lambda)}{\Delta\lambda}\right)$ from the dispersive properties of air, which is currently unknown in the K band, but certainly less than the slope itself, $\frac{\Delta(n_\lambda)}{\Delta\lambda} \approx 0.25$/m. [The transition from $\epsilon(\lambda)$ to star temperatures could be made utilizing the last page of [38]; for temperatures from 5,000 K to 25,000 K, $\lambda_{ses} - \lambda_{ps}$ cannot exceed $4 \times 10^{-3}\mu$m, which yields a solid, pessimistic upper bound $\left(n_{\lambda_{ses}} - n_{\lambda_{ps}}\right) < 9 \times 10^{-10}$]. or $\epsilon\left(\frac{\Delta(n_\lambda)}{\Delta\lambda}\right)\left(n_{\lambda_{ses}} - n_{\lambda_{ps}}\right) < 1 \times 10^{-9}$].

If the refractive indices of air and water vapour can be measured with sufficient reliability, it is clear that the error in the colour of the observing band for the primary and secondary stars will dominate the contribution from air in the main delay line, giving a total error contribution of (summing errors in quadrature):

$$\epsilon\left(n_{\lambda_{ses}} - n_{\lambda_{ps}}\right) \simeq 7 \times 10^{-10} \tag{34}$$

in units of metres of OPD error per metre of air path compensating vacuum path with the main delay lines. This corresponds to 70 nm differential OPD error for 100 m of air path in the main delay line. Read backwards, an error of 0.4 cm^{-1} in the effective (spectroscopic) wavenumber difference between the two stars is equivalent to 5 nm in DOPD at $D = 100$ m. A marginally more optimistic conclusion (for a shallower dispersion) is drawn in [132, Table 2.2].

The statistical approach of Milman [129] is not available to overcome this wide-band problem as long as stepping is not introduced into the arsenal of the fringe tracker.

9.4 Conclusion

If an accurate model for the refractive index is obtained, then an error budget for the effects of air in the VLTI can be constructed. The error due to the uncertainty in stellar temperature and stellar spectrum is currently too large to meet the astrometric accuracy requirements for the analysis of the differential OPD in the tunnel. This error scales as $\frac{1}{R^2}$ for stellar temperature uncertainties where R

is the spectral resolution of PRIMA. However, this dispersive term is meeting another term in the data reduction—see Eq. (6) in [120]—which cancels an error in the stars spectrum to a very high degree. A small increase in the spectral resolution of PRIMA should allow accurate astrometry to take place.

10 POLARISATION EFFECTS

10.1 Introduction

This component of the error budget is studied in [131] for the instrumental polarization. The influence of the K-prism that is part of the FSU is discussed in [119]. Influences of the earth atmosphere [13] or polarization of the astronomical source [172, 189] are not yet considered.

10.2 Dependencies

An experimental campaign to measure the actual VLTI polarization similar to what has been done for the VTT [16] would be needed to parametrize a polarization model for PRIMA or VITRUV [103].

10.2.1 Error terms effected by this

Error term	Relevant subsection
Systematic errors in the FSU phase	19.3

11 VLTI BASELINE GEOMETRY

11.1 Introduction

The ray geometry of the two stars beam following the AT/STS mirror train is sketeched in Fig. 23. The simplest principle of measuring the angle τ between the two wavefronts is to determine the two tip-tilt angles of the individual M11/FSM needed to turn both wave vectors parallel, and detect when this is the case with some imaging (focussing) optics (camera plus array detector) that follows.

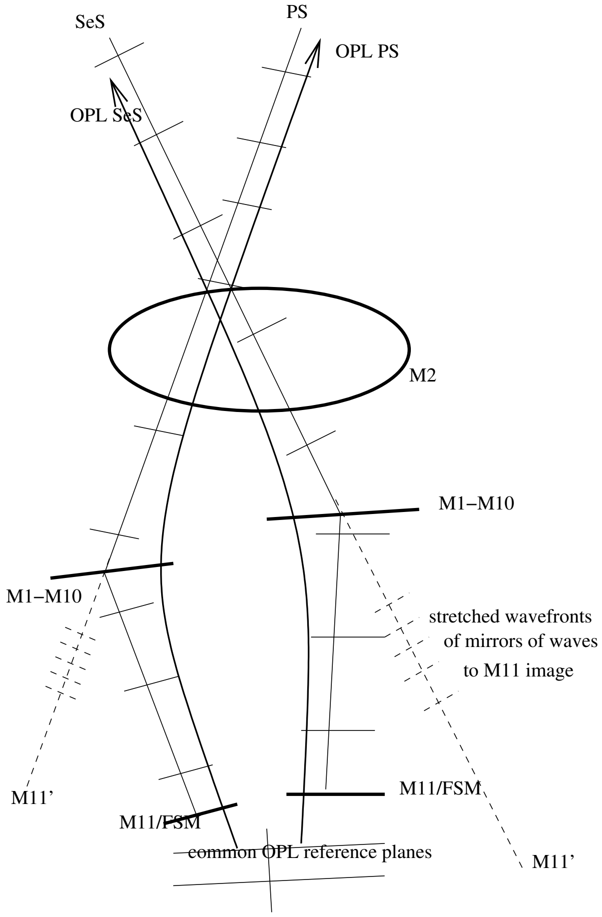

Figure 23: Common parallel wavefronts in the observation of off-axis stars are only achieved after they have passed their associated M11/FSM leaving for M12 (of the STS). Up to this point, the rays pick up phase/optical path length which is a function of the off-axis angle, but not easily convertible to (differential) sky angles. The virtual wavefronts of the two beams after the M11/FSM images are not necessarily parallel, even though the real PWs after the real M11/FSM are.

The rotation angles of the M11/FSM in the lab would be scaled by a factor of 36 (Tab. 9) to angles on the sky to account for the angular magnification of M1–M10. An alternative interpretation of the same optics is to determine the angle between the normal vectors of the M11/FSM *images* as seen from above M1, at an angular magnification of one. The angular resolution of this approach would be set by the PSF of the single telescope. PRIMA astrometry uses a different, interferometric setup to enhance this resolution. The message of what is said above is that postponing/relaying the sensing of these angles to the FSM of the STS is a characteristic of the 2-beam optics, even though methologies to measure these may differ.

11.2 Baseline Terminology

11.2.1 Wide Angle Baseline

The meaning of baseline endpoints to interferometry is to assist in the definition of different tilts of incoming wavefronts; for each telescope, it is the point in the optics, where the "accumulation" of phase/path length ends such that one corner of the "fundamental" triangle of OPD D, baseline b and projected baseline at directional angle a,

$$D = b \cos a, \tag{35}$$

can be pinned down there: Fig. 24. Turning this into a definition for a particular optical layout means

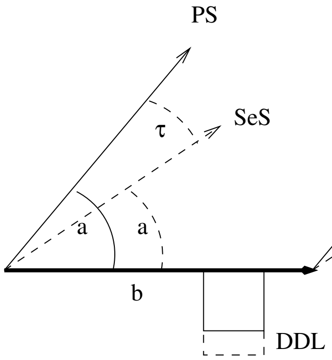

Figure 24: This geometry is the building block of combining the pointing directions a to the two different stars and the baseline vector to their angular separation τ, used in Sect. 32.2.

to locate the axis of the last mirror that turns beams from any direction on the sky into the same direction of a "common" wavefront. In a wide-angle use of the VLTI telescopes which are pointed with their axes to individual stars, this is realized by M3—the baseline vector definition adopted in the glossary of [6, 7, 8]—as long as the tip-tilt action of M6 is neglected.

This is the optical interpretation of the interferometric principle of selecting two sub-apertures of the infinitely broad plane wavefront that approaches both telescopes. Once (i) a subaperture has selected a slice of the wavefront, and (ii) the wave vector leaves the aperture parallel to the surface normal, an optical train that faithfully maps pupil plane on pupil plane can "preserve" the phase of the sub-aperture in the sense that it can be controlled "linearly" by positioning a delay line reflector. (The PW passing through a pupil matches the plane mirror as the controller. Other wavefronts or modes, spherical wave fronts or Gaussian Beams for example, would need more complicated phase manipulators.) We see that—aside from shaping the OTF—the baseline conceptionally connects two phase-aperture stops such that the subsequent relay to the beam combiner becomes a matter of bookkeeping the (optical) path length travelled until then.

11.2.2 Narrow Angle Baseline

Narrow angle astrometry [79] with PRIMA looks at the same time at two off-axis stars, and the common parallel wavefronts are only realized after leaving the two M11/FSM (Fig. 23). An on-axis ray traced back from the FSU through the mirror chain emerges at different angles above M1 depending on the tip/tilt of M11/FSM, which points on different areas of M10. In that sense PRIMA runs two interferometers in parallel, defining two baseline vectors between the four M11/FSM of the two telescopes, revealing additional "internal structure" as we zoom into what are only geometric points in Fig. 24, reaching Fig. 25.

In principle, this fact that the two baseline vectors start at two different places about 17 cm apart in the U coordinate does not matter as long as the three components of these two baseline vectors are the same. One could then virtually move one of them and the pointing vectors $\mathbf{s}$ attached to it until one is back to the case of a common baseline as in Fig. 24. On second thought, this argumentation is not applicable because shifting rays means shifting the optical surfaces, including the M2 pupil, by the same amount; this associated relocation of the entrance pupil that defines some mean reference for the wavefronts would call for a correction of the reference point of the OPL for this star depending on the differential overlap between the actual and the shifted pupil. Thinking over again, this effect cancels if we construct variables that depend only on the OPD's of the two stars—to the degree that the two telescopes are identical. (The 17 cm are not equivalent to ≈ 17 cm in LST, although the U coordinate is running almost East-West, because they keep the baselines parallel and do not have a rotational component.) For the *individual* telescope, passing with a beam off-axis through the pupil violates our aforementioned criterion for a baseline: defining a phase reference point in the middle of the pupil for a wave front parallel to the pupil. Re-definition of the pupil to match that criterion involves a rotation *plus* a translation where a reference for the translation remains undefined. For a *pair* of identical telescopes, this undefined/arbitrary amount of translation along the wave vector cancels, and only secondary effects (like an elliptical shape of the PSF [33]) remain.

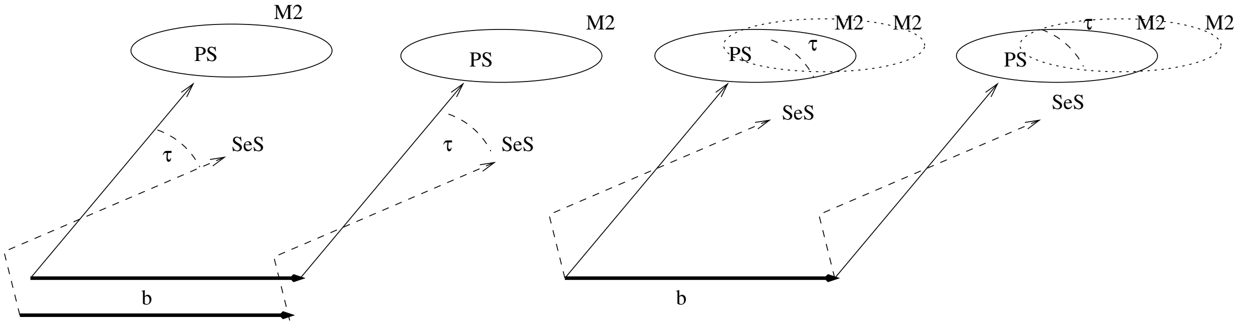

Figure 25: Left: A closer look at the baseline end points of Fig. 24 displays four pickup mirrors M11/FSM at the two telescopes with two baseline vectors, one for the PS and one for the SS. Right: If one of the baseline vectors is shifted to match the other, an additional virtual pair of M2 pupils for the associated star is also created.

11.2.3 (Internal) Metrology

The metrology light path and retroreflector system in the STS [133] have been designed to map it onto its own return path for any of the M11/FSM pointing directions [133]: the narrow angle astrometry baseline is *defined* by the M11/FSM, but *determined* by the end point of the metrology system (in the STS). The metrology system can be viewed as measuring the distance from a FSU endpoint in the laboratory to an image plane in the STS, situated close to the roof mirror M10 which separates the beams from the two stars in the STS. In this way the metrology system is creating a virtual reference surface within the ATs against which the narrow angle astrometry is performed.

See Section 15.1 for further details.

11.3 Dependencies

11.3.1 This error term is effected by

Error term	Relevant subsection
Image plane optics in the star separator	15.3
Ground level temperature, humidity and pressure fluctuations	E.3.2
Wavefront amplitude and phase fluctuations above M1	5.3

The dependence on the combination of telescope and delay line is obvious; for illustration, table 3 shows the X and Y components of the E0–G0 baseline that have been generated with `IPHASE` [184] in the past two years, with typical variations on the 300 μm scale.

T1	T2	Date	T1X (m)	T1Y (m)
dl2AT1G0	dl1AT2E0	2005-02-03	-15.134 336 787	-5.208 439 957
dl6AT3G0	dl5AT2E0	2005-03-30	-15.135 552 946	-5.208 422 566
dl2AT2G0	dl1AT1E0	2005-05-11	-15.135 980 062	-5.209 041 393
dl6AT2G0	dl5AT1E0	2005-11-07	-15.136 076 523	-5.208 426 855
dl5AT1E0	dl6AT3G0	2006-02-13	+15.136 008 268	+5.208 077 517
dl5AT1E0	dl6AT3G0	2006-02-25	+15.135 732 062	+5.208 344 855
dl5AT2E0	dl6AT3G0	2006-03-16	+15.136 008 268	+5.208 077 517
dl5AT2E0	dl6AT3G0	2006-03-17	+15.135 925 588	+5.208 181 358
dl5AT1E0	dl6AT3G0	2006-08-27	+15.135 968 430	+5.208 315 141

Table 3: Apparent length variations in the E0–G0 baseline length through the variation in DL and AT number, obtained from the `IPHASE` fits collected in the `vltipom` CMM module.

These variations are artificial to some degree; they were obtained by ESO running `IPHASE` with star catalogues with zero proper motions and radial velocities. Fig. 26 shows a test where this information (from `SIMBAD`) has been added explicitly to the `IPHASE` input file for all 17 sky positions. It proposes that incorporating these, especially for stars like `lam Sgr` and `tau Sgr` with large proper motions, can reduce the `IPHASE` fitting errors. The origin of the residual misfits on the ± 200 μm scale—equivalent to a timing jitter on the 100 ms scale if one translates them with the velocities as in Fig. 45—is not clear.

11.4 Detailed contributions

11.4.1 M11/FSM Image Jitter

Since the guidance of the off-axis beams over M1 to M10 includes various turns, one might be tempted to define the endpoint of the baseline as the image M11' of M11 as seen from above M1 (Fig. 23). This would "keep" the differential angle on the sky up to the baseline endpoints.

A result of this attachement of the baseline to the M11 images is, that if any of the optics between the entrance pupil and the reference surface are moved then the baseline may be changed. If, for example, M2 is moved one μm off axis, the baseline changes by a few tens of μm, generating an error term which contributes significantly to the overall error budget, since this change is not sensed by

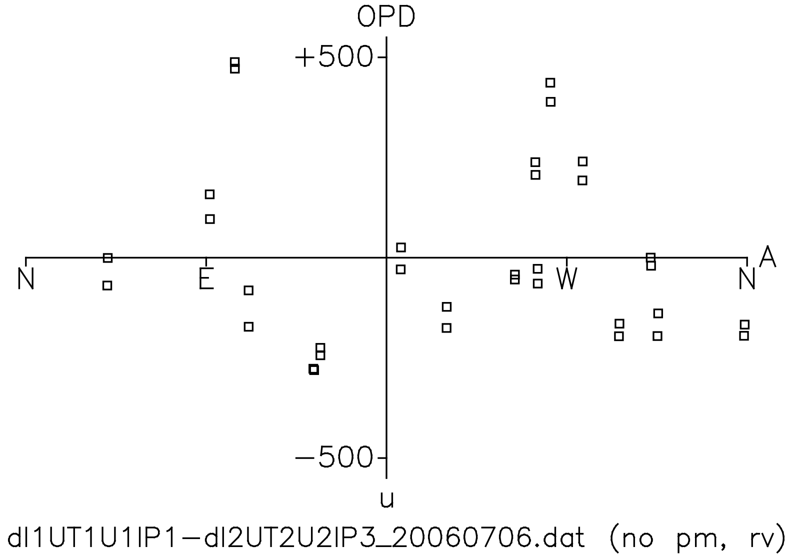

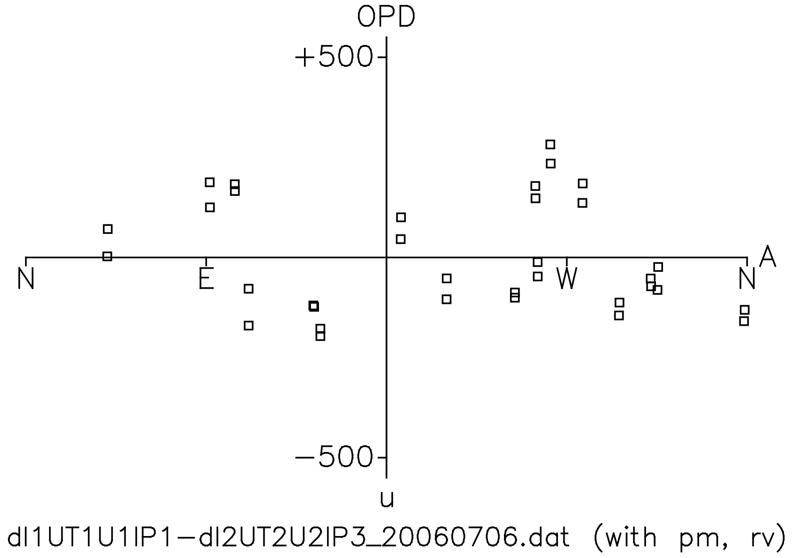

Figure 26: Comparison of running `iphase` over UT1–UT2 MIDI data with or without providing the input information on proper motion, parallax and radial velocity. The rms error in the OPD with the four standard parameters `T1X`, `T1Y`, `T1Z` and `A1L` is reduced from 215 μm in the upper plot to 136 μm in the lower.

an equivalent change in the metrology light path. If we start from a reference image of M11 under the assumption that all mirror surfaces are at their nominal positions—which is the on-axis case of Table 11), the sensitivity of these image coordinates to individual, uncorrected translations of AT mirrors follows according to Table 4.

By symmetry, the plane mirrors (M3, M4, M6, M9) and to good precision the almost plane mirror M8 can be translated sideways in two directions perpendicular to their surface without changing the light path: In the global coordinate system chosen in Table 4, this shows up in zero responses for the y-direction, whereas the second direction in the $x-z$-plane depends on the individual mirror's

mirror transl.	x (μm)	y (μm)	z (m)
none	0.000000	0.000000	-15.438
M1 x	-0.055	0.000	-15.438359
M1 y	0.000	-0.054	-15.438456
M1 z	0.000	0.000	-15.438004
M2 x	-0.062	0.000	-15.438456
M2 y	0.000	-0.062	-15.438456
M2 z	0.000	0.000	-15.440469
M3 x	0.127	0.000	-15.436884
M3 y	0.000	0.000	-15.438456
M3 z	0.127	0.000	-15.436884
M4 x	-0.127	0.000	-15.440023
M4 y	0.000	0.000	-15.438456
M4 z	-0.131	0.000	-15.439978
M5 x	0.790	0.000	-15.435334
M5 y	0.000	0.790	-15.438360
M5 z	-0.054	0.000	-15.392514
M6 x	-0.118	0.000	-15.467721
M6 y	0.000	0.000	-15.438456
M6 z	-0.324	0.000	-15.518691
M7 x	-1.173	0.000	-15.352677
M7 y	0.000	-1.520	-15.438410
M7 z	0.988	0.000	-15.354522
M8 x	-0.245	0.000	-15.488396
M8 y	0.000	0.000	-15.438456
M8 z	-0.606	0.000	-15.562258

Table 4: M11 center point images in a coordinate system centered at M3 where $+z$ is parallel to $+W$, and $+x$ is parallel to $+V$ (Fig. 27), ensueing from AT mirror x, y or z coordinates translations of 10 μm. The 10 μm have been adopted from an axis runout specification [54] and because this number has been dropped in [39].

inclination toward the horizontal. A table with the image response for perturbations of the remaining three degrees of freedom of the AT mirrors, their rotations, can be set up in the same fashion.

The cause of this high sensitivity to mirror perturbations is that most of this is powered optics, and this demonstrates why the baseline definition via the M11 *images* is not advantageous compared to the definition of the M11 themselves: whereas the optical path from M3 to M11 is about 13 m (Tab. 10), the mirror image is 16 to 38 m below M3 (Tab. 11), since some of the path is stretched/shrinked by longitudinal magnification factors. The closer lineup of the dashed wavefronts in Fig. 23 symbolizes that this implies a piece-meal re-definition of the wave number/wavelength as a function of the magnification of the local path element, which is needed to end up with the same number of phase turns in the straight, mirrored path and the zig-zagged actual path. The scale of the ruler, which measures the OPL up to the baseline terminal point, must change along the way from M1 to M10 to convert the mirrored M11 to a point in space that is helpful in the sense of the second sentence on p. 61. [Note that this problem cancels for the wide angle definition via M3 as long as this stays at the center of the telescope axes crossing.]

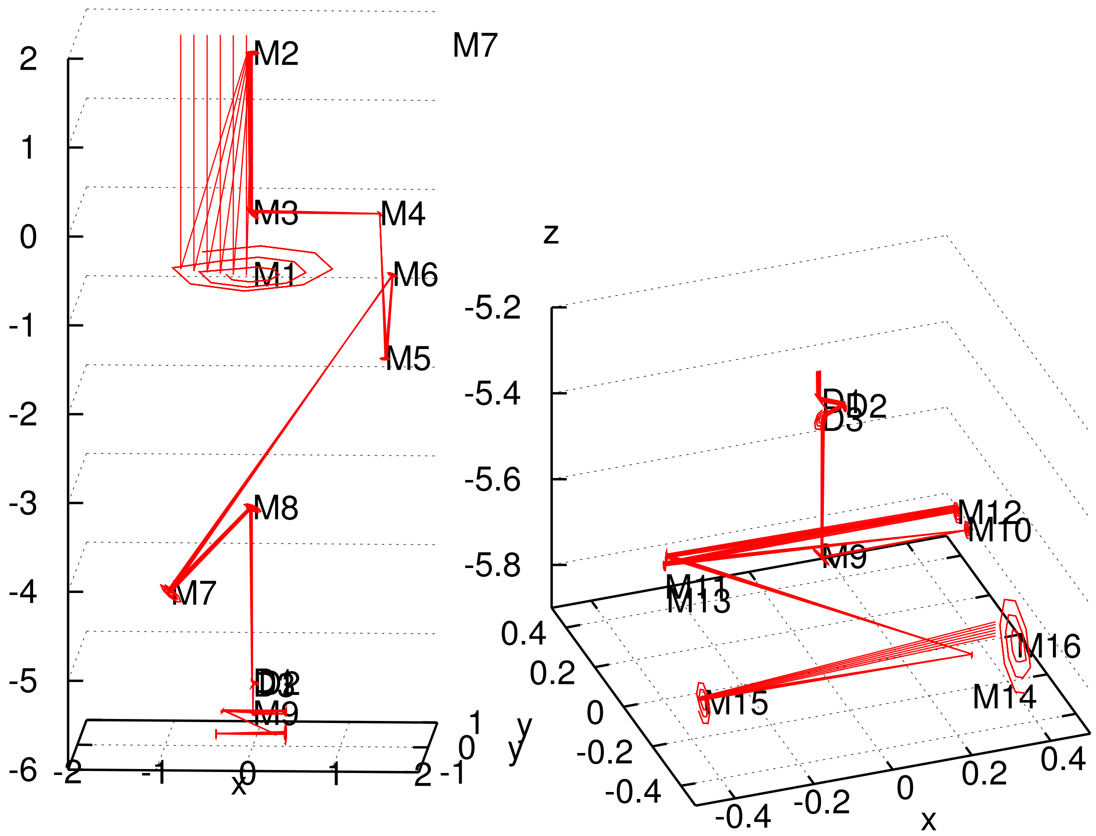

Figure 27: Optical layout of the AT Coudé train and one arm of the dual beams of the star separator, with the coordinate system used in Tables 4 and 11. Up to M8, the system is similar to the UT train [48].

11.4.2 OPL Leakage

The disadvantage of fulfillment of the "requirement" of the baseline terminal point rather late in the mirror train is: Ordinarily, the total OPL from the star through one of the telescopes up to the beam combiner would be split in two sections, one up to the entrance pupil and the other one "linearly" controlled by a delay line. This allows "geometric" reconstruction of the PW tilt angle above the telescopes from finding the fringe position. This is also the naïve splitting of the optical path difference in exactly two parts we find in the Glossary of [31]. With PRIMA, a middle section between the entrance pupil is inserted which adds OPL for off-axis rays until the baseline is reached. We may refer to this term, which has been placed at the end of the SS path in Fig. 25, as "OPL leackage" because it changes the optical path length without changing the IR metrology reading and without originating from an angle on the sky. As argued in Fig. 25, the symmetry of the two telescopes allows to regard this as an "uncontrolled" section of the delay lines, because the OPD is not affected. Implications to the astrometric data reduction follow in Sec. 12. As long as the two telescopes are identical, connecting any point on an optical surface of one telescope to the same point on the other defines the same three components of the baseline vector, and the result of calculations like the one in Sec. 32.2 is immune against the actual choice.

The strategy to handle asymmetries between the telescopes could be

- to define the narrow-angle baseline terminal points at the (real) M11, not their images, with the advantages
    1. Baselines are more stable because the defining optics is not exposed to the wind; all image jitters discussed above are irrelevant.
    2. Baselines are closely monitored by the "internal" metrology.
- to perform an OPL (not a baseline) calibration as a function of off-axis angles (defined according to the varying angular magnification either in the lab coordinates after M11 or on the sky)
- to subtract this delta in the OPL from the total OPL that has been measured by the science beam (but not by the metrology) to account for any add-on path (differential leakage) shown below M2 in Fig. 23.
- to discuss the contribution of errors in mirror positions and angles not in terms of the baseline b or optical path difference D, but directly in terms of angles z (with the benefit of cancellation effects between errors in D and b on one hand, and between PS and SS on the other).

11.4.3 Axis Runouts

The stability of the vertical axis of AT#1 has been measured in [134]. The wobbling of the axis of $\approx 21''$ shows the need of counter-steering with the other axis, and is not of immediate interest.

The measured radial runout of 11 μm is small enough that the definition of the baseline length to 40 μm (see Sect. 28.3.3) is not in danger, and does not need an azimuth term. The estimated accuracy of the relative positions of the bearing center and the ROS rotation center to the "station" of ≈ 60 μm center indicate that a new "baseline solution" is needed for each transportation between the AT stations. The azimuth axis of AT#3 has a similar displacement of ≈ 80 μm found with one fixed clamping to a "station" [144], with the same conclusion.

The distance between the Altitude and Azimuth axes of AT#1 is ≈ 50 μm, with a measurement accuracy of ≈ 40 μm [135, §4]. This obviously adds a "dipole" term of the same amplitude to the baseline terminal point as a function of azimuthal pointing direction. This is either reduced or enlarged by the equivalent effect on the independent sister telescope, which depends on whether the "gap" has the same sign on both. (A "sign flip" during the integration phase of the telescope is reported in [135].) The same magnitude of a ≈ 50 μm gap was measured for AT#3 [142]. Since both measurements are sufficiently close to the term allocated in the baseline error budget, and the pointing to a common target means their azimuth dependence has a common "dipole" characteristics, the calibration of the effect ought be feasable.

12 SYSTEMATIC DIFFERENCES IN BASELINE LENGTH FOR PS AND SS

12.1 Introduction

Differences in the colour or the elevation of the PS and SS could in principle introduce a difference in the effective baseline length for the interferometric measurements.

Systematic deviations between the OPDs from the (achromatic) effect of handling the two principal rays of the PS and the SS at the same time (sharing the same mirror surfaces up to M9) are investigated below [12].

12.2 Dependencies

12.2.1 This error term is effected by

Error term	Relevant subsection
Ground level temperature, humidity and pressure fluctuations	E.3.2
Wavefront amplitude and phase fluctuations above M1	5.3

12.3 Detailed contributions

12.3.1 Off-axis optical path lengths

The magnitude of the effect described in Section 11.4 for the nominal mirror surfaces is calculated as sketched in Fig. 28: the actual path length difference the rays have to run from O and R to the center of M11, respectively, is subtracted from the path difference they would have if they ran from O and R straight to X, respectively. (As shown in Table 11, this point X is 16 to 38 m below M3. In some sense, it plays the role of an ideal 1-mirror substitute of the Coudé train, and can be defined for any direction of the dual beams on the sky.)

This OPD leakage, which is a detour actually travelled by off-axis rays and which could be wrongly attributed to the star separation angle τ, is plotted in Fig. 29. Note that this is derived from intersection of the on-axis with the off-axis ray; there is no proof that the numbers are associative in the sense that the leakage experienced by combination of any two off-axis rays is the sum (or difference) of two of these individual numbers, because their point of intersection X would generally be off-axis, too, and not be related in simple terms to any of the individual on-axis intersections X. There is one lucky, obvious expection to this: if the two stars are symmetrically placed relative to the STS (and telescope axis), the additional OPD's are the same for both stars and lead to no net effect to the fringe placement as it would be noticed by the FSU.

12.3.2 Impact on Astrometry

Looking at Fig. 25, taking into consideration both telescopes, cancellation happens more generally to the degree that both telescopes are replicas that act in the same way: the computed OPD's remain uneffected, and so does the differential OPD. The OPL leakage in each single telescope does not add a systematic spurious term to the OPD.

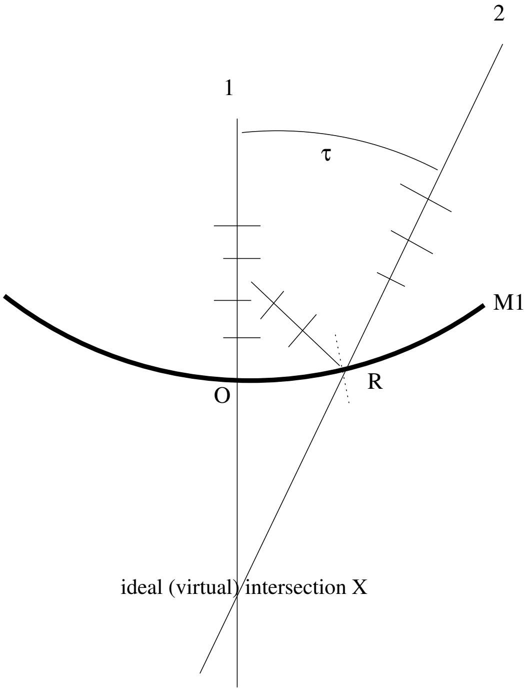

Figure 28: The reference on-axis ray 1 and the off-axis ray 2 are relayed at the surface of M1 and their optical path lengths up to the point when they meet M11 are different from the ones they would have reached meeting at X. This is the pupil plane analog to a residual astigmatism of the mirror train from M1 to M11/FSM.

Then, tracking errors [91, Fig. 11] become the source of residuals.

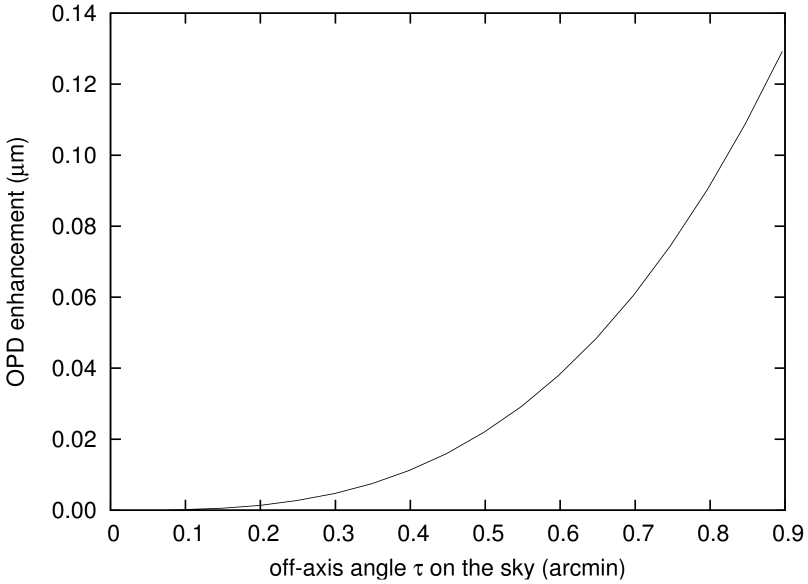

Figure 29: The OPD "leakage" of Fig. 28 subtracting the two actual and the two virtual path differences $(\overline{R \rightarrow M11} - \overline{O \rightarrow M11}) - (\overline{R \rightarrow X} - \overline{O \rightarrow X})$. The two actual path differences measured from R and O to M11, and the virtual path differences measured from R and O to X: see Fig. 28. The actual aberration and astigmatism of AT1 [91, Fig. 12–13] are of the same order of magnitude.

13 QUASI-STATIC COUDE TRAIN MIRROR MOTIONS

13.1 Introduction

Deviation of AT mirrors from their nominal positions change the OPL to the BC. If the same deviation applies to both telescopes at the same time—which is a lowest-order description of mirror cage deformation due to larger zenith angles or temperature gradients in the dome—the two OPDs and the differential OPD remain unaffected.

We study the effect of unpaired mirror motions, defined as those that are not matched by the sister telescope, caused by inherent differences in the constructions, by uncorrelated vibrations on short time scales etc.

The contents of this section is summarized in [116].

13.2 Dependencies

13.2.1 Error terms effected by this

Error term	Relevant subsection
Fringe jumps and group tracking errors	27.4
Wavefront corrugations before and after the STS	6.3

13.3 Detailed contributions

For the telescope mirrors, the impact on the baseline definition is demonstrated in Section 11.4. We follow the proposal of Section 11.4.2 and convert unbalanced mirror motions not into errors of the baseline but into errors of the differential OPD ΔD.

13.4 Impact on astrometry

The model calculations of the effect optain optical path lengths of PS and SS rays that start at different U coordinates but the same V coordinates above M1, at a star separation τ, head towards the apex of M1, and end at a (virtual) flat mirror after M11/FSM and before M12. Four OPLs are obtained by performing this calculation twice, once for the nominal mirror positions, and once for mirror positions perturbed by translation or rotation, the six degrees of freedom of a rigid mirror.

13.4.1 Case Study A: With M11/FSM Tip/Tilt Removal, Requirements

The sensitivity of the OPL to mirror translations and rotations depends on the off-axis angle, the telescope pointing direction, and the mirror in question (position, orientation, conic constants). We present the *requirements* on the maximum deviation of each of the mirrors. For the following calculations, we assume active control by IRIS [138] on M11/FSM of the STS up to 10 Hz [138][15, §2.3]: generic distortions of the mirror positions end up in changes in both OPL and in image position on M10. Our calculations re-orient each M11/FSM to project the center ray of its tilted beam perpendicular onto the common vertical reference placed at M12, where the “nominal” OPL and the “distorted” OPL are subtracted to define the tabulated “effect.” (A rewording of this is that the small-angle baseline is only defined after the compound action of all mirrors up to M11/FSM.) This treatment of M11/FSM as active mirrors leads to much less DOPD sensitivity to mirror distortions than keeping them at their nominal position for the nominal off-axis star positions.

Corrective counter-steering of M6 as a result of tilting M1–M5 is not taken into account: One of the mirrors is rotated off its nominal position at a time.

Details of Calculations For each pointing of the main telescope axis, 29 points above the M1 surface are rather randomly selected by tessellation of the entrance pupil of 1.8 m diameter. For each of these, 4 rays are traced reflecting individually at each conic surface until they end at a virtual flat screen fixed near M12 of the STS. (This is done within the focus of M12, not in a pupil plane. This does not harm because the DOPDs are calculated for each ray individually, then averaged.) This yields 29 times four OPLs between the starting point and a vertical flat mirror replacing M12:

- l_{Pu} for the PS and unperturbed (nominal) mirror optics
- l_{Su} for the SS and unperturbed (nominal) mirror optics
- l_{Pp} for the PS and perturbed mirror optics
- l_{Sp} for the SS and perturbed mirror optics

Figure 30 visualizes this process. This produces 29 differential OPDs $l_{Pu} - l_{Pp} - l_{Su} + l_{Sp}$; the radial dependence (created by following the beams not to a pupil plane) of the individual ray positions cancels when this difference is calculated, and dependence on the arbitrary zeros of the OPL is also removed. The DOPD differ by a few percent depending on starting point above the telescope: the induced OPD error has speckles across the pupil, and a weighted average of these samples is taken.

The calculations assume that the rotation axes of the distortions run straight through the apexes on the mirror front surfaces; sweeping motions (superpositions of translations and tilts) of mirrors in realistic mounts have not been simulated.

Back-of-the-envelope Estimates The sensitivity to M7 rotations shown in Table 5 could as well be estimated as follows with Figure 31: the footprint of the $2'$ FOV on M7 is 111 mm as shown in Figure 7 of [39]. If the off-axis angle is $\tau/2 = 30''$, the mirror is hit $x \approx 28$ mm off-center by the middle of the beam. The radius of curvature of M7 is 3826 mm, so these 28 mm are equivalent to a distance of $y \approx 100$ μm from the tangential plane of the apex, or 0.0036 rad of tilt. Adding the distortion of $0.0087''$ lifts this distance by ≈ 1.1 nm where shown by the double-headed arrow. There is a factor of 2 for the conversion of mechanical to optical path length, and another factor of 2 for the opposite modification of the other star's beam on the opposite hemisphere of M7, building the total of 5 nm.

The mixing ratio for the sensitivity towards rotations around the V and W axis derives from the angle of each particular mirror towards the horizontal.

The action of M7 translations follows in the same manner, Figure 32: the derivative of the off-center point on the conic with respect to side-ways shifts equals twice the tangent of the aforementioned 0.0036 rad of tilt. (The factor 2 is the familiar factor of the derivative of a parabola.) Multiplication with the sideways motion of 0.13 μm of the table yields 1 nm, and the two factors of 2 apply as for the tilts.

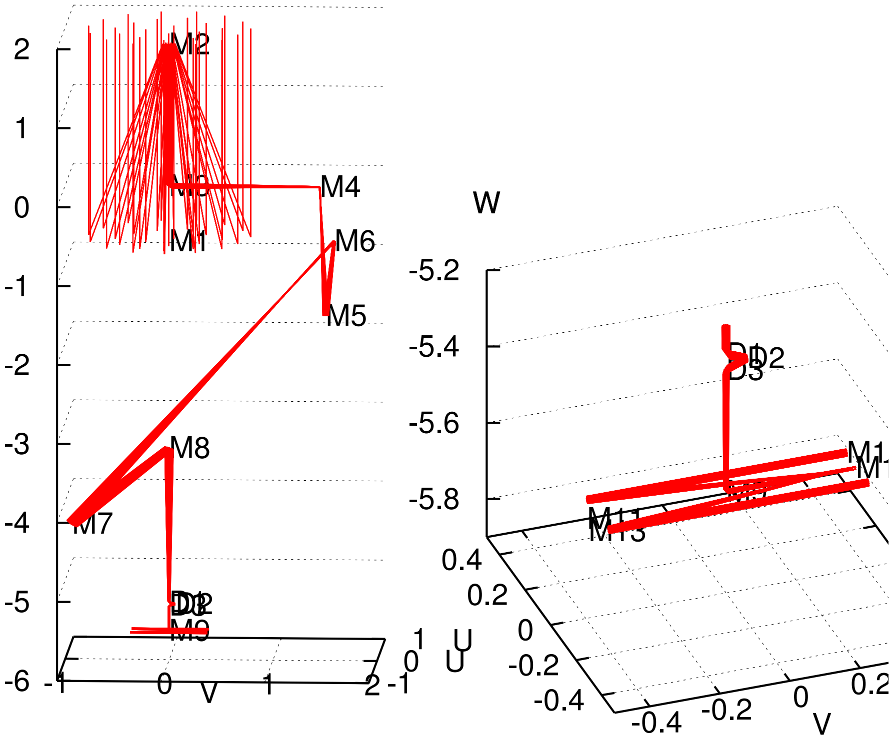

Figure 30: A bundle of 29 rays is sent four times through the AT mirror train to build a statistics over the differential OPD. D1–D3 are the mirrors of the star rotator. Turning the three mirrors of the star rotator by an angle φ around the W axis rotates the image by 2φ.

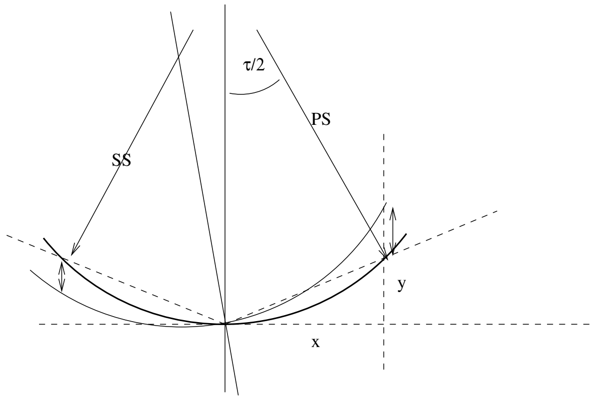

Figure 31: If the centers of the footprint are x away from the mirror axis, a slight tilt of the mirror axis away from its nominal position changes the optical path lengths in two different directions, away from the nominal value y.

In summary, the lever of the center of the off-axis footprints on the mirrors establishes the DOPD sensitivity to two out of three axes of rotation. If the footprints of the off-axis beams are read from [39], ray-tracing is superfluous to perform the sensitivity analysis. One may attempt to perform a

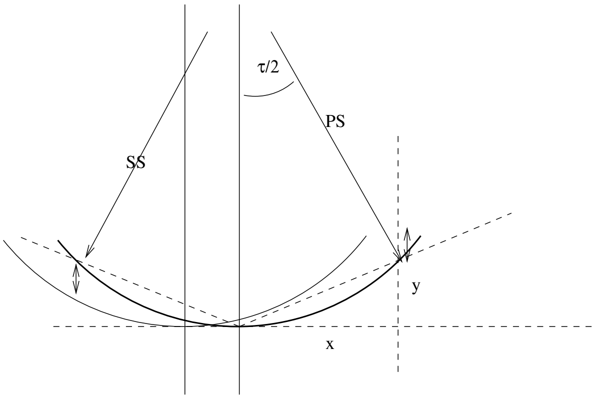

Figure 32: If the centers of the footprint are x away from the mirror axis, a slight translation of the mirror axis away from its nominal position changes the optical path lengths in two different directions, away from the nominal value y.

Gaussian (linear) analysis of the imaging errors for these perturbations [30, 175], but these calculations become quickly complicated even for a 2-mirror optical system with one plane of incidence; no further insight would be gained.

Results for Zenith Pointing Results of this sensitivity analysis are shown in Table 5 for zenith pointing of the main telescope axis. It shows the translations along the UVW Paranal coordinates in units of μm or the rotations along these coordinate axes in units of arcseconds that produce a differential OPD of 5 nm (unless matched by the same distortion on the other telescope).

The star separation of $\tau = 20''$ or $\tau = 60''$ (the latter is half of the maximum accomodated by the FOV) is split either symmetrically w.r.t. the mirror axis into $\tau = 10'' + 10''$ or $\tau = 30'' + 30''$ off-axis angles, or asymmetrically into $20'' + 40''$. Three dots mean the DOPD is insensitive to the degree of freedom at a table entry:

- indicating the translation must be $> 500\mu$m to induce 5 nm in differential OPD.
- the rotation must be so large that either some of the 29 pencils would be clipped (not reach M12), or so large that the difference in the DOPD across the speckles is much larger than the 5 nm; then computing the average over the 29 traces does not make sense.

The reasons for this insensitivity are either

- symmetry of the optical setup: examples are sideways translations of plane mirrors in the two directions perpendicular to their surface or rotations of non-elliptical mirrors (all but M8) around their principal optical axis. If τ is split evenly into off-axis angles of 30 arcsec between the two stars, the inherent symmetry of the mirror train w.r.t. flipping the U coordinate is preserved, and some of the perturbations applied do not take effect on the differential OPD ΔD. Sideways motion of the flat mirrors does not even change the OPLs and is the least harmful degree of freedom in this study, always ending as 0.0 in the table.
- or a distortion inducing a mere tip-tilt component which can be “counter-chopped” by individual action of the two M11/FSM.

It is assumed that the star rotator is rotated such that the line between the stars runs perpendicular across the STS edge. Numbers in parenthesis mean that this rotation angle on the sky is not 90° but off by 1°, which increases the sensitivity to the corresponding translations. This value of 1° IRIS error in the star rotator angle is equivalent to $30'' \cdot \sin 1^\circ \approx 0.5''$ on the sky for the star separation of $1'$, close to the $1.2\lambda/d \approx 0.31''$ of the PSF.

mirror	translation			rotation		
axis	$30''+30''$	$10''+10''$	$20''+40''$	$30''+30''$	$10''+10''$	$20''+40''$
M1 V	…	…	-44.	-0.0085	-0.026	-0.0084
M1 U	0.22	0.70	0.22	49.	…	…
M1 W	…	…	-98.	…	…	…
M2 V	…	…	46.	0.096	0.30	0.093
M2 U	-0.21	-0.65	-0.21	…	…	…
M2 W	…	…	78.	…	…	…
M3 V	…	…	…	-0.11	-0.34	-0.12
M3 U	…	…	…	…	…	…
M3 W	…	…	…	0.11	0.34	0.11
M4 V	…	…	…	0.08	0.26	0.086
M4 U	…	…	…	…	…	…
M4 W	…	…	…	-0.088	-0.26	-0.088
M5 V	…	…	280.	-0.034	-0.099	-0.034
M5 U	0.26	0.77	0.26	…	…	…
M5 W	…	…	67.	1.3	3.8	1.3
M6 V	…	…	180.	-0.59	-1.9	-0.59
M6 U	…	…	…	…	…	…
M6 W	…	…	64.	1.6	5.1	1.6
M7 V	… (8.4)	…	75.	0.0087	0.026	0.0087
M7 U	-0.13	-0.38	-0.13	…	…	…
M7 W	… (-9.9)	…	44.	-0.011	-0.032	-0.011
M8 V	…	…	-81.	-0.013	-0.038	-0.013
M8 U	…	…	…	…	…	…
M8 W	…	…	-32.	0.032	0.096	0.032

Table 5: Effect of single-mirror motions (i.e., their allowances) that change the DOPD by 5 nm, the case of zenith pointing. The left three columns describe mirror translations (μm) in one of the three directions, the right three columns describe mirror rotations around the axis (arcseconds in the local frame, not on the sky). Note that tip-tilt corrections by M6 are not taken into account.

The DOPD is generally *not* immune against rotations of the M6 tip-tilt mirror, although this is in a pupil-plane and both beams hit centered. The reason is that the resultant change in the pointing direction accumulates OPLs up to M11/FSM differently for different off-axis angles: the OPLs up to there have an approximately quadratic dependence on the off-axis angle (assuming no other power optics in between). If L is the path length along the main optical axis between two mirrors, stars at a small angle θ have a path length $L/\cos\theta \approx L + L\theta^2/2$. This changes by $L\theta \cdot \Delta\theta$ if θ changes by $\Delta\theta$. Example: The FSM is $L = 9$ m away from M6 (Table 10). If $\theta = 30'' = 1.5 \cdot 10^{-4}$ rad, a change by $\Delta\theta = 1'' = 4.8 \cdot 10^{-6}$ rad is a change in OPD of 6 nm. The effect on DOPD is twice as large for a symmetric splitting of $\tau = 1'$ because the other beam is changed as well with the same θ, but opposite $\Delta\theta$. The equivalent calculation can be applied to M1, but the angular magnification becomes an additional factor.

Results for Random Pointing In the case of "random" pointing to general altitude and azimuth positions, the footprint of the center line between the two stars on the individual mirrors classifies which linear combination of U, V and W coordinates in translation or rotation becomes the "critical" or "insensitive" component—think of this as a principal axis decomposition. "Random" pointing means that general conclusions should be aware of artificial cancellation effects that arise if the telescope points to special directions associated with principal axes of the mirror train (zenith, along a V coordinate,...). Here, this re-mixes the three axes for new principal axes, but does not change the magnitude of the effects. In plain English: for other directions than the zenith, the typical 0.2 μm are re-distributed over the U, V and W axes without changing the combined magnitude.

Conic Constants Asymmetry in the conic constants between the two telescopes introduces concentric phase distortions across the pupil—overlaid with those that are already intrinsic to the nominal design [39]. These alternate in sign as a function of distance from the pupil center, and therefore tend to cancel to high extent if sent through the spatial filter of the FSU. We therefore do not form the mean across the pupil as with the translations and tilts above, but report the change in the (unitless) conic constant that is allowable if the *maximum* effect on the DOPD is to be kept below 5 nm: Table 6. The actual variation for the UT mirrors is reported in [190, Table 4-1].

mirror	$30'' + 30''$	$10'' + 10''$
M1	0.00020	0.00031
M2	0.00063	0.0015

Table 6: Effect of change in the conic constants of the primary and secondary (i.e., their allowances) that change the DOPD by 5 nm across the pupil, the case of zenith pointing. In two examples of the star separation, $1'$ and $20''$, the STS splits the separation evenly by half.

13.4.2 Case Study B: Active M6 plus M11/FSM Tip/Tilt Removal

Considering the angular magnification factor ≈ 60 near M6, the ratio $-1.9/-0.026 \approx 73$ for the relative effects of a M6 and a M1 rotation along V in Table 5 indicate that this action of M6 (upon notice of the equivalent motion of the GS) would provide very efficient correction to this error in ΔD.

Therefore additional calculations have been run where distortions of M1–M5 trigger a tip/tilt rotation of M6 such that an on-axis ray (which is generally no longer on the true optical axis at arrival at M6 due to these distortions) is brought back to a path parallel to the nominal axis between M6 and M7. It is to be noted that

- the future of active control of M6 besides the active control via the M11/FSM is dependent on ESO decisions, which warrants a separate study in addition to the one of Section 13.4.1.
- the actual control loop is more complicated because the image position is monitored after M9; this allows in addition counter-steering of distortions acting on M7 and M8, which has not been implemented in our ray-tracing software.

The sensitivity of this model calculations is summarized in Table 7. Compared to the case without active M6, there is no noticeable change: M6 simply cannot remove piston which is the main scope of the present analysis. The question whether the axial focussing with M2 to adapt to changes in the distance between M1 and M2 ought also be studied does hardly arise, because this would allow some correction to the M1 and M2 W translations of the table, not to the decentring translations shown in V or U direction which are obviously more important.

mirror	translation			rotation		
axis	$30'' + 30''$	$10'' + 10''$	$20'' + 40''$	$30'' + 30''$	$10'' + 10''$	$20'' + 40''$
M1 V	...	...	-45.	-0.0079	-0.021	-0.0079
M1 U	0.21	0.55	0.21	25.	29.	-1.7
M1 W	...	...	-50.	...	...	...
M2 V	...	...	47.	0.090	0.24	0.090
M2 U	-0.20	-0.52	-0.20	...	...	-21.
M2 W	...	...	50.	...	...	...
M3 V	...	...	...	-0.11	-0.34	-0.11
M3 U	...	...	...	...	...	-31.
M3 W	...	...	...	0.11	0.34	0.11
M4 V	...	...	...	0.08	0.26	0.086
M4 U	...	...	...	...	...	79.
M4 W	...	...	...	-0.088	-0.26	-0.088
M5 V	...	...	...	-0.034	-0.099	-0.034
M5 U	0.26	0.79	0.26	...	...	53.
M5 W	...	...	100.	1.3	3.9	1.3

Table 7: Single-mirror motions in units of μm and arc-seconds that change the DOPD by 5 nm as in Table 5. The difference is that some tip-tilt correction by M6 is added as explained in the text, with has virtually no effect.

13.5 Estimated Performances

13.5.1 Non-Astrometric

Tests reports [85, 86, 87, 88] on AT1 and AT2 have measured pointing, chopping and other performances which have no relevance to the OPLs discussed here. (Table 1 in [54] implies that only requirements on the WFE, but no requirements w.r.t. the OPL exist.)

The only obvious actual misalignment is the periodic activity of the M6 as documented in Section 22.4. The *measured* astigmatism of 200 nm as a function of pointing direction, Figure 13 in [91], encompasses these effects for a single, on-axis beam. The main task of this section is to estimate to which extent this magnitude persists after subtraction to a differential effect looking through two telescopes, and to compare the residual with the 5 nm “guideline” of the (total) error budget.

13.5.2 Frequency Cut

A cut on the frequency axis divides frequency components that are subject to averaging after a sufficient time of observation (Section 22.2) and mainly prolong this time for a fixed accuracy, and others on a time scale of half an hour and longer which we focus on now because their signature could be misinterpreted as a "trend" of astronomical origin if the same target pair is not visited again.

The frequency spectrum in the "breathing" mode that changes the M1–M2 distance is provided in [140]. A look into Table 7, rows M1 W and M2 W, shows that an asymmetric distance of the stars to the STS edge may induce a DOPD in this case, but would be allowed up to typically 50 μm for a star separation of $1'$. Since the measured OPDs does not exceed OPD changes of ≈ 5 μm on time scales of 30 seconds, the DOPD generated from this effect would well comply with the error budget: a M1–M2 longitudinal motion of 5 μm along the common telescop axis is still "common" mode.

13.5.3 Finite Element Calculations

The FEM analysis [5] will not be analyzed in what follows for the following reasons: (i) only pages 30–39 have been made available to the Consortium. (ii) The "stresses" applied to the telescope structure that cause distortions (temperature, gravity, even wind) are to lowest order identical for both telescopes, and one would have to introduce assumptions like on the difference in vertical temperature gradients between the two telescope stations (ie, on the second partial derivative off the temperature w.r.t. the spatial coordinate) to generate the length differences to advance to estimates of the ΔD signature. The local temperature gradients studied in the analysis, for example, would typically be caused by some power generated by electronics and motors, but it is plausible that the same type of equipment would heat the equivalent spots on the sister telescope as well. The wind loads are also the same to lowest order, because both telescopes are looking into the same direction with the same arrangement of their wind shields and the same M1 cross section facing the wind; the reasoning for differences then have to be based on assumptions on dominant wind directions and some AT stations being a bit better protected by the UT domes and the VLTI control building than those on the J rail. These are fine examples of the problem outlined in the third chapter on page 3. (iii) It seems to be easier (and simply more reliable, see e.g. the underestimation of the deflection by a factor 10 in [141, Fig 5-2]) to proceed to parameters actually measured.

It looks as if the work done by the manufacturer followed closely the expected verfication procedures on the real hardware. However, some FEM results provide estimates on the response of the structure to wind, and estimates on motions of M4–M7, which are not complimented by the test reports on real hardware.

From the available information we conclude:

- The thermal expansion of the tubes is expected to increase the distance between M1 and M2 by approximately 1.6 μm for a temperature difference of 0.2°C [5, 6.1.2.3.4]; given prototypical vertical temperature laps rates of Fig. 33 there is no risk to reach the tens of microns of Table 5 needed to impact the ΔD. Looking at the vertical distance between M4 and M7 of 4.3 m (Figs. 30,27), an effect of 9 μm of Table 5 is also unlikely—even considering that M7 may feel some of the several degrees of temperature difference between tunnel and outdoors displayed in Fig. 46 of [119]. Given that already two ATs are on the moutain with their local temperature sensors [11], real data to verify this assumption ought already be available.
- The gravity load at 30° pointing from the the zenith displaces the "components" of M1 by up to 77 μm, of M2 by up to 180 μm, and of M3 by up to 45 μm. Again, these non-differential numbers have no immediate relevance to the astrometric DOPD.
- The effect of wind load on M7 was estimated to be smaller than $3.1 \cdot 10^{-7}$ rad ($= 0.07''$) for the angular distortion and smaller than 0.28 μm for the displacements perpendicular to the

direction of incidence [5, p. 36]. This exceeds the allowances, Table 5, by about a factor of 7 for the tilt and about a factor of 2 for the displacement at a star separation of $1'$, and again to a lesser degree at smaller star separations.

The effect of wind load on M1 was estimated to be smaller than $5.6 \cdot 10^{-7}$ rad ($= 0.11''$) for the angular distortion and smaller than 1.9 μm for the displacements perpendicular to the direction of incidence [5, p. 34]. This exceeds the allowances, Table 5, by about a factor of 14 for the tilt and about a factor of 9 for the displacement at a star separation of $1'$, to a lesser degree at smaller star separations.

We stress that the expected *differential* effect is an unknown portion of these.

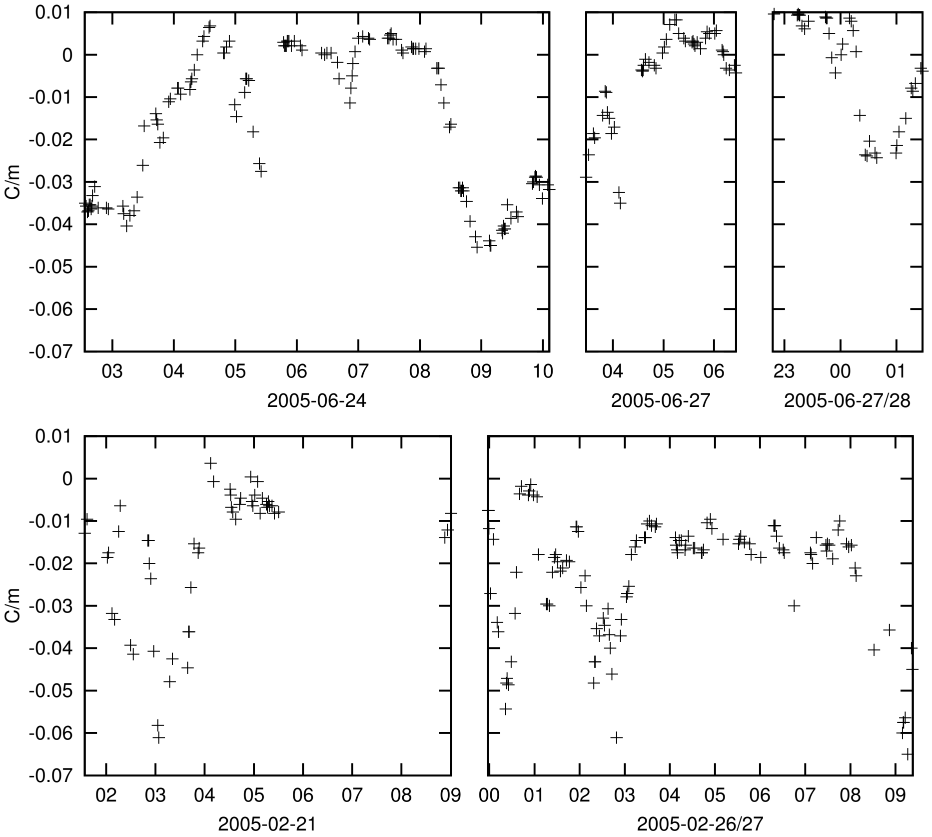

Figure 33: Randomly selected examples of ambient laps rates on the Paranal platform in units of °C/m reported by MIDI FITS files with the `ISS AMBI LRATE` keyword. The spacing between the abscissa tic marks is one hour.

The subsequent approach to generate any differential statistics in the PRIMA sense is to compare characteristics of any two of the three "prototypical" telescopes that have actually entered Paranal. If no equivalent tests of this "replica" type are available, one may look at "hysteresis" numbers within a single telescope.

13.5.4 Report on AT#3 Structural Deflection

Measurements on AT#3 [141] tabulated the translations and rotations of M1 to M3 as a function of deviation off the zenith. The items of interest are

- [141, Tab. 5-1] shows that that the deflection of the M1–M2 axis around what would be the two horizontal axes for zenith pointing has a standard deviation (hysteresis) of up to 12 μrad (=2.4″). This exceeds the allowance for the "rotation" column of the M1 V axis in Table 5 by a factor 100 assuming that the typical star separation will be $\approx 20''$. One of the two axes is stiffer by a factor of two resulting from the uniaxial cross-bar of the altitude axis, potentially reducing the factor to 50 depending on the alignment with the STS edge.

  The astrometric assessment of this optical measurement depends on how much of this is attributed to pointing of M1 and/or pointing of M2, because the sensitivity of the DOPD to M1 is roughly ten times higher as the sensitivity to M2 (Table 7). (We are confident that any effect of an optional non-flat surface of the dummy M2—which we have no information about—has been properly reduced during the AMOS data analysis.) For this aim one would like to move on to the tilt sensor measurements (with the intrinsic disadvantage that they measure M1 motion relative to the tube structure), but finds that the values in [141, Tab 5-3] do not have a statistical information on the scattering of the data over the sets of the measurement which we are looking for. To this end we conclude from the fact that the full angular motion of M1 in [141, Tab 5-3] is less than 17 μrad and less than 15 μrad for one axis and less than 1.5 μrad for the other in [141, App. 7], of which at least 2/3 are predicted by the FEM, that most of the relative deflection between M1 and M2 stems from M2. Since the measurements of [141, p 32] with some modified mirror support repeated the values of [141, p 14] to within 3 μrad for the more flexible axis and brought the motion stiffer axis to 1.7 μrad, we assume that the differential M1 tilt will be bound by 3 μrad ($= 0.6''$), and the differential M2 tilt to 9 μrad ($= 2''$).

- [141, Tab. 5-2] shows that the translational mismatch between M1 and M2 is reproducible to 2 μm or better, close to the intrinsic accuracy of the test equipment. In comparison with the "translation" columns of Table 5 or 7 the allowance would be exceeded by factors of ≈ 3–6.

- [141, Fig. 5-6] shows a hysteresis of the M3 pointing of $\approx 10\mu$rad for zenith angles $z > 10°$, and of $\approx 5\mu$rad ($= 1''$) for $z > 20°$. This is typically four times in excess of the margin of Tables 5 and 7. The predictability is worst ($\approx 20\mu$rad) for zenith pointing—result of the kinetic mount—and besides az-axis runouts one of the few dependencies in the error budget that call it favorable to stay away from the zenith.

- The measured non-repeatable pointing error [141, p 29] is $\approx 0.15''$ on the sky for (A, z) ranges of $\approx 2'$—which we chose as a guideline because it equals the STS FOV. Through the effect shown in Fig. 29 below, this value of "misalignment" of the intended M1–M2–M3 axis by 0.15″ is equivalent to ≈ 34 nm in DOPD at $\tau = 60''$, or to ≈ 18 nm at $\tau = 30''$ (if orthogonal to the STS edge). In this case, the induced error does not depend on whether the distances to the STS edge are equal or not, because it is mediated through the first derivative of Fig. 29. These numbers already assume the removal of two individual tip-tilt's by operation of the M11/FSMs: IRIS could not improve on them.

It is expected that these numbers derived from driving the main telescope axis from the zenith down to 20 degrees of altitude and back are worst cases: both telescopes are driven through the same alt-az program in interferometric mode, so even the hystereses will partially compensate. We do not speculate of how much relief this aspect (of going one order further into the "differentials") could bring to the error budget

The "telescope performances assessment" in [141, §6] is concerned with image quality and pointing error: Note that the image quality computed as 32 nm RMS in [141, §6.1] relates to the image size *after* subtraction of the piston, the subject of Section 6, whereas we are here to the contrary interested in that piston *itself*.

13.5.5 Reports on Axis Stability

The stability of the AT horizontal and vertical axes is first of all related to the baseline definition, Section 11.4.3. This becomes obvious if one looks at placement on different AT stations as an extreme form of radial axis runout. The telescope axis is defined optically (through guiding and IRIS), not mechanically. The axis angular deviations are therefore removed to first order. A displacement of the M1–M2–M3 unit relative to the followup mirror train is left over and changes the foci/pupil positions and OPD/baseline for the longitudinal component, and looks like a change of the split ratio of the two off-axis angles for the lateral components, which induces residuals in the DOPD.

Sample calculations for telescope axial runouts of 20 μm and radial runouts of 20 μm follow. The effective displacement of the telescope pointing axis is a linear combination of the axial and radial runouts of the altitude and azimuth axes. The runouts of 11 μm and 19 μm for the AT#1 Az axis [134, §5] are comparable to the 10 μm and 31 μm of the AT#1 Alt axis [139, §6], of the 18.8 μm and 18.2 μm for the AT#3 Az axis [144, §6] and the 15 μm and 26 μm for the AT#3 Alt axis [143, §6]. Pairing AT#1 and #3 may enhance or subtract these effects to a degree that is not known and could only be estimated better if the angular dependence for the altitude axes would be known in the way it has been measured for the azimuth axes, and if one knew if there is some gravity-related correlation between these runouts. In summary, using 20 μm for radial and lateral displacements of the M1–M2–M3 positions is a realistic order of magnitude representing the relative runout.

Table 8 shows differential DOPDs induced for various zenith angles z, star separations $\tau = 1'$ (split evenly or with a ratio 1:2) and for two telescope azimuth angles A. The star rotator has not been corotated; so the two azimuth angles represent the field rotation angle relative to the STS edge. Active removal of a net tip-tilt with M11/FSM has been used as above. The DOPD is again $\propto \tau$, and of the order of 30 nm for this particular τ.

13.6 Conclusion

We estimate that the differential M1 tilt is not larger than $0.6''$ which is roughly 30 times the value allowed for a star separation of $20''$ (Tab. 7), and that the differential M2 tilt is not larger than $2''$ which is roughly 8 times the allowance for 5 nm of DOPD.

Expected pointing errors of $\approx 0.15''$ lead to differential OPDs of typically 40 nm, and axial runouts of 30 μm to typically 30 nm at star separations τ close to $1'$, after tip-tilt removal by the M11/FSMs. The numbers become smaller for smaller τ and depend on how the pointing error is aligned with the pointing of the STS edge.

Ideas to gather the information on the actual mirror positions are collected in Section 6 of [116]. These must be classified as an outlook on a virtual instrument, whereas the errors listed in the current technical report deal with the real instrument as being constructed.

z (deg)	$A=0°$		$A=45°$	
axis	$30''+30''$	$20''+40''$	$30''+30''$	$20''+40''$
0	0.	0.	0.	0.
30	0.	0.	7.	7.
45	0.	0.	5.	5.
60	0.	0.	0.	0.
axis	$30''+30''$	$20''+40''$	$30''+30''$	$20''+40''$
0	0.	0.	23.	23.
30	0.	0.	1.	1.
45	0.	0.	5.	5.
60	0.	0.	8.	8.
axis	$30''+30''$	$20''+40''$	$30''+30''$	$20''+40''$
0	33.	33.	23.	23.
30	33.	33.	22.	22.
45	33.	33.	21.	21.
60	33.	33.	19.	19.

Table 8: Differential OPDs as a result of 20 μm displacement of the pointing axis in units of nm. The top table is for axial displacements into the pointing direction, the middle table for radial displacements within the azimuthal plane, and the bottom table for radial, horizontal displacements perpendicular to the azimuthal plane. The numbers are the mean DOPDs across the pupil from the 29 test rays; the corrugations may be larger.

14 ABERRATIONS IN IMAGE PLANE OPTICAL COMPONENTS

14.1 Introduction

Pupil plane is set by AT M2. The specifications for the AT foci are shown in Table 9. The distances of the AT mirrors along the optical axis are given in Table 10.

Focus	f-ratio	focal length (m)	image scale (μm arcsec^{-1})	Field of view (arcmin)	(mm)
Nasmyth	25.0	45.0	218	8	104.6
Coudé	36.2	65.2	316	2	37.8

Table 9: AT Foci [39].

Mirror	Distance from last mirror (mm)	Physical distance from M1 along axis (mm)	Reimaged distance from f/1 image plane (mm)	Reimaged distance from M1 (m)
M1	0.0	0.0	Near pupil plane	0
M2	2493.4	2493.4	Pupil plane	32.586
M3	1793.4	4286.8	Near pupil plane	672.494
M4	1450.0	5736.8	199	
M5	1630.0	7366.8	Near pupil plane	
M6	950.0	8316.8	Pupil plane image	
M7	4400.0	12716.8	Near pupil plane	
M8	1344.6	14061.4	Near pupil plane	
D1	1954.0	16015.4		
D2	63.25	16078.7		
D3	63.25	16141.9		
M9	319.0	16460.9		
M10	370.0	16830.9		
M11/FSM	740.0	17570.9		

Table 10: D1 to D3 are the star rotator surfaces. The star rotator is not yet mentioned in [39] or [190], and the M9 position has been relocated 160 mm upwards from there.

The Airy disk radius after the M1 focus for $\lambda = 2.25$ μm at a telescope diameter of $d = 1.8$ m is $1.22\lambda/d \approx 1.53 \cdot 10^{-6}$ rad ≈ 0.31 arcsec, equivalent to a spot of 4.1 μm radius at a focal length of 2.7 m of the primary. With relative lateral magnifications of 16, 21 and 25 for the following foci (App. 14.3.2), this Airy disk radius grows to 69, 86 and 101 μm at these locations. (The last number could also be obtained by multiplying 0.31 arcsec with the image scale cited in Tab. 9 and Section 10.4 of [9].) These are fairly large areas compared to the roughness typically assumed for the mirror surfaces, which reduces the sensitivity of the results to the individual microscopic landscape on the mirror surfaces that are associated with individual directions within the FOV.

14.2 Dependencies

14.2.1 This error term is effected by

Error term	Relevant subsection
Wavefront amplitude and phase fluctuations above M1	5.3
Wavefront corrugations before and after the STS	6.3

14.3 Detailed contributions

14.3.1 M2 and M3 seen through M1

The entry for M2 in Tab. 10 means that the image of M2 seen through M1 is $1/(1/2700 - 1/2493.4)$ mm below M1 with the standard formula for thin lenses, where 2700 mm is the M1 focal length. This is to be taken with caution:

- the curvature of M2 means that its rim is 5.4 mm above its center; since both are close to the M1 focus, the apparent aperture of M2 (which limits the effective aperture of M1 from 1.82 to 1.80 m) seen through M1 would appear additional 95 cm below M1 with the thin lens formula.
- Only an off-axis beam could see the M2 aperture through M1, because the central radius of 69 mm of M1 would be shadowed by M2 itself. The only light that would enter parallel to the telescope axis and hit first M1 and then the rim of M2 must hit M1 close to its rim. This would see an image of M2 higher up, about 33.1 m below M1.

The entry for M3 means that the virtual image of M3 seen trough M2 would be 196 mm above M2, and this seen in addition through M1, from the point of view of the impinging stellar beam, would be lying 672 m below M1; the same remarks apply here, too.

14.3.2 Image planes

Use of the "Gaussian matrix" formulation for paraxial optics [67] and the parameters of curvatures and distances of the AT/STS ZEMAX file 9010 418 result in the locations of image planes:

The focal lens of M1 is 2.700 m, and the focal length of M2 is -0.2198 m. The (virtual) star image created by M1 is $(2.7-2.4934)$ m $= 0.2066$ m behind M2. With $1/x = 1/0.2198\text{m} - 1/0.2066\text{m}$ we get $x = 3.443$ m for the distance between M2 and its re-image of the star, which is $(3.443 + 2.4934)\text{m} = 5.936$ m behind the apex of M1. Continuation of this analysis locates the three real images

- $\approx$ 19.96 cm after M4 where the angle of incidence of incoming starlight towards the optical axis is $0.06001 = 1/16.66$ times the value for the (virtual) focus of M1. This distance is reproduced in Tab. 10: Nasmyth Focus.
- $\approx$ 85.25 cm after M6 where the angle of incidence of incoming starlight towards the optical axis is $0.0476187 = 1/21.000$ times the value for the (virtual) focus of M1.
- $\approx$ 3.78 cm after M10 where the angle of incidence of incoming starlight towards the optical axis is $0.015069 = 1/24.58$ times the value for the (virtual) focus of M1: Coudé Focus.

These results are to be taken with caution since continuing this calculation up to M10 puts the focus 3.7 cm away from M10, as listed, which by design ought to be an image plane. The discrepancy disappears in a full ray tracing which includes the conic constants of the near-to-spherical mirrors and the minimum distance of incoming light to the telescope axis enforced by the shadowing of M1 by M2.

14.3.3 AT M4 aberrations

M4 is not in an image plane, but is close enough to show a very substantial change in the footprint for off-axis stars. The beam radius on this flat elliptical mirror (major axes 40 mm and 56 mm) is ≈ 10 mm [39, Fig. 4] for zenith pointing, and the focus ≈ 20 cm away. This component comes before the STS, and before the laser metrology end point [116], so systematic error terms cannot be eliminated using the normal calibration procedures. The surface of this mirror must be modelled to nm accuracy in order to reach the astrometric accuracy required.

Property	Value
f / ratio	?
Plate scale	~ 0.48 mm arcsec^{-1}
Surface roughness	?
Beam diameter	20 mm

14.3.4 AT star separator aberrations

Star separator has one mirror in an image plane and other mirrors close to the image plane.

Property	Value
f / ratio	?
Plate scale	?
Surface roughness	?

14.3.5 Main delay line VCM aberrations

The VCM is very close to an image plane. The inflated mirrors are expected to show some pressure dependence, which may result in piston, wavefront tilt or pupil re-imaging errors being introduced into the beams. The performance of the VCMs will have to be investigated in detail.

Property	Value
f / ratio	?
Plate scale	?
Surface roughness	?
Beam diameter	?

14.3.6 Beam compressor

The middle mirror in the beam compressor is very close to an image plane

Property	Value
f / ratio	?
Plate scale	?
Surface roughness	?

15 IMAGE PLANE OPTICS IN THE STAR SEPARATOR

15.1 Introduction

The image plane(s) in the star separator positioned at the same location as the STS roof mirror (the mirror which separates the beams from the two stars) are particularly important as they play a crucial role in the fundamental calibration of PRIMA. The metrology system can be viewed as measuring the distance from the FSU input fibre spatial filter to this image plane in the STS. In this way the metrology system is creating a virtual reference surface within the ATs against which the narrow angle astrometry is performed. It is interesting to note that this reference surface is best defined by the image of the metrology system retroreflector (RR3) in the mirror RR2. This metrology system image plane is co-located with an image plane of the AT starlight beams. Any difference in the shape (curvature or tilt) of these co-located image planes will lead to a phase error which varies as the stellar images are moved around the image plane (note that there is complete freedom to move both stars around independently through the combined action of the derotator and the tip-tilt correction – the STS pick-off mirrors can ensure that the starlight and metrology beams reach the FSU even if the location of the stellar images moves around in this plane). It is thus critical that the two image planes are aligned at the sub-micron level, and that they have the same curvature.

15.2 Dependencies

15.2.1 This error term is effected by

Error term	Relevant subsection
Wavefront corrugations before and after the STS	6.3

15.2.2 Error terms effected by this

Error term	Relevant subsection
VLTI baseline geometry	11.4

15.3 Detailed contributions

Coordinates of the (virtual) image of the M11 center point in a global Cartesian coordinate system with M3 at the center are tabulated in Table 11. They have been calculated by emitting pairs of rays with acute angles to different surface points on M10 and intersecting their mirror images after final individual reflection off M1. The angles on the sky are measured relative to the telescope axis, and the angles in the lab relative to the line that connects the M10 and M11 centers. The results for the other star (the second M11) would be obtained by flipping the y-coordinates.

This particular ray tracing result is not really applicable, since no ray that is closer to the M11 center than approximately 10 percent of its radius would actually be emitted to the sky: these near-axis back-traced rays are reflected from M3 to M2 and back onto M3 instead of M1, trapped by the non-negligible diameter of M3. However, the table demonstrates that the optically defined baseline reference point of the telescope may well depend on the angle to the telescope axis, as a result of powered optics in the optical train upstream (M1, M2, M5, M7).

x (m)	y (m)	z (m)	sky angle (arcmin)	lab angle (deg)
0.000012	0.000001	-16.669	0.050	0.001
0.000043	0.000002	-17.904	0.100	0.003
0.000091	0.000004	-19.143	0.150	0.007
0.000158	0.000007	-20.387	0.199	0.013
0.000243	0.000010	-21.633	0.249	0.020
0.000347	0.000014	-22.886	0.299	0.029
0.000469	0.000019	-24.141	0.349	0.040
0.000609	0.000024	-25.400	0.399	0.052
0.000768	0.000030	-26.664	0.448	0.065
0.000947	0.000037	-27.931	0.498	0.081
0.001144	0.000045	-29.204	0.548	0.097
0.001360	0.000053	-30.479	0.598	0.115
0.001596	0.000062	-31.759	0.648	0.135
0.001851	0.000072	-33.043	0.697	0.156
0.002125	0.000082	-34.331	0.747	0.179
0.002419	0.000093	-35.623	0.797	0.202
0.002733	0.000105	-36.919	0.847	0.228
0.003066	0.000118	-38.219	0.897	0.254

Table 11: M11 center point images in a coordinate system centered at M3 where $+z$ points to the zenith, and $+x$ from M3 to M4.

16 ABERRATIONS IN PUPIL PLANE OPTICAL COMPONENTS

16.1 Introduction

Pupil plane is set by AT M2. The specifications for the AT foci and the distances of the AT mirrors along the optical axis are shown in Table 9.

16.2 Dependencies

16.2.1 This error term is effected by

Error term	Relevant subsection
Angle error between beams in STS calibration mode	6.3
Wavefront amplitude and phase fluctuations above M1	5.3

16.3 Detailed contributions

The nominal wave front aberrations from AT relay optics and STS optics are rather small, of the order of ±4 nm for star separations up to $\tau = 20''$, and of the order of ±10 nm for star separations of $\tau = 60''$, as shown in Fig. 34 for the "reference" position of zenith pointing. The toroidal shape of M16 removes a contribution of $\approx$ 80 nm of astigmatism that would otherwise exist in case of a simpler spherical surface. From this geometric model of the nominal optics (neglecting atmospheric turbulence and any flexures in the AT optical train) an irreducible inherent wave front error of a few nanometer emerges.

16.3.1 AT M1 aberrations

M1 is close to a pupil plane, and the beam wander is relatively small.

Property	Value
Beam diameter	1820 mm
Surface roughness	?

16.3.2 AT M2 aberrations

M2 is the pupil plane, and the beam wander vanishes by definition.

Property	Value
Beam diameter	138 mm
Surface roughness	?

16.3.3 AT M3 aberrations

M3 is close to a pupil plane, and the beam wander is relatively small.

Property	Value
Beam diameter	172×122 mm
Surface roughness	?

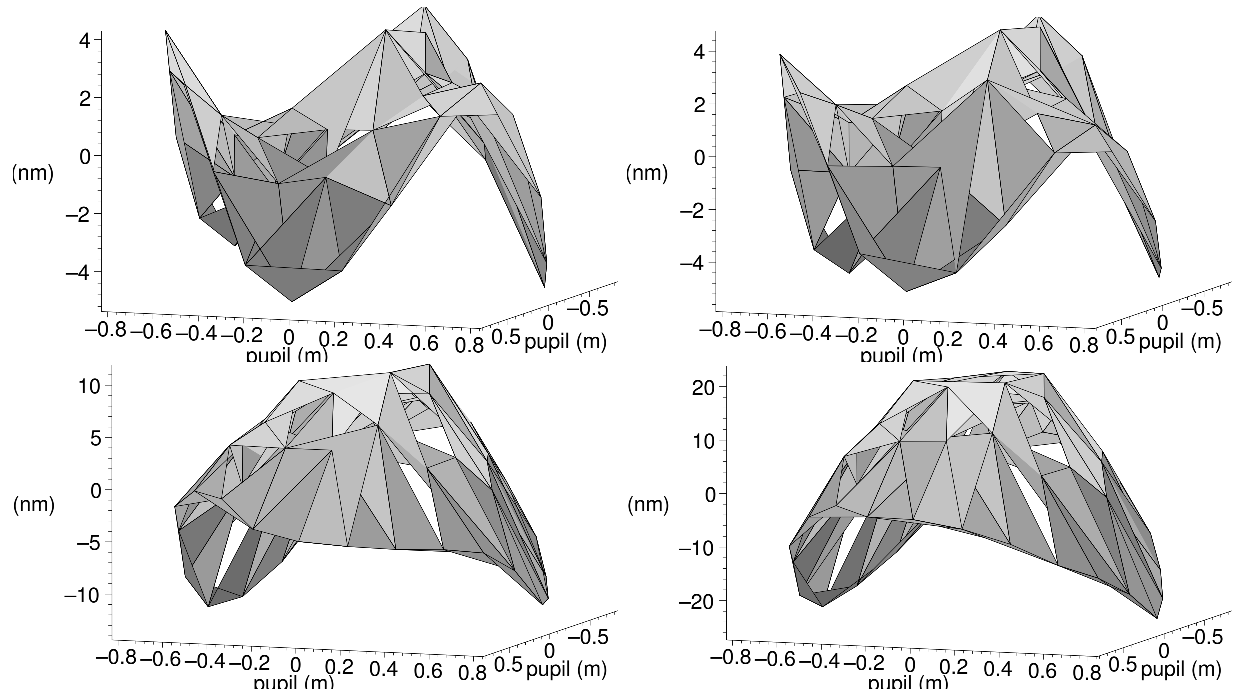

Figure 34: Residual OPL variation for a set of rays started above AT measured in a plane after M16 of the STS (before entering the light duct) after removal of a piston equivalent to Fig. 29, and after removal of tip and tilt. The parameters are star separations of $\tau = 0''$, $20''$, $60''$ and $90''$ from the left upper to the right lower figure.

16.3.4 AT M5 aberrations

M5 is close to a pupil plane, and the beam wander is 36 mm for a star wander of $2'$ [39, Fig. 5].

16.3.5 AT M6 aberrations

M6 is in a reimaged pupil plane, and the beam wander is very small.

16.3.6 AT M7 aberrations

M7 is close to a pupil plane, and the beam wander is 169 mm for a star wander of $2'$ [39, Fig. 7].

16.3.7 AT M8 aberrations

M8 is close to a pupil plane, and the beam wander is 108 mm for a star wander of $2'$ [39, Fig. 8].

16.3.8 AT derotator aberrations

16.3.9 AT window aberrations

16.3.10 Aberrations in star separator mirrors before image plane

16.3.11 Aberrations in star separator mirrors after image plane

16.3.12 Aberrations in M12 in MDL tunnel

16.3.13 Aberrations in M13 in MDL tunnel

16.3.14 Aberrations in M14 in MDL tunnel

16.3.15 Aberrations in M16 in MDL tunnel

16.3.16 Aberrations in pupil plane mirror of beam compressor

16.3.17 Aberrations in DDL window

16.3.18 Aberrations in pupil plane mirror of DDL

Property	Value
Beam diameter	?
Beam walk	? mm arcsec^{-1}
Surface roughness	?

17 BEAM WALK ON OPTICS BEFORE THE STS

17.1 Introduction

Light from the PS and SS follows different paths before the STS due to the angular separation of the stars on the sky. Surface errors in these mirrors can thus introduce systematic phase differences in the measurements. This effect cannot be eliminated by beam-switching for the mirrors which are hit before the de-rotator.

17.2 Dependencies

17.2.1 This error term is effected by

Error term	Relevant subsection
Wavefront amplitude and phase fluctuations above M1	5.3
Wavefront corrugations before and after the STS	6.3

18 VARIATION IN PRIMET LENGTH CALIBRATION

18.1 Introduction

This section deals purely with the metrology laser performance [162] (and not with variations in the refractive index, which are included in Section 9, nor with the influence of the STS mirror optics generating an anticipated r.m.s. error of 22 nm [133, §4.2.1]). We have been assured that the drift in the frequency of the laser is negligible, so little work will be required.

18.2 Dependencies

18.2.1 This error term is effected by

Error term	Relevant subsection
Ground level temperature, humidity and pressure fluctuations	E.3.2

18.3 Detailed contributions

There is a simple geometric dependence of the mean effective phase of a metrology laser bundle on its aperture angle caused by the longer path length of the rays further away from the optical axis [28, 108, 149], which may lead to a small bias of the actual reading on the total optical path length (ie, on the AT stations and VLTI DL offsets). A fringe intensity $\propto \cos^2(2K)$ measuring a phase $K = 2\pi L/\lambda$ for a single-path distance L between the laser source and the reflecting object is modified to become $\propto \cos^2(2K - \Delta)$ [108, (4.7)] [23, 177] where $\Delta = K\theta^2/2$ is a phase shift depending on the obliquity angle θ. Upper limits on θ are set by the size of the central aperture of 2.5 mm diameter in the beam splitter reserved for the metrology light [127, §3.4.26], which is to be halved because it has to be hit on return from the STS, and to be halved again because θ is meant to be half of the FOV seen by the metrology beam. A rough guess on the minimum distance L during interferometric operation is defined by the AT station on the mountain second-closest to the Interferometric Lab, which seems to be G0, at $L > 61$ m [119]. This would yield $\theta \approx 0.625 \cdot 10^{-3}/61$ rad, $L/\lambda \approx 61/1.32 \cdot 10^{-6}$, $K \approx 2\pi \cdot 4.5 \cdot 10^7$, and $K\theta^2/2 \approx 2.4 \cdot 10^{-3}$. Ignoring this effect of 2.4 milli-cycles can lead to a maximum misinterpretation of the OPL to the RR3 in the STS of $2.4 \cdot 10^{-3} \cdot 1.32\mu\text{m}/2 \approx 1.6$ nm.

18.4 Impact on astrometry

The standard operation of the PRIMET subsystem forsees infrequent (implicit) resets of the "phase counter" [46, 152]. The largest implicit correction to the data will probably stem from the drift of the tunnel air refractive indices between such a reset and the reading at the science data with the FSUs [117], which means that the explicit OPD variation as reported contains an implicit part from geometric motions and an implicit part from refractivity drifts.

19 SYSTEMATIC ERRORS IN THE FSU PHASE

19.1 Introduction

This section depends a lot of input from the designers and manufacturers of the PRIMA FSUs [19]. An important design aspect is that no fiber optics is used in the path before the beam combiner. Unlike with FINITO [14, 62],

- the strong group delay within the propagation through the fiber optics cannot add chromaticity to the dispersion in air, in the K-prism, and in the optional glass of the FSU "shutter" [104, 163].
- matching fiber lengths as described in [29] does not matter.

19.2 Dependencies

19.2.1 This error term is effected by

Error term	Relevant subsection
Atmospheric scintillation and thermal background fluctuations	25.3

19.3 Detailed contributions

Overshooting and chromaticity of the $\pi/2$ phaseshift in the K-prism lead to a non-ideal mixing of the polarizations as described in [3, 119].

Insufficient knowledge of the wavelength and temperature dependence of the glass material inserted by the FSU "shutter" for atmospheric dispersion correction [19] leads to errors.

The fiber coupling efficiency is intrinsically wavelength dependent since the diffraction-limited fiber core modes are matched with the electic field in the pupil plane [19, 119].

The chromatic TAD is equivalent to a chromatic beam tilt which translates into a (further) chromatic fiber coupling efficiency. An equivalent effect is induced by vertical temperature gradients [119].

Absorption in the beam splitter may cause extra phases [22].

20 KNOWLEDGE OF STELLAR SPECTRA

20.1 Introduction

If the PS and the SS have different spectra, they will be offset in position in the night sky due to atmospheric refraction [17]. The optical path length correction applied by the air delay lines will be different for each of the two stars, hence introducing an error into the differential astrometry measurements (note that this error is proportional to the offset of the main delay line from the point where the air paths are equalised). In order to subtract this effect, the spectral energy distribution of the correlated flux from each star will have to be accurately determined (see Sect. 4.2 in [122]).

20.2 Dependencies

20.2.1 Error terms effected by this

Error term	Relevant subsection
Refractive index of air and colour of correlated flux	9.3
VLTI baseline geometry	11.4

20.3 Impact on astrometry

21 TOTAL SPECTRAL RESPONSE OF PRIMA

21.1 Introduction

The total spectral response of PRIMA depends on many factors, including the FSU spectral sensitivity, the mirror reflectivities, and the combined effects of atmospheric refraction and the spatial filtering processes in the FSU and in the STS.

Most information on this subject is currently found in [119, 124]. For UT's equipped with AO this has been studied by M. Gai [63] and Felkel [49], and in terms of coupling efficiencies for the different Zernike modes, generally by Ruilier [157]. Standard diffraction theory shows how the blue components of spectra are enhanced [146]. Unfortunately, due to the lack of units on abscissa axes, the related figures on page 13 of [90] derived from VINCI data turn out to be of no value.

21.2 Dependencies

21.2.1 This error term is effected by

Error term	Relevant subsection
Atmospheric scintillation and thermal background fluctuations	25.3
Wavefront corrugations before and after the STS	6.3

21.2.2 Error terms effected by this

Error term	Relevant subsection
Refractive index of air and colour of correlated flux	9.3
VLTI baseline geometry	11.4

21.3 Detailed contributions

One of the promises of monomode fiber optics is the removal of corrugations across pupil planes ("cleaning" of the beams) by symmetric weighting of the electric field across the pupil. For this section, the transformation of phase screens has been studied by computation of the overlap with the anticipated far-field distribution of the PRIMA fiber optics of the FSUs [164]. The results are optimistic in the sense that fiber misalignment [178] has not yet been incorporated.

The survival of speckles is demonstrated by coupling 500 phase screens into a virtual photometric channel as if one would project a single telescope's input, reduced to the 18 mm beam width of the FSU, directly with the coupling lens onto the fiber head. The phase screens have been generated with a Kolmogorov spectrum by synthesizing Karhunen-Loéve basis functions as described in the literature [34, 156, 188]. The piston mode and the two modes that are almost equivalent to a pure tip-tilt have been discarded, and the 75 Karhunen-Loéve basis functions with the largest eigenvalues been retained. The phase mixing coefficients have been randomly generated with a Gaussian distribution equivalent to the structure function of Eq. (4) normalized to the Karhunen-Loéve eigenvalues.

These coupling efficiencies were derived from pure phase corrugation neglecting amplitude scintillation (see Sec. 25): the photometric fluctuations probably look worse than derived here. Absence of a tip-tilt component $m = 1$, $\phi \propto \cos(\vartheta)$ in the phase is important, since the intensity coupling factor from the azimuth integration in the overlap integral over the electrical fields becomes $|\int_0^{2\pi} e^{i\cos(\vartheta)}d\vartheta|^2/|\int_0^{2\pi} d\vartheta|^2 = J_0^2(1) \approx 0.59$, whereas it vanishes, $|\int_0^{2\pi}\cos(\vartheta)d\vartheta|^2/|\int_0^{2\pi} d\vartheta|^2 = 0$, in the equivalent amplitude mode. IRIS is designed to achieve this at up to 10 Hz [71, 138].

Results of this stability analysis are shown in Fig. 35 and 36 for sub-average and better-than-average seeing conditions [61, 137]. The scatter of the results is (much) wider than expected from the simulation in [63]—probably all related to the efficient AO correction in the phase screens used there. At stronger turbulence even complete drop-outs may occur [187].

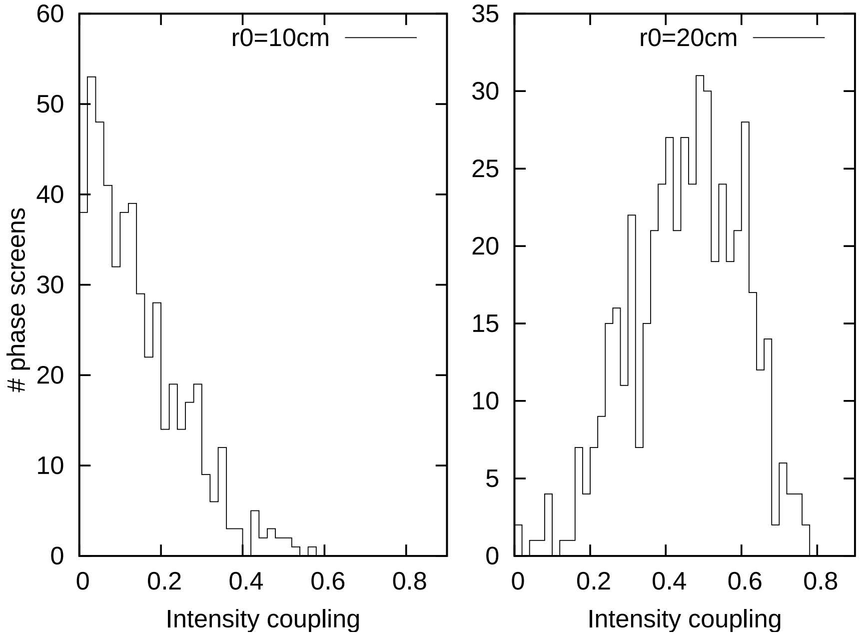

Figure 35: Statistics of intensity coupling coefficients for two sets of 500 phase screens over a $\rho = 1.8$ m telescope at a Fried parameter $r_0 = 60.8$ cm (left) and $r_0 = 121.6$ cm (right) for $\lambda = 2.25$ μm—equivalent to $r_0 = 10$ and 20 cm at $\lambda = 500$ nm by scaling $\propto \lambda^{6/5}$—coupled into the 8.5 μm fiber. 2.25 μm is the nominal central wavelength for the FSU center pixel.

Although simulation of the outputs of the interferometric ABCD channels would require more sophisticated coadding and subtraction of two-telescope's pupil phases, the anticipated variance must be similar to what is shown in Fig. 35 but—in the realm of the Taylor model of turbulence shifting—depend also on additional parameters of wind velocity, direction and baseline (Sect. 4.2, [55]). The qualitative argument is that the sum of two interferometric channels $A + C$ or $B + D$ roughly is a photometry, and that the astrometric mode turns to long baselines (Sect. 32) and uses the smaller ATs which diminishes the chance of correlated phase screens over the two telescopes. The operation of adding the electrical fields of phase screens and building the overlap with the fiber mode builds up variance in the cross terms (visibility). This anticipated variance of the visibility, however, is not necessarily a concern of the astrometric mode, but only a rephrasal of the inter-beam an-isoplanatism above the telescopes.

21.4 Conclusion

Fiber-mode optics cannot remove the phase corrugations anticipated at K-band wavelengths over a 1.8 m telescope pupil if only tip and tilt are removed. Values of fiber coupling parameters near 0.83

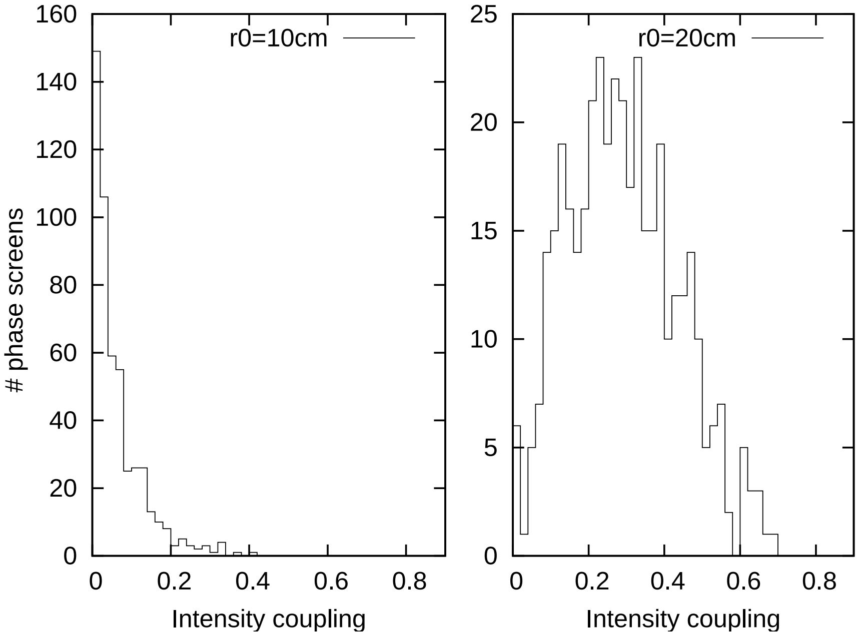

Figure 36: The statistics of Fig. 35 after switching to $\lambda = 1.71$ μm, which is the approximate photocenter of one of the two side pixels of the FSU (Fig. 26 in [120]), at a Fried parameter $r_0 = 43.7$ cm (left) and $r_0 = 87.5$ cm (right)—equivalent to $r_0 = 10$ and 20 cm at $\lambda = 500$ nm.

([62, Tab. 1]) would be unrealistic. To quote [155]: "*The net result is a dependance as* $r_0^{17/12} D^{-5/12}$ *which has the paradoxial implication to give a performance decrease for a diameter increase: the explanation is indeed the contrast loss due to the fast increase of the speckle number* N_s *when* D *grows.*"

22 INTERNAL VIBRATION IN THE VLTI

22.1 Introduction

Vibration in optical components in the VLTI will introduce fluctuations in the wavefront phase, particularly in the first three Zernike modes (piston mode and tip-tilt) [4]. These may reduce the S/N ratio for fringe tracking. Tip-tilt fluctuations may also result in a systematic error in the measured astrometric phase even if the mean tip and tilt are removed through the spatial filtering with the FSU fiber optics [157, 174, 183].

22.2 Dependencies

22.2.1 Error terms effected by this

Error term	Relevant subsection
Fringe jumps and group tracking errors	27.4
Wavefront corrugations before and after the STS	6.3

22.3 Detailed contributions

22.3.1 Reported OPL vibrations

Statistical (zero-mean) OPL jitters from vibrations have been characterized earlier [54, 140]. To first order, the contribution to the DOPD cancels if they are common-mode (that is, if they originate from mirrors before the STS hit by both star beams), see Sect. 13.5.2 and [124].

Analysis of the PSDs diagrams for the M1–M2 vibrations measured for AT#1 on pages 14–23 in [140] is difficult since the units on the ordinate axis are seriously defect. It does not make sense to believe that the values are close to $5 \cdot 10^{-10}$ nm^2/Hz, which would mean $\approx 5 \cdot 10^{-19}$ m^2/Hz if interpreted literally, or even $\approx 5 \cdot 10^{-28}$ m^2/Hz including parenthesis around the "nm." If one tries a re-analysis of the graph "displacements" for the velocities of 15″/sec in Az and 6″/sec in Alt, assuming that these values are correctly reported close to $8 \cdot 10^{-7}$ m, one gets $\approx 3 \cdot 10^{-15}$ m^2/Hz of the PSD of the displacements. With the additional factor of 2 to convert these to displacements (hence 4 in the PSD) one might expect $1 \cdot 10^{-14}$ m^2/Hz$= 1 \cdot 10^{-8}$ (mm)^2/Hz. Since there is some indication in the scripts of [140, App 3] that the raw data had been measured in mm as a function of seconds, we assume in the following interpretation that (i) the conversion factor of 2 for the transition from motion to OPL had already been applied in the HP interferometer data, and (ii) that the additional factor of 2 needed to include the contributions of the negative frequency spectrum had been dropped when calculating the PSD in [140] which we have to post-multiply, and (iii) that the units on the ordinates are then (mm)^2/Hz. The calculation of the r.m.s. of the graphs of the "OPL stability" has obviously been done in the time domain and would not be affected.

22.3.2 Performance of STRAP

RMS residual tip-tilt and temporal properties of the STRAP tip-tilt errors reach from 0.00724″ (sky) at Vmag=10 over 0.0235″ (sky) at Vmag=14 to 0.0721″ (sky) at Vmag=18 [147, Fig. 3.2.7-1]. Multiplied by a factor of 100 to transform these angles to the 18 mm beams on the PRIMA FSU, then combined with the table computed by Alenia [19, Fig. 4.3-12] gives estimates of the reduction of the fiber coupling efficiency from ≈ 0.73 (no tilt) to ≈ 0.66 (at the weakest natural guide star of Vmag=18). This will probably be overshadowed by the coupling efficiency variations caused by seeing (Sect. 21).

22.4 Impact on astrometry

The model OPD variations seen by the fringe tracker from atmospheric turbulence [40, Fig. 5-1] are $\approx 1 (\mu\mathrm{m})^2/\mathrm{Hz}$ at 1 Hz, $\approx 2.3 \cdot 10^{-5} (\mu\mathrm{m})^2/\mathrm{Hz}$ at 10 Hz, $\approx 10^{-8} (\mu\mathrm{m})^2/\mathrm{Hz}$ at 40 Hz, and $\approx 10^{-10} (\mu\mathrm{m})^2/\mathrm{Hz}$ at 90 Hz. The contributions from the mirror vibrations [140, p. 19] deduced as described above—but without a factor of 2 that would generate an OPD spectrum between two telescopes—are $\approx 1.5 \cdot 10^{-3} (\mu\mathrm{m})^2/\mathrm{Hz}$ at 1 Hz, $\approx 2 \cdot 10^{-6} (\mu\mathrm{m})^2/\mathrm{Hz}$ at 10 Hz, $\approx 2 \cdot 10^{-7} (\mu\mathrm{m})^2/\mathrm{Hz}$ at 40 Hz, and $\approx 5 \cdot 10^{-6} (\mu\mathrm{m})^2/\mathrm{Hz}$ at 90 Hz. In conclusion, at frequencies above 25 Hz the fringe tracker will have to deal mainly with the piston generated from the AT mirrors.

The actual tracking [91, Fig 10] superimposes a periodic saw-tooth pattern (probably caused by offloading the STRAP Coudé-table offsets) of a typical frequency of 2 Hz and 0.1 arcsec of amplitude. Table 5 implies that this becomes a ΔD signal of the order of 34 nm at the same frequency. (Scanning M5 with M6 means rotations around the U and W axis in this table.) This is an uncorrelated (unphased) motion on both telescopes, but at the same frequency depending on the velocity of the zenith changes caused by tracking. This adds an overlay of two saw-tooth signals of unknown relative phase (one from each telescope) since information on the timing is not available [185].

23 INTERNAL SEEING WITHIN THE VLTI

23.1 Introduction

Aspects of the tunnel seeing have been characterized before [43, 55, 68, 69, 70, 92, 105, 107, 128] and need to be reviewed. The impact of the beam tilt, added by the tunnel air, on fiber coupling efficiencies has been pointed out in [15]. Internal seeing imposes the limits of the blind tracking mode with the DDL, and also decides whether—even for stars of the same color—building the phasor products (17) produces mere noise.

23.2 Dependencies

23.2.1 This error term is effected by

Error term	Relevant subsection
Ground level temperature, humidity and pressure fluctuations	E.3.2
Air flow through the VLTI	B.3

23.2.2 Error terms effected by this

Error term	Relevant subsection
Wavefront corrugations before and after the STS	6.3

23.3 Detailed contributions

23.3.1 Dome seeing

23.3.2 AT internal seeing above primary

23.3.3 AT internal seeing below secondary

23.3.4 AT internal seeing between secondary and STRAP

23.3.5 AT internal seeing close to STRAP

23.3.6 AT internal seeing between STRAP and derotator

23.3.7 AT internal seeing between derotator and AT window

23.3.8 AT internal seeing between AT window and STS

23.3.9 AT internal seeing close to STS image plane

23.3.10 Seeing in AT duct

23.3.11 Seeing at interface between AT duct and MDL

23.3.12 Seeing in MDL

The OPD drifts of some μm per minute measured within the VLTI with VINCI [43] provide a warning that the beam swapping technique foreseen to remove some gradient effects between the two beams may become difficult, because this swapping is expected to need longer than a minute. The variation in water vapor content measured with the GENIE sensors is $< 10^{-3}$ mole/m^3 in 5 minutes [119, App.], with an associated change of $< 10^{-8}$ in the air refractive index, equivalent to an expected change in OPD of 1 μm over a path of 100 m; this matches the value of 1.21 μm over 300 s shown in [43, Fig. 6].

It is difficult to scale the results of [43] to the 0.24 m separation of the PRIMA beams, because the report specifies the air path by referring to "the AT light duct," which can mean anything up to 100 m if one does not remember the standard Siderostat positions of that time.

To predict the differential OPD of the PRIMA beams from the data, one needs (i) to assume isotropy of turbulence to convert flucutations along the beam direction to fluctutations in the transverse direction, ie, to assume that both beams are taken from the same statistical ensemble—see [81] for an investigation that compares horizontal and vertical statistics—, (ii) to deduce the correlation length (the characteristic width of the spatial structure function) of the density fluctuations with some sort of ergodic hypothesis from the temporal structure function implicitly provided by the paper (taking the role of Taylor's frozen turbulence in main-stream 2-telescope interferometry). If the correlation length is much larger than 24 cm, the differential OPD approaches zero, otherwise its variance is ~ 1 μm of the single beam.

A comparison of Tables 9 and 10 in [105] shows that moving the two beams 80 m through the UT3 duct, the differential OPL fluctuations are about half as large as the fluctuations within a single beam; the differential OPL fluctuations in the delay line tunnel (Table 19) are only about 10% of the value in the duct.

23.3.13 Seeing in MDL carriage

23.3.14 Seeing near image plane of MDL carriage

23.3.15 Seeing in interface between tunnel and lab

23.3.16 Seeing in lab

23.3.17 Seeing in beam compressor cats eye

23.3.18 Seeing in DDL if air filled

23.4 Impact on astrometry

23.4.1 Impact on the FTS Mode

Residual differential phase fluctuations add a term $\phi(t)$ in the correlated intensities

$$\left\{\begin{array}{c} A \\ B \\ C \\ D \end{array}\right\} = \int e(k)\{1+\cos[n(k)kD_t - kD + \left\{\begin{array}{c} 0 \\ \pi/2 \\ \pi \\ 3\pi/2 \end{array}\right\} + \phi(t)]\}dk \qquad (36)$$

of the interferograms of the beam that is scanned in the Fourier Transform Spectrometer mode. If $\phi(t)$ has a white noise spectrum, and the spectra are scanned slowly in the sense that a sufficiently high integration time builds a mean over the statistics at each point in the interferogram, each point in the interferograms $A-C$ and $D-B$ is effectively multiplied by the same Strehl factor $\exp(-\sigma_\phi^2/2)$ [98], and the resolution in the spectrum remains unharmed.

However, it is more likely that the phase fluctuations stem from density fluctuations and have the wave number-dependent variance $\sigma_\phi^2 = \sigma_n^2\, k\delta h$ induced by the equivalent fluctuations in the index of refraction. If we assume Gaussian statistics for the fluctuations in n with variance σ_n^2, the points in the spectrum are effectively multiplied by the Strehl factor $\exp[-(k\,\delta h\,\sigma_n)^2/2] \sim \exp[-D_\phi^2/2]$ in the slow-scan mode. The negative impact of large σ_n^2 to the spectrum is therefore an apodization—multiplication by this factor $\propto \exp(\sim k^2)$—which may reduce the contribution of the K band spectrum $4000\ \mathrm{cm}^{-1} \leq 2\pi k \leq 5200\ \mathrm{cm}^{-1}$ below the noise level, if the k-independent factor in the exponential becomes too large. The alternative in this case is to use fast scans such that the turbulence in the phase can be regarded as frozen while taking one interferogram. This linear phase in k can then be deduced off-line for each scan over the two interferograms, which are eventually coadded coherently by software.

24 DETECTOR NOISE AND PHOTON SHOT NOISE

24.1 Introduction

Detector noise and photon shot noise are expected to limit the sensitivity of PRIMA observations, but are not expected to introduce significant systematic errors into the astrometric observations. The simulations presented in this document do not take account of detector noise and photon shot noise – it will be important to incorporate these effects in the models of the fringe tracking performance discussed in Section 27.

24.2 Dependencies

Estimations on the S/N as a function of star luminosity, detector integration time and spectral coverage of the detector pixels are given in [120].

24.2.1 Error terms effected by this

Error term	Relevant subsection
Fringe jumps and group tracking errors	27.4
Systematic errors in the FSU phase	19.3

25 ATMOSPHERIC SCINTILLATION AND THERMAL BACKGROUND FLUCTUATIONS

25.1 Introduction

25.1.1 Scintillation

Phase perturbations in the wavefronts from a star produce fluctuations in the optical amplitude after the light has propagated down through the atmosphere. The phase measured by the FSU corresponds to an integral of the contributions over both AT pupil planes, and this measurement will naturally be weighted by the amplitude at each point in the pupil plane. In the absence of internal seeing within the VLTI and with accurate pupil relay the scintillation in the pupil plane in front of the FSU will match the scintillation across the AT aperture. However, if there is internal seeing within the VLTI away from the pupil plane additional scintillation can be generated at the FSU. Incorrect pupil relay can also modify the level of scintillation at the FSU.

The simulations described in Section 4 were used to investigate the approximate level of scintillation expected at the telescope aperture. Example plots from 4 timesteps of the simulations were shown in Section 5. Figure 12 shows the optical amplitude as a function of position in the AT aperture plane. It is clear that the amplitude fluctuations are dominated by one of the layers moving from the upper right to the lower left. The dominant layer is the higher one (5 km above the telescope – see Section 4.2).

25.2 Dependencies

25.2.1 This error term is effected by

Error term	Relevant subsection
Wavefront amplitude and phase fluctuations above M1	5.3
Wavefront corrugations before and after the STS	6.3
Ground level temperature, humidity and pressure fluctuations	E.3.2
Air flow through the VLTI	B.3

25.2.2 Error terms effected by this

Error term	Relevant subsection
Fringe jumps and group tracking errors	27.4
Systematic errors in the FSU phase	19.3

25.3 Detailed contributions

25.3.1 Scintillation

Effect of scintillation

25.3.2 Thermal background fluctuations

Effect of thermal background fluctuations

26 SYSTEMATIC EFFECTS FROM THE ATMOSPHERE

26.1 Introduction

The curvature of the earth and the atmosphere above add chromatic OPD's between the two ends of the K-band of up to 17 μm [119]; this effects both fringe trackers individually and is one of the effects that do not inherently cancel from the differential point of view.

The curvature also necessitates correction of the earth-bound baseline length with respect to the lensing effect of the atmosphere [18, 119], which could amount to 0.5 mm at large baselines and low zenith angles. (The stability of the fringe positions was 0.6 mm in 2002 [186].)

Large scale gradients could be produced in the atmosphere by the effects of nearby mountains or the Pacific Ocean. These gradients are known to effect conventional astrometric observations [77].

Wind speed profiles over the mountain have been studied by García-Lorenzo et al [66]. The 1992 balloon data [111] have been analysed in terms of phase variations before [35]. Seeing in the wake of UT domes is characterized in `http://www.eso.org/gen-fac/pubs/astclim/paranal/seeing/buildingwake/`.

26.2 Dependencies

26.2.1 This error term is effected by

Error term	Relevant subsection
Large scale structure in the atmosphere above Paranal	E.3

26.3 Detailed contributions

26.3.1 Horizontal air density gradient

Mostly from temperature, but also from pressure

26.3.2 Horizontal water vapour density gradient

From absolute humidity

26.3.3 Isoplanatism

A summary of computations derived from profiles of the 1992 Balloon Data [36] is given in Section 9.1.3.2 of [147].

An isoplanatic angle [99, 100, 110] of 17" is reported by Cresci et al. [33] derived from NACO. The isoplanatic angle for adaptive optics was recomputed from scintillation data and estimated at 2" on the mean [159], and is logged in `http://www.eso.org/gen-fac/pubs/astclim/forecast/meteo/CIRA/images/repository/teta0/`.

The anisoplanatic angle (for a fringe visibility reduction not smaller than 80% or a residual piston error smaller than $\lambda/10$) was estimated at 27 arcsec for Paranal in the K-Band [20, 50] at an outer scale $L_0 = 20$ m [32, 195]. Also based on [36], the total detector exposure time was estimated to limit the separation angle to 15" [42] which probably sets a more realistic upper limit to the typical scenario [40, Fig. 5-15].

26.4 Conclusion

Isoplanatism is—from the interferometric point of view—a matching between phases of "equivalent" portions of the wavefronts superimposed in the plane of an aereal beam combiner. The—less restrictive—single telescope request would only match phases between the two stars. The interferometric definition is unlikely fulfilled if the baselines are much longer than the outer scale of turbulence; for AT observations, this becomes even more improbable since the long baselines are established by mixed telescope positions North and South of the delay line tunnel, which generates differential field rotations for both telescopes [72][147, §3.2.2]. Attempts to counter-rotate with the derotator mirror set (Fig. 30) would induce polarization effects [131].

27 FRINGE JUMPS AND GROUP TRACKING ERRORS

27.1 Preamble

In case one looks at PRIMA as yet another external fringe tracker in support of other instruments of the VLTI, one would focus on "high quality" (stiffness of the tracker's response function, its capability to adapt to various atmospheric conditions). In contrast, the astrometric data reduction will expect recording of the full PRIMA data set of the ABCD channels, which puts less stringent requests on the online fringe tracker and its performance in either tracking on a fringe intensity maximum or a maximum of the fringe envelope. In general, *a posteriori* fringe tracking [74] is possible, but with the low spectral resolution put into the FSU design, the standard Fourier transform methods are not at hand.

27.2 Introduction

Fringe tracking in an interferometer with large apertures and spatial filters is known to be very challenging. There are three regimes of interest to PRIMA:

1. Observations where the performance is limited by the S/N for active fringe tracking
2. Observations where the performance is limited by the S/N for passive observations of the SS when the fringes are phase-stabilised using the PS
3. Observations where the performance is limited by the S/N for passive observations of the SS when the fringes are not phase-stabilised.

Under regime 1 above, the configuration of the VLTI should be optimised to provided maximum S/N ratio on the PS. Under typical Paranal seeing conditions the AT diameter is close to the optimum for fringe tracking S/N with ideal tip-tilt correction – under poorer seeing or poorer tip-tilt correction it may be beneficial to stop down the aperture diameter at the FSU. The results of simple simulations which investigate the performance of the group tracking performance on seeing and aperture diameter are presented in later this section. The added complication for the baseline geometry if the pupil is stopped down may outweigh the benefit in fringe-tracking performance. If the UTs are used there may be a stronger case for stopping down the apertures, particularly if the AO system can be matched to the stopped-down aperture geometry.

Under regime 2 above, the configuration of the VLTI should be optimised to provided maximum S/N ratio on the SS. As the fringes are phase-stabilised, this simply requires the flux through the spatial filter to be optimised. [89] shows that even for simple tip-tilt correction the optimum aperture size can be as large as $6r_0$ for an interferometer with spatial filters, so the AT apertures will never have to be stopped down. It also seems likely that the UT apertures would not need to be stopped down to a smaller diameter if MACAO was used in PRIMA observations.

Regime 3 will require more detailed analysis, although it is expected that the optimum operating conditions will be similar to those for regime 1.

The precise performance of PRIMA will also depend on specific characteristics such as the wavelength separation of the group delay tracking channels, the bandpass of the phase-tracking channel and the performance of the tip-tilt correction. For this reason, numerical simulations which are more PRIMA-specific will be required in order to produce a realistic model of the fringe-tracking performance of PRIMA.

27.3 Dependencies

27.3.1 This error term is effected by

Error term	Relevant subsection
Atmospheric scintillation and thermal background fluctuations	25.3
Wavefront corrugations before and after the STS	6.3
Refractive index of air and colour of correlated flux	9.3
Wavefront amplitude and phase fluctuations above M1	5.3
Internal vibration in the VLTI	22.3.1

27.4 Detailed contributions

27.4.1 Simulations of PRIMA operation with the ATs

In order to investigate potential sources of noise in the fringe tracking process, the simulations described in Section 4 were modified to include a simple fringe tracking algorithm [179, 180]. Optical propagation through the VLTI was not modelled – the spatially filtered output from two telescope simulations was simply combined to form an interferometer. In the fringe tracking algorithm, the phases of the seven spectral channels used in the simulation were adjusted so as to subtract the fringe offset measured in the previous timestep (or according to the piston mode if it was the first timestep). The seven channels were then combined to produce the two group delay tracking channels and the one phase tracking channel analogous to the PRIMA FSU spectral channels, as described in Section 4.2. The group delay tracking channels were then used to produce an estimate of the change in group delay, and this was used to find the nearest zero-point in the fringe phase.

One of the first interesting results to come out of these simulations was just how difficult group delay estimation is using the two widely spaced wavelength channels from the PRIMA FSU design, particularly during periods of less-than-ideal seeing. When the stellar images at the telescopes are distorted by wavefront corrugations across the telescope apertures, the phases of the fringes in the group delay tracking channels are also perturbed. This perturbation is different in the two different spectral channels, which produces a substantial error in the calculated group delay. This problem was partially solved by low-pass filtering the group delay measurements, causing perturbations due to the atmosphere to be averaged out over 5—10 time units (where one time unit corresponds to the time taken for each atmospheric layer to move r_0, as discussed in Section 4). The fringe tracking algorithm was then found to perform very well, with fringe jumps detected only every few hundred fringe coherence times. Example plots of the fringe tracking performance are shown in Figures 37 and 38. If the group delay measurements are averaged over too long a period, the algorithm is not able to track the motion of the fringes due to the atmospheric piston mode fluctuations.

These preliminary simulations have also been useful in determining which factors will have the most impact on fringe tracking performance, and hence which should be studied in more detail. Simulations were performed with seeing of $r_0 = 0.45$ m and seeing of $r_0 = 0.9$ m at K band (see Section 3.1 for an introduction to atmospheric seeing – these numbers correspond approximately to the following two sets of conditions which might be compared with the NACO results [61]: observing a target at low elevation under below average seeing; and observing a target at the Zenith under excellent seeing). Both the full aperture (1.8 m) and a stopped-down aperture (1.2 m) were simulated. A summary of the simulation characteristics is presented in Table 12. Temporal power spectra of the fringe motion are plotted in Figure 40 for these simulations. Characteristic wind velocities are $v \approx 30$ m/s [147,

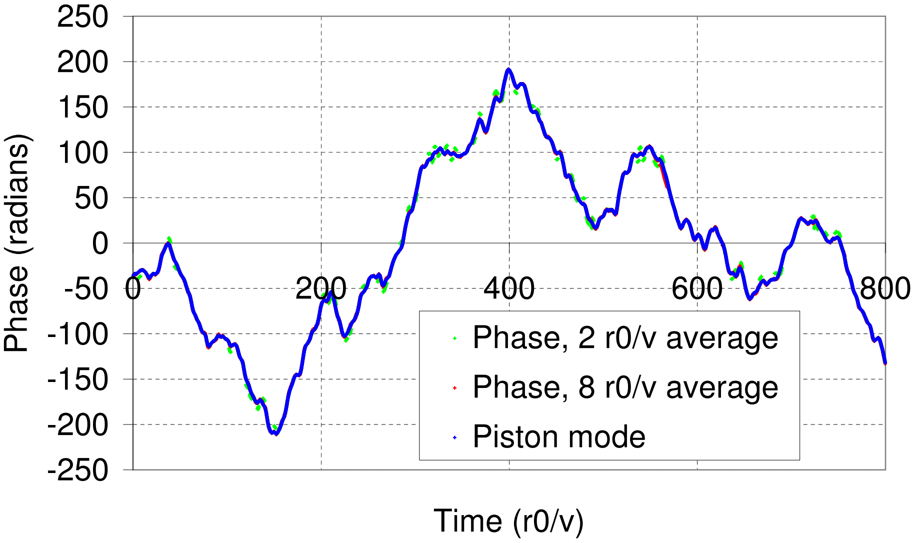

Figure 37: The measured optical phase compared with the piston mode in simulations. The curve labelled *Phase,* $2r_0/v$ *average* shows the optical phase in a simulation where the group delay used in unwrapping the phase is the average group delay over a time period 2 time units ($2r_0/v$). For *Phase,* $8r_0/v$ *average* the averaging is performed over 8 time units. Also shown is the piston mode component. All curves are for the same atmosphere. Photon shot noise and detector noise were not included (the optical phase measurements were noiseless).

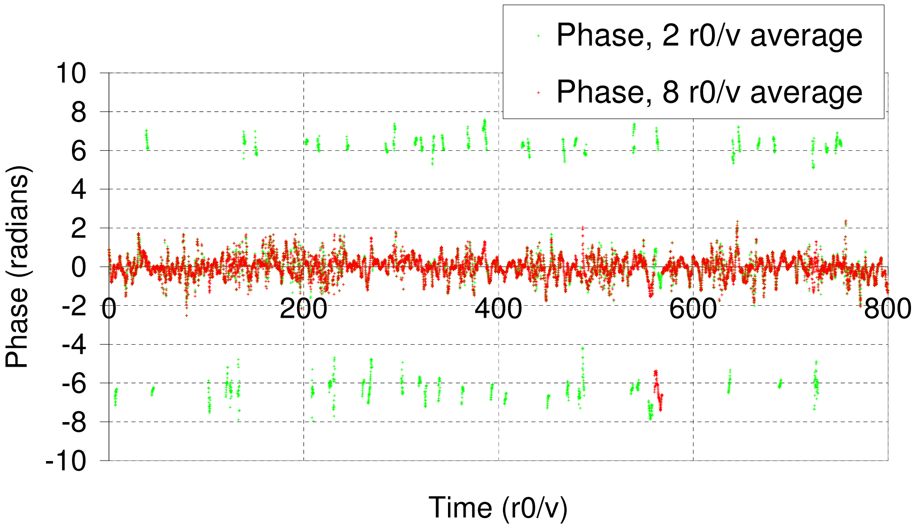

Figure 38: The same data as Figure 37 but the piston mode component has been subtracted from the optical phase data for clarity.

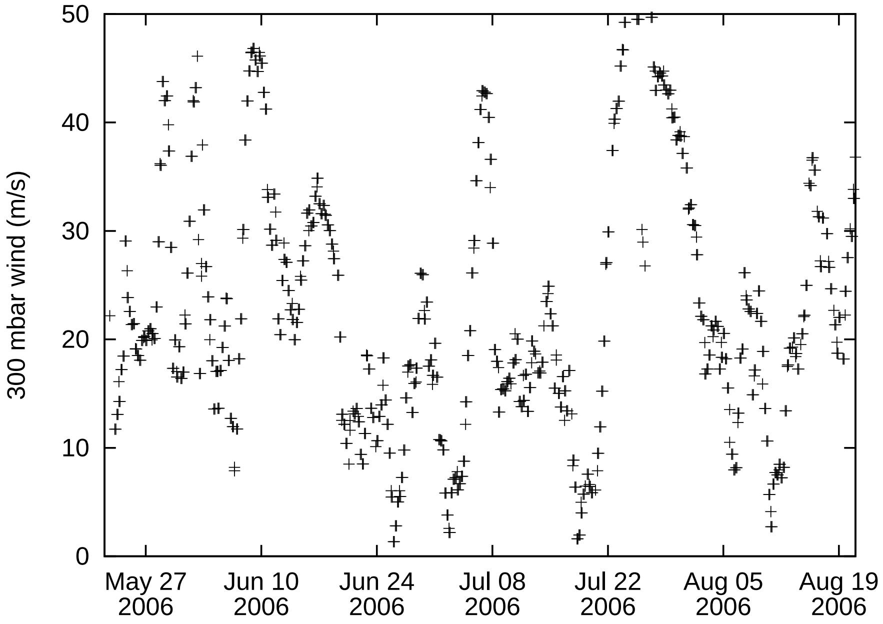

Figure 39: Paranal wind velocities at a pressure level of 300 mbar from the files `par_dapp.txt` in the wheather satellite package `latest_forecasts.tar.gz`.

Table 12: Simulations of fringe tracking.

	Simulation 1	Simulation 2	Simulation 3	Simulation 4
K band r_0	0.45 m	0.9 m	0.45 m	0.9 m
Seeing* if $z = 0°$	1.4"	0.68"	1.4"	0.68"
Seeing* if $z = 60°$	0.89"	0.45"	0.89"	0.45"
Aperture diameter	1.8 m	1.8 m	1.2 m	1.2 m

*500 nm Zenith seeing which would give the appropriate K band r_0 for observations at the Zenith angle z listed.

Fig. 9.1.2-4][66] and measured remotely each 3 hours: Fig. 39.

It is clear from the power spectra in Figure 40 that the fringe motion at high frequencies is dominated by the wavefront corrugations across the aperture in all the simulations, and the piston mode component (discussed in e.g. [37]) is negligible. Note that the piston mode component has a larger high frequency component with smaller aperture sizes as expected, but this is swamped by the effects of wavefront corrugations across the AT aperture (and vibrations in the AT optics not simulated here), which are much smaller with the smaller aperture size. It is clear that the fringe tracking performance will be determined mostly by the effects of these wavefront corrugations, and that the slow drifts from the piston mode component will be much less important in optimising the fringe tracking algorithm.

The maximum aperture diameter which can successfully used for fringe tracking will be set by the amount of fringe jitter introduced by the wavefront corrugations across the aperture. It is interesting to compare the fringe jitter under different seeing conditions and with different aperture diameters. In this case I have defined the jitter as the residual fringe phase after the piston mode component has been subtracted. There was no photon shot noise or detector noise in these simulations, so this phase

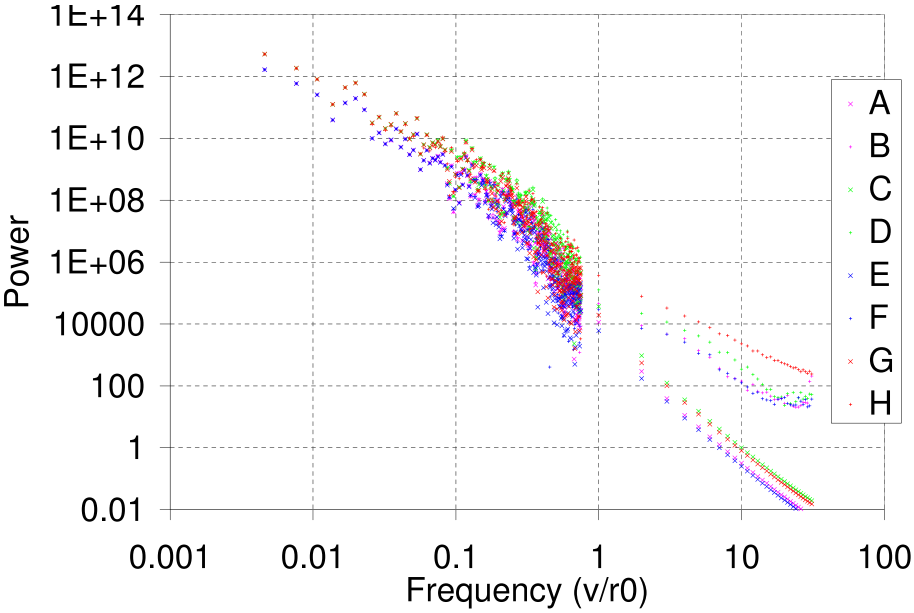

Figure 40: Temporal power spectra of fringe motion. *A* and *B* show the temporal power spectrum of the piston mode and of the fringe phase for simulation 4 (small aperture, good seeing). *C* and *D* show the same for simulation 3 (small aperture, poor seeing). *E* and *F* show the same for simulation 2 (large aperture, good seeing). *G* and *H* show the same for simulation 1 (large aperture, poor seeing). At high frequencies many the datapoints have been binned together and averaged for clarity. The frequency axis is normalised for v/r_0 with the r_0 for the poorer seeing conditions (the Taylor screens moved at the same physical velocity with the good seeing conditions).

Table 13: Phase jitter resulting from wavefront corrugations in the aperture plane.

	Simulation 1	Simulation 2	Simulation 3	Simulation 4
K band r_0	0.45 m	0.9 m	0.45 m	0.9 m
Aperture diameter	1.8 m	1.8 m	1.2 m	1.2 m
RMS phase jitter	0.81 radians	0.31 radians	0.38 radians	0.30 radians

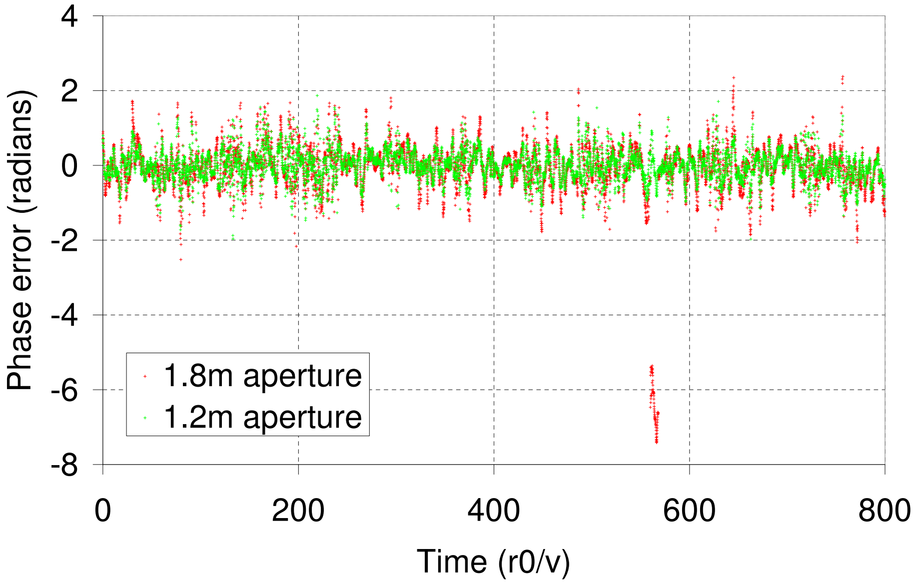

Figure 41: The amount of phase jitter introduced by wavefront corrugations in the aperture plane of an AT. The jitter with the full 1.8 m is shown along with the result when the aperture is stopped-down to 1.2 m diameter. Both simulations used the same atmosphere. Photon shot noise and detector noise were not included (the optical phase measurements were noiseless).

difference corresponded directly to the effect of the wavefront corrugations across the aperture plane. A summary of the simulation characteristics and results is presented in Table 13 (the simulations are the same as those presented in Table 12). The likelihood of fringe jumps should be small as long as the RMS fringe jitter $\ll 1$ radian.

The phase jitter with the full diameter aperture under the poorer seeing conditions (Simulation 1) is clearly much worse than the other cases. Stopping down the AT aperture provides a very significant reduction in the phase jitter, and appears a promising option at times when fringe tracking becomes very unreliable. Note that the very high phase jitter for Simulation 1 is partly due to a small number of very large phase excursions including fringe jumps, an example of which is shown in Figure 41. Note that the RMS phase jitter is lower for the 1.2 m diameter aperture at all times, however. The loss of stellar flux would make stopping down the telescope aperture less appealing for faint stars.

27.4.2 Estimated performance of PRIMA with the UTs

Simulations of PRIMA performance with the UTs have not been undertaken, however some estimates of the probable performance can be made using general properties of optical interferometers. Figure 42 shows the light collected through a spatial filter per coherence time of the interference fringes for a typical interferometer with different levels of AO correction (but all under the same

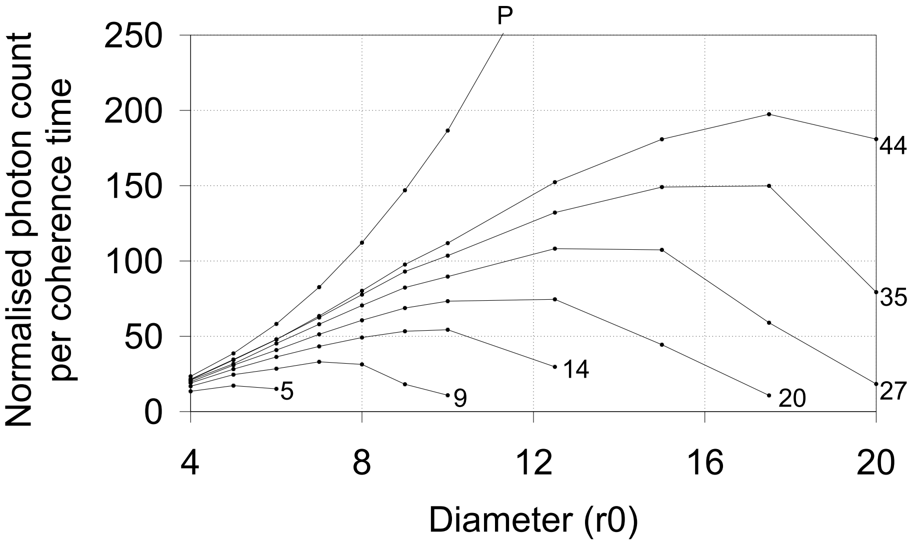

Figure 42: The photon count through a spatial filter per coherence timescale normalised so that a diffraction-limited aperture of diameter r_0 would give unity. The labels on the lines indicate the number of Zernike modes corrected from tip-tilt upwards (describing the level of AO correction). The curve labelled “P” corresponds to the result expected for piston mode only simulations (i.e. with ideal AO correction – see e.g. [37]). All curves are for the same seeing conditions.

seeing conditions). In this case the AO correction involved ideal compensation of a finite number of Zernike modes (with the modes matched to the aperture diameter used). The decrease in signal for large apertures and low-order AO correction is due to the reduced coherence time for the fringes when the variance in the wavefront phase across the aperture increases beyond 1 radian. It is not clear which (if any) of these curves would correspond to the MACAO system. It is interesting to note that the S/N ratio is optimised when the Strehl ratio is ∼ 30% for all the AO correction models shown here. More realistic simulations of the VLTI would probably be required in order to optimise the operation of PRIMA using the UTs.

28 DATE AND TIME OF THE OBSERVATIONS

28.1 Introduction

Mean azimuths $\bar{A}$ (measured from the baseline), mean zenith angles $\bar{z}$ of the pair of stars that boost the geometrical fraction in (59) ought be avoided, because errors in the inputs, that is in the "global" star positions and in the differential OPD, are multiplied by this term.

28.2 Dependencies

28.2.1 Error terms effected by this

Error term	Relevant subsection

28.3 Detailed contributions

28.3.1 Interferometric Resolution

The interpretation of (59) in terms of interferometric resolution of the astrometric angle τ follows [132, 2.4.2.2]. The projected baseline **P**, the baseline **b** and the extended (mean) star direction **s** (which was defined with unit length in (53)) form a triangle shown in Fig. 51,

$$\mathbf{b} = \sqrt{b^2 + P^2}\,\mathbf{s} + \mathbf{P}, \qquad P \equiv |\mathbf{P}|, \quad b \equiv |\mathbf{b}|, \quad |\mathbf{s}| = 1. \tag{37}$$

The cosine of the angle between **s** and **b** in this triangle is from the dot product of (53)

$$\cos a = \cos \bar{A} \sin \bar{z} = \frac{P}{\sqrt{b^2 + P^2}}, \tag{38}$$

which inserted into the previous equation yields an expression for **P** in Cartesian coordinates

$$\mathbf{P} = \begin{pmatrix} P - b \\ P \tan \bar{A} \\ P/(\cos \bar{A} \tan \bar{z}) \end{pmatrix}. \tag{39}$$

We decompose this vector into the orthogonal coordinate system centered at the mean position $(\bar{A}, \bar{z})$ with unit vectors into the directions of increasing A, decreasing z, and radially outwards, sketched in the middle of Fig. 51:

$$\mathbf{e}_A = \begin{pmatrix} -\sin \bar{A} \\ \cos \bar{A} \\ 0 \end{pmatrix}, \quad \mathbf{e}_z = \begin{pmatrix} -\cos \bar{A} \cos \bar{z} \\ -\sin \bar{A} \cos \bar{z} \\ \sin \bar{z} \end{pmatrix}, \quad \mathbf{e}_r = \begin{pmatrix} \cos \bar{A} \sin \bar{z} \\ \sin \bar{A} \sin \bar{z} \\ \cos \bar{z} \end{pmatrix}, \quad \mathbf{e}_r \times \mathbf{e}_A = \mathbf{e}_z. \tag{40}$$

Building the dot products $\mathbf{P} \cdot \mathbf{e}_z$ and $\mathbf{P} \cdot \mathbf{e}_A$ we get

$$\mathbf{P} = b \sin \bar{A} \mathbf{e}_z + b \cos \bar{A} \sin \bar{z} \xi \mathbf{e}_A + \ldots \mathbf{e}_r, \tag{41}$$

where the coefficients in front of $\mathbf{e}_z$ and $\mathbf{e}_z$ identify the rotation angle ξ of the projection of **P** on the tangential plane spanned by $(\mathbf{e}_A, \mathbf{e}_z)$,

$$\cos \xi = \cos \bar{A} \cos \bar{z}, \quad \sin \xi = \sin \bar{A}. \tag{42}$$

This allows to rewrite the denominator in (59) as

$$\sin \bar{A} \sin \varphi - \cos \bar{A} \cos \bar{z} \cos \varphi = -\cos(\varphi + \xi). \tag{43}$$

Another look at Fig. 51 shows that this angle $\varphi + \xi$ describes how far the star pair axis is rotated off the plane spanned between the baseline and projected baseline. The calculation of the projected baseline angle is discussed in [121, 123]. It shows that $\varphi + \xi$ equals $p_{\text{SS}} - p_b$, the difference between the position angle of the SS and the position angle of the projected baseline (where the orientation of the projected baseline vector is opposite to the one chosen here).

28.3.2 Propagation of OPD Errors

Eq. (59) means that the *relative* error derived for τ equals the *relative* error made in $\Delta D/b$, which is the sum of the relative errors in ΔD and b supposed the mean position $(\bar{A}, \bar{z})$ of the pair and its orientation φ are known (which has of course been noted before [165, §3.2]). For 10 μas absolute accuracy over a 2 arcmin FOV the relative error may be required to drop below $10 \cdot 10^{-6}/120 \approx 8 \cdot 10^{-8}$. The *absolute* error in τ (in radians) equals the absolute error in $\Delta D/b$ multiplied by a geometric factor that is illustrated in Fig. 44. The pole along some line in the $(\bar{A}, \bar{z})$-plane means hypersensitivity of τ to the differential OPD; these are directions on the sky where $\Delta D = \cos(\varphi + \xi) = 0$ though $\tau \neq 0$ (Fig. 43).

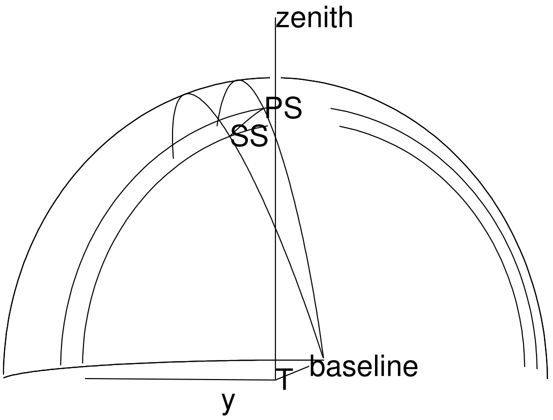

Figure 43: The two stars can individually be moved on two circles around the baseline vector, which does not change their OPD, does not change the DOPD, but obviously does change their separation τ.

This happens if both stars lie on the same circle around the basline direction, and corresponds to zeros of the differential OPD that occur periodically as illustrated in Fig. 45. (A similar figure is found in [169].) The time delay between the zeros of the DOPD and the OPD provides a mean to measure the co-zenith φ of the SS relative to the PS.

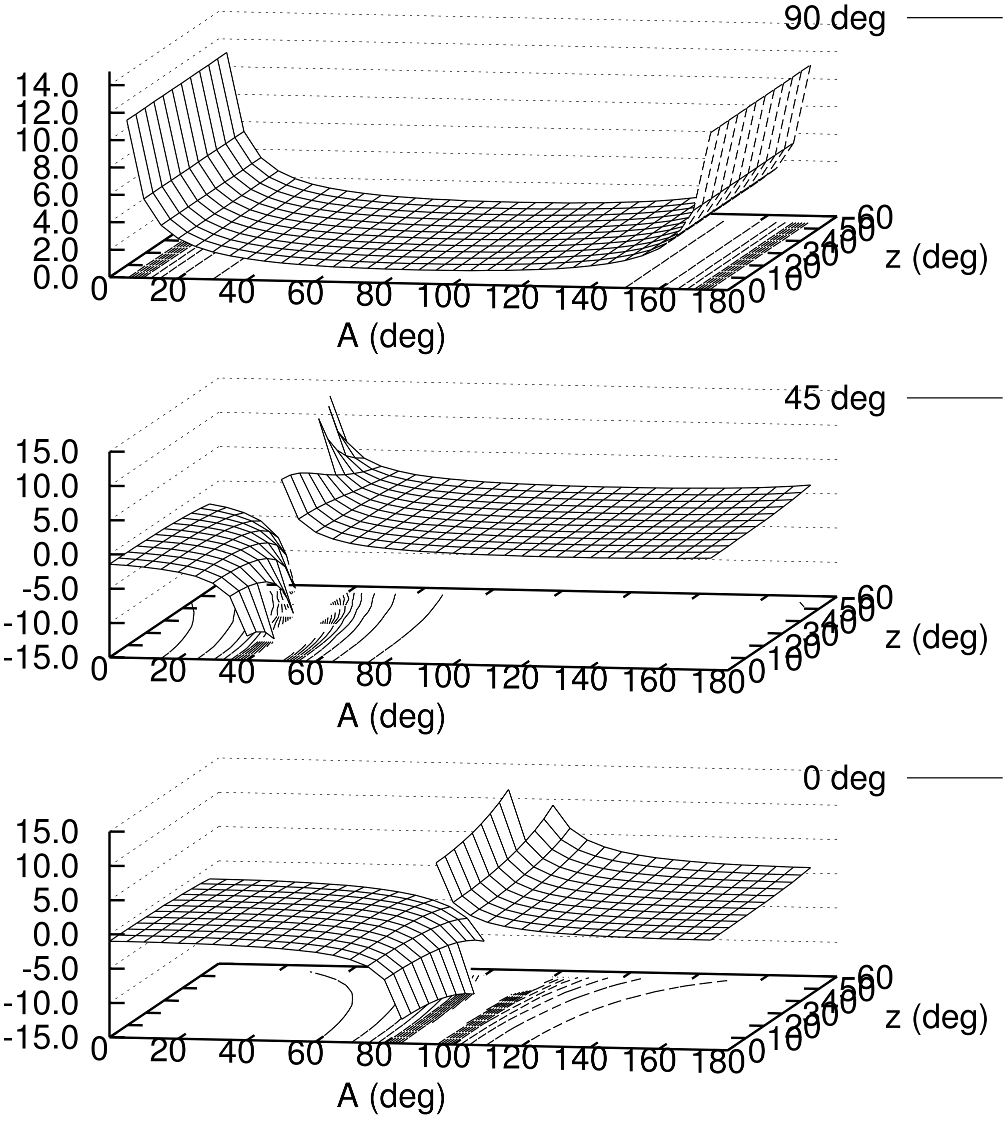

Figure 44: The factor $1/(\sin\bar{A}\sin\varphi - \cos\bar{A}\cos\bar{z}\cos\varphi)$ in Eq. (59) for three co-zeniths φ of the secondary star between 0 and 90 deg. The denominator is some cosine of an angle in a spherical triangle, Eq. (43), and stays in the range [-1:1].

To turn the argument around, Fig. 47 shows the error allowed in the differential OPD by (59) supposed to reach an error in τ of 10 μas at a 100 m baseline. Doubling the baseline or doubling the error in τ would each double the margin on the DOPD.

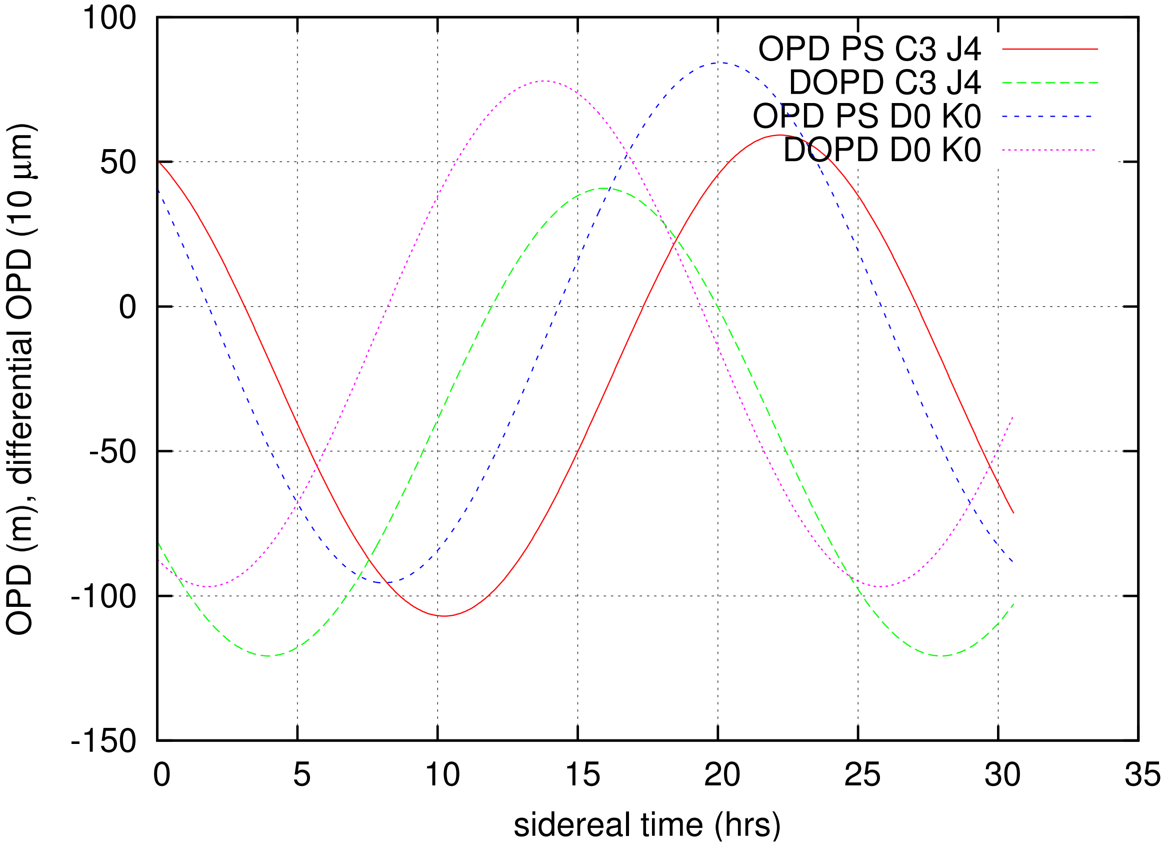

Figure 45: The OPD D and differential OPD ΔD for two stars, separated $2''$ in RA and $0.7''$ in DEC, seen from two baselines b that connect either station C3 with station J4 ($b = 147$ m) or D0 with K0 ($b = 96$ m), as if observed through one day and one night. A zenith limitation to 60° makes the delays > 127m for the 147 m and the delays > 83m for the 96 m baseline unreachable. See Sect. D.2 for the determination of b from measurements of D, and Sect. D.3 for the parameters of $\Delta D(t)$.

28.3.3 Global Star Position Errors

The previous chapter related the error $\epsilon(\tau)$ in the astrometric angle to the error $\epsilon(\Delta D/b)$. In the same manner, Eq. (59) demonstrates how the geometry of (i) the mean position of the pair of stars relative to the baseline and (ii) of the direction from the PS to the SS relate to the error $\epsilon(\tau)$. If $\epsilon(\bar{A})$ denotes the absolute error in the mean azimuth, and $\epsilon(\bar{z})$ the absolute error in the mean zenith angle (units are radian), lowest order error propagation yields a relative error

$$\frac{\epsilon(\tau)}{|\tau|} = \left|\frac{\cos\bar{A}\sin\varphi + \sin\bar{A}\cos\bar{z}\cos\varphi}{\sin\bar{A}\sin\varphi - \cos\bar{A}\cos\bar{z}\cos\varphi}\right|\epsilon(\bar{A}) + \left|\frac{\cos\bar{A}\sin\bar{z}\cos\varphi}{\sin\bar{A}\sin\varphi - \cos\bar{A}\cos\bar{z}\cos\varphi}\right|\epsilon(\bar{z}). \qquad (44)$$

The factor shown in Fig. 44 again "boosts" any error $\epsilon(\bar{A})$ or $\epsilon(\bar{z})$ that would typically be inherited from star catalogues. For illustration, we again assume three different orientations φ of the pair of stars on the sky at the time of observation; we plot the relative error $\epsilon(\tau)/|\tau|$ produced by an error of 0.1 arcsec in either $\bar{A}$ or $\bar{z}$ in Fig. 48. In summary, an error of 0.1 arcsec in the knowledge of the star positions produces a relative error in the astrometric angle of the order of 10^{-7} to 10^{-5}. Because $\tau \le 2$ arcmin, this is an absolute error in $\epsilon(\tau)$ less than 10 μas to 1 mas.

The argumentation is actually dealing with the *relative* positioning error between the stars **s** and the baseline **b**: the direction of the baseline vector must also basically be known to $\approx 0.1'' = 4.8 \cdot 10^{-7}$ rad, which is an accuracy of 48 μm per 100 m baseline. (The term does not surface explicitly because the direction was fixed in (59) to simplify the notation.) Better a priori knowledge on the single source positions is not necessarily useful given the PSF of $0.3''$ of an AT in the K-band, and the pointing accuracy of $\approx 0.15''$ [141].

This is a rather generic astrometric conclusion: Measurement of an angle τ for a well-resolved object means we may set the cosine in the combined (59) and (43) to 1,

$$\tau = -\frac{\Delta D}{b\cos(\varphi + \xi)} \longrightarrow \tau = -\frac{\Delta D}{b}. \tag{45}$$

With the interferometric altitude a shown in Fig. 51, $D = b\cos a$, this becomes

$$\tau = -\Delta(\cos a) = \sin a\,\Delta a, \tag{46}$$

with an error term

$$\epsilon(\tau) = \epsilon(\sin a)\,\Delta a = \cos a\,\epsilon(a)\,\Delta a. \tag{47}$$

The factor Δa would be limited by anisoplanatism to typically 40 arcsec $= 2 \cdot 10^{-4}$ rad [33], and $\cos a$ of the order 1/2; therefore the global positioning error $\epsilon(a)$ contributes to the astrometric error $\epsilon(\tau)$ typically multiplied by a factor of 10^{-4}, translating $\epsilon(a) = 0.1''$ into $\epsilon(\tau) = 10\mu$as. The hard limits set for the PRIMA differential FOV are $\Delta a < 2$ arcmin and for the AT pointing $a > 30°$, combined $\cos a\,\Delta a < 5 \cdot 10^{-4}$ rad, translating $\epsilon(a) = 0.1''$ into $\epsilon(\tau) = 50\mu$as.

The strategy to keep this fundamental geometric error low is the same as in Sect. 28.3.2: to avoid observing close to that time of the night where the orientation vector between the two stars is perpendicular to the baseline, ie, where the PS and SS are on the same "rainbow" half circle around the baseline vector, illustrated in Fig. 43. For baselines aligned in polar directions, though, this scheduling option looses its grip since this type of angular co-alignment of the pair's vector would barely change during a night. The other obvious advice is to obtain the global star positions accurately enough to make this error, which is proportional to these accuracies, negligible.

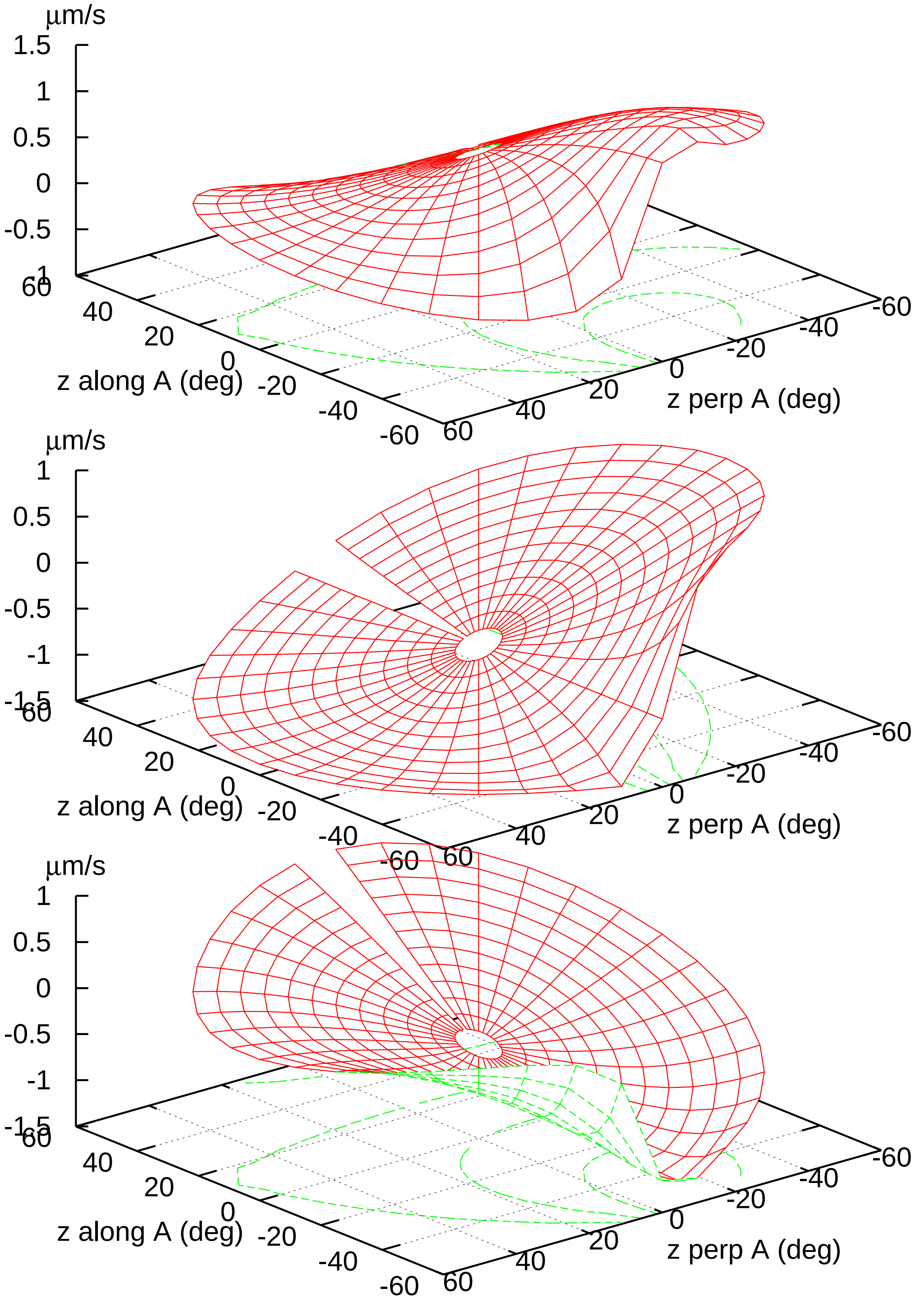

Figure 46: Complementary to Fig. 45, these are examples of velocities of the differential OPD, $\partial \Delta D/\partial t$, for the U1–U3 baseline measurement on midnight of 2006-08-31 with a star separation of $1'$. The top figure is for a position angle of $p_{\mathrm{SS}} = 0°$, the middle figure for $p_{\mathrm{SS}} = 90°$ and the bottom figure for $p_{\mathrm{SS}} = 180°$. The base of each figure is a flat projection of the Celestial Sphere; the middle of each plot is the value if the star pair is at the zenith; concentric circles around the center describe positions further away up to a maximum zenith angle of 60°; the radial directions are rays of constant azimuth.

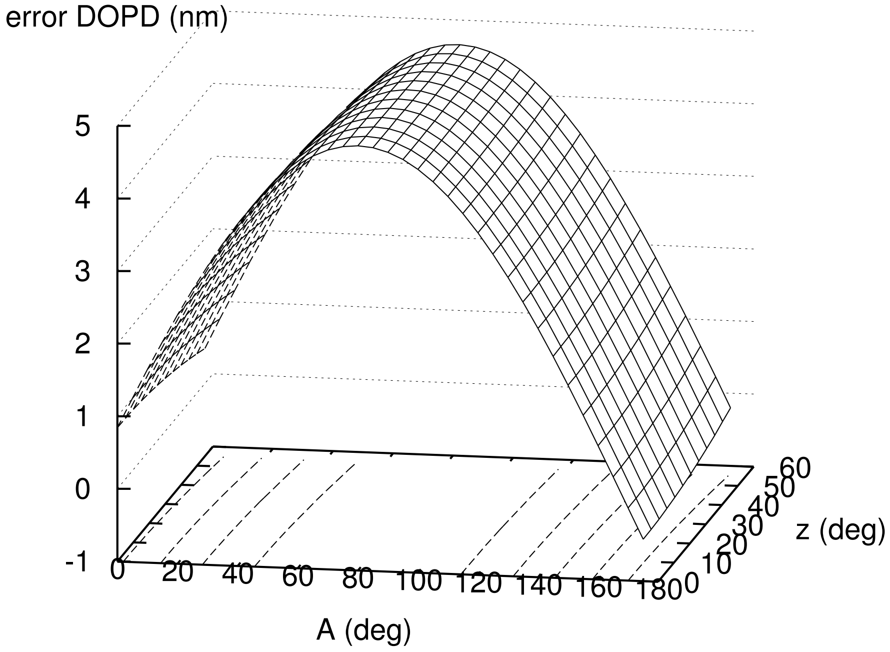

Figure 47: The (signed) error in ΔD linked to an error of 10 μas in τ according to Eq. (59) at $b = 100$ m for varying alt-az positions on the sky at an angle of $\varphi = 30$ deg between the two stars.

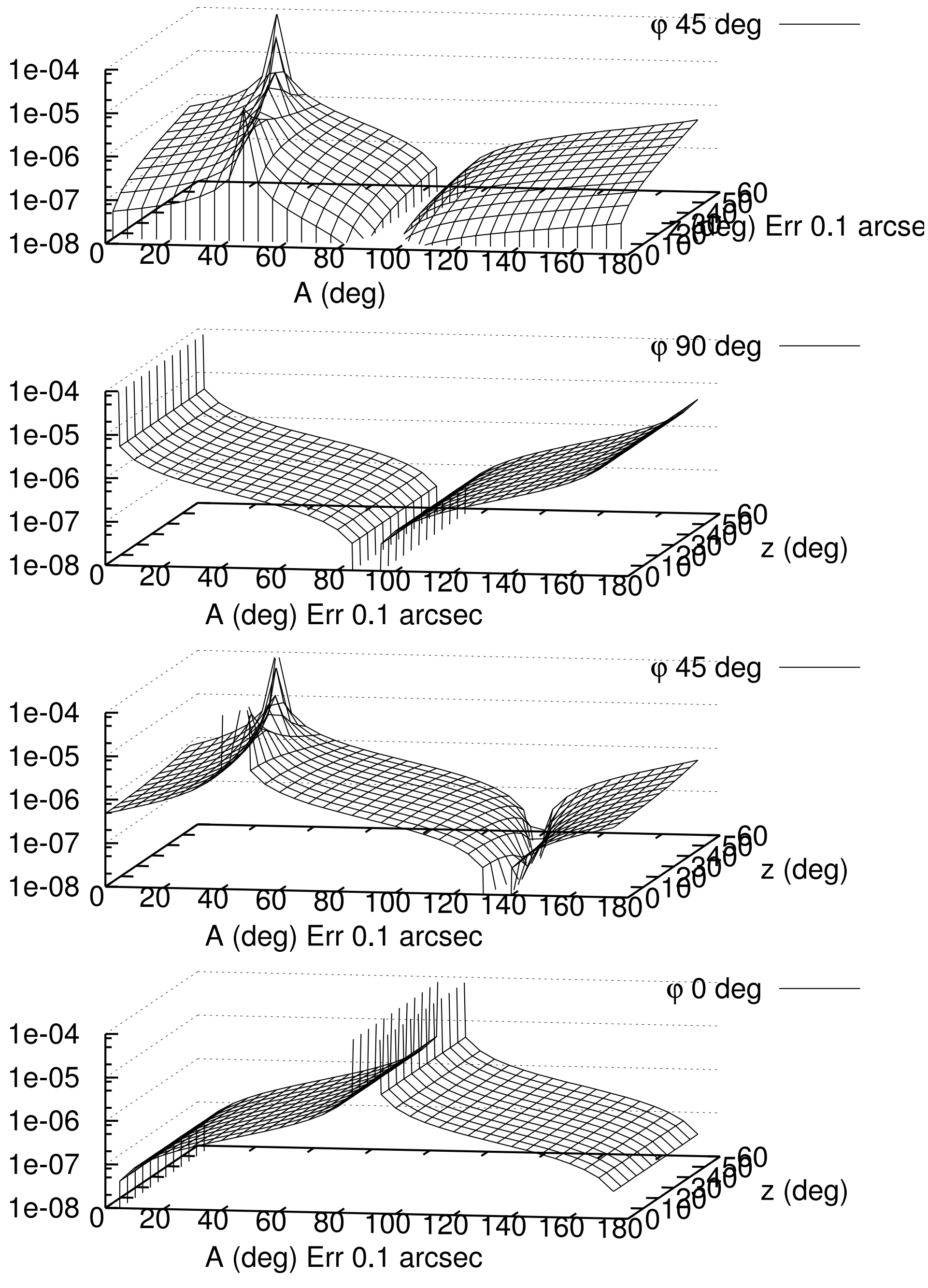

Figure 48: The relative error $\epsilon(\tau)/|\tau|$ of the astrometric angle as a function of mean azimuth $\bar{A}$ and mean zenith $\bar{z}$ for three different orientation angles φ of the star pair, acc. to (44). The uppermost plot assumes an error of $\epsilon(\bar{z}) = 0.1$ arcsec and no error in $\bar{A}$, the lower three plots assume an error of $\epsilon(\bar{A}) = 0.1$ arcsec and no error in $\bar{z}$.

28.3.4 Numerical Simulator

More thorough numerical examples can be computed by the Java applet we provide in the `prErrWeb.html` link of the URL `http://www.strw.leidenuniv.nl/~mathar/vlti/`; this takes into account the correlations between OPD and baseline errors, allows to introduce errors in both degrees of freedom (τ and φ) of the reduction, etc (Fig. 49).

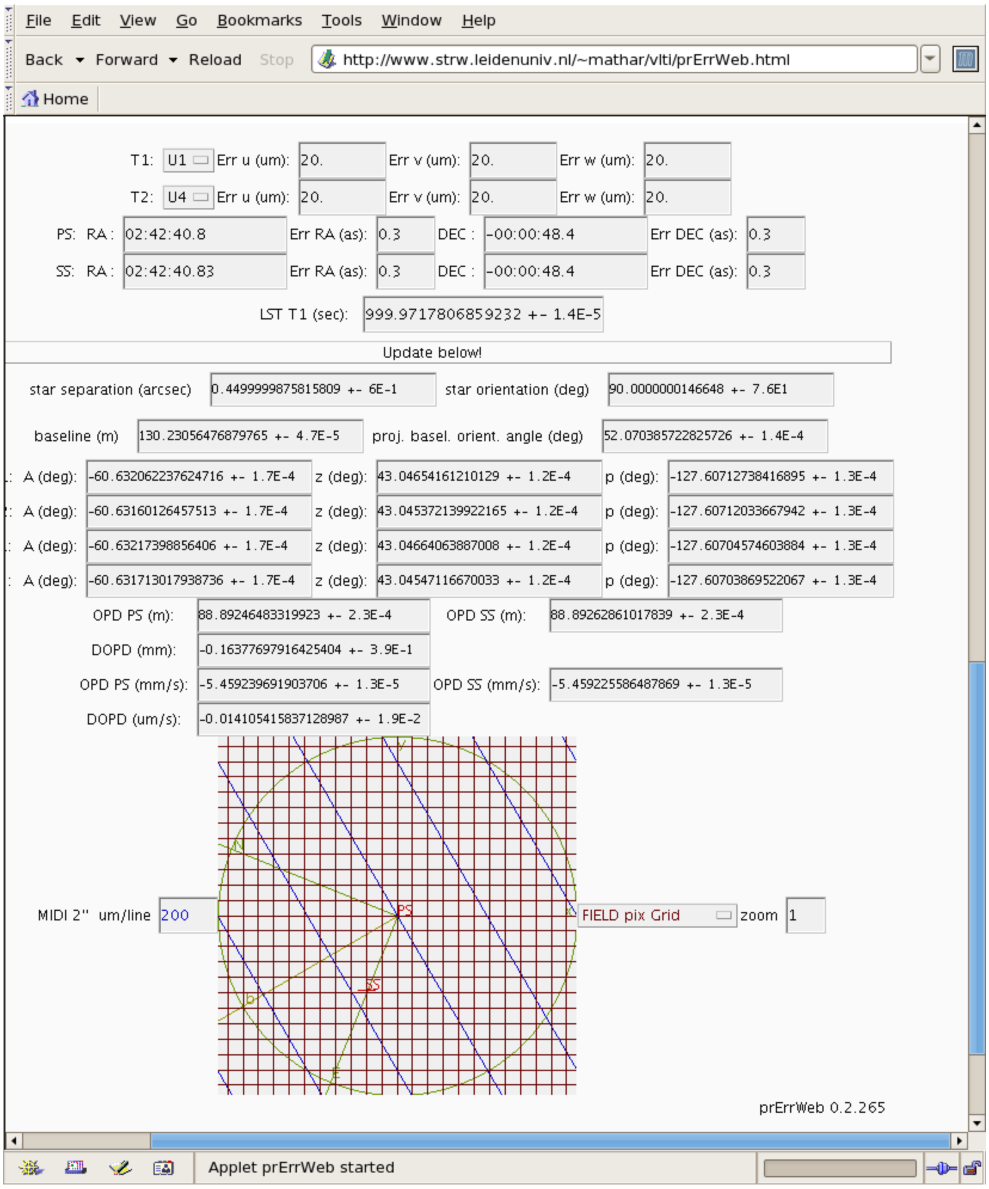

http://www.strw.leidenuniv.nl/~mathar/vlti/prErrWeb.html

T1: U1 Err u (um): 20. Err v (um): 20. Err w (um): 20.
T2: U4 Err u (um): 20. Err v (um): 20. Err w (um): 20.
PS: RA : 02:42:40.8 Err RA (as): 0.3 DEC : -00:00:48.4 Err DEC (as): 0.3
SS: RA : 02:42:40.83 Err RA (as): 0.3 DEC : -00:00:48.4 Err DEC (as): 0.3
LST T1 (sec): 999.9717806859232 +- 1.4E-5

star separation (arcsec) 0.4499999875815809 +- 6E-1 star orientation (deg) 90.0000000146648 +- 7.6E1
baseline (m) 130.23056476879765 +- 4.7E-5 proj. basel. orient. angle (deg) 52.070385722825726 +- 1.4E-4
A (deg): -60.632062237624716 +- 1.7E-4 z (deg): 43.04654161210129 +- 1.2E-4 p (deg): -127.60712738416895 +- 1.3E-4
A (deg): -60.63160126457513 +- 1.7E-4 z (deg): 43.045372139922165 +- 1.2E-4 p (deg): -127.60712033667942 +- 1.3E-4
A (deg): -60.63217398856406 +- 1.7E-4 z (deg): 43.04664063887008 +- 1.2E-4 p (deg): -127.60704574603884 +- 1.3E-4
A (deg): -60.631713017938736 +- 1.7E-4 z (deg): 43.04547116670033 +- 1.2E-4 p (deg): -127.60703869522067 +- 1.3E-4
OPD PS (m): 88.89246483319923 +- 2.3E-4 OPD SS (m): 88.89262861017839 +- 2.3E-4
DOPD (mm): -0.16377697916425404 +- 3.9E-1
OPD PS (mm/s): -5.459239691903706 +- 1.3E-5 OPD SS (mm/s): -5.459225586487869 +- 1.3E-5
DOPD (um/s): -0.014105415837128987 +- 1.9E-2
MIDI 2" um/line 200
zoom 1

prErrWeb 0.2.265

Applet prErrWeb started

Figure 49: `prErrWeb.html` converts errors in station coordinates and star positions into errors of local sky coordinates and optical path differences.

ΔD can be rewritten in terms of $\Delta\delta$ and Δh of the star coordinates as in [130, §2.3].

28.3.5 Tangential Approximation

The expansion of (54) in Δz and ΔA reads

$$C \equiv \cos\tau - 1 = -\frac{1}{2}\left[(\Delta z)^2 + \sin^2\bar{z}(\Delta A)^2\right] + \frac{1}{24}\left[(\Delta z)^4 + 3(\Delta z)^2(\Delta A)^2 + \sin^2\bar{z}(\Delta A)^4\right] + \cdots \quad (48)$$

The inversion of the power series of the cosine

$$C = -\frac{1}{2}\tau^2 + \frac{1}{24}\tau^4 - \frac{1}{6!}\tau^6 + \cdots \quad (49)$$

yields [1, 3.6.25]

$$\tau^2 = -2C + \frac{1}{3}C^2 - \frac{4}{45}C^3 + \frac{1}{35}C^4 + \ldots \quad (50)$$

Insertion of C from above yields the terms in (56) up to mixed 4th order in Δz and ΔA:

$$\tau^2 = (\Delta z)^2 + \sin^2\bar{z}(\Delta A)^2 - \frac{1 + 2\cos^2\bar{z}}{12}(\Delta z)^2(\Delta A)^2 - \frac{1}{12}\cos^2\bar{z}\sin^2\bar{z}(\Delta A)^4 + \cdots \quad (51)$$

Δz and ΔA are limited to the PRIMA FOV of $2'$, which means the relative change in τ^2 introduced by the two 4th order terms is limited to roughly a fourth of $(\Delta z)^2, (\Delta A)^2 < 3.4 \cdot 10^{-7}$ rad^2. The relative correction in τ is limited to half of this, $4 \cdot 10^{-8}$ rad. Since τ is also less than $2' = 120''$, the absolute contribution of the 4th order terms to τ is never larger than 5 μas. In this sense, Equation (58) does not suffer from distortions as it ignores wrapping effects in the coordinate system.

The equivalent extension of (57) to mixed third order is

$$\begin{aligned}\frac{\Delta D}{b} \approx\ & \sin\bar{A}\sin\bar{z}\Delta A - \cos\bar{A}\cos\bar{z}\Delta z \\ & + \frac{1}{24}\cos\bar{A}\cos\bar{z}(\Delta z)^3 - \frac{1}{8}\sin\bar{A}\sin\bar{z}(\Delta z)^2\Delta A - \frac{1}{24}\sin\bar{A}\sin\bar{z}(\Delta A)^3 + \frac{1}{8}\cos\bar{A}\cos\bar{z}\Delta z(\Delta A)^2\end{aligned}$$

Taking into account the coefficients, the relative change by the third order terms is limited to a sixth of $(\Delta z)^2, (\Delta A)^2 < 3.4 \cdot 10^{-7}$. This correction obviously is of the same order as the relative correction to τ, since both parameters are tightly linked by Equation (59).

28.4 Impact on astrometry

The sidereal motion of the two stars limits the time over which one can naïvely calculate the DOPD as a simple mean over an observation period, for example during a data compression step in the DRS. The DOPD is a sinusoidal function of time as shown in Fig. 45. The maximum amplitude X_m is 0.117 m if the longest baseline $b = 202$ m is used at the maximum star separation $\tau = 2'$. (The longest baseline admitted in [64] is 145 m.) Assigning the mean OPD to the middle of an observation period is exact for strictly linear motion in t, $\Delta D(t) = \Delta D(t_0) + \frac{\partial \Delta D(t)}{\partial t}(t - t_0)$. The DOPD velocity may reach up to $\partial\Delta D(t)/\partial t \leq X_m\omega_L \approx 8.5$ μm/s, where $\omega_L = 2\pi/(24 \cdot 3600)$ 1/s$\approx 7.3 \cdot 10^{-5}$ 1/s is the angular velocity. The error results from higher order derivatives, here the second order derivative $\partial^2\Delta D(t)/\partial t^2 \leq X_m\omega_L^2$. In such 2nd order approximation, the difference between the true mean (the integral over the interval divided by the length of the interval) and the actual value in the middle of the interval is the second derivative times the squared length of the interval divided by 24:

$$\epsilon(\Delta D) = \frac{1}{24}X_m\omega_L^2\bar{t}^2. \quad (52)$$

The average should therefore not be done on time intervals longer than $\bar{t} = \sqrt{24\,\epsilon(\Delta D)/X_m}/\omega_L$, which is 14 s if $\epsilon(\Delta D) = 5$ nm. This requirement becomes more relaxed when either X_m becomes smaller because the two stars are closer than the $2'$ maximum, or when the phase of the diurnal motion at the time of the averaging is known, for example.

In the same spirit, the time $\bar{t}$ should not exceed 35 s if the non-linearity error of the estimation of the main delay is to be kept smaller than 40 μm. This result is obtained by insertion of $\epsilon = 40 \cdot 10^{-6}$ m and a diurnal amplitude of $X_m = 150$ m into the same formula.

Differential proper motions have obviously been left aside here.

29 CLOCKS

29.1 Introduction

The need for clock accuracy differs according to the data reduction model adopted in synthesizing the subsystems' information to the star separation.

29.2 Data Reduction Fundamentals

29.2.1 Concurrent Interferometer Model

In the concurrent interferometer model, a data unit is the ABCD channel information of the two FSUs, a sequence of (spectrally dispersed) concurrent read-outs of the two detector control software "instances" with independent time stamps. These two clocks are implicitly synchronized by a master GPS system and have a specified accuracy of 9 μs [150, 151]. Timer interrupt latency and software overhead introduce a jitter on 400 MHz CPUs of the order of 30 μs [45, 113, 114] which enters the `TIME` columns of the FITS files, maybe worse. Although running a readout pattern by activating a program in static RAM achieves a much better uniformity in the readout cycles on the 100 ns time scale on the timer boards of a ROE, the time bias between the two sequences remains on the 30 μs time scale, limited by the way of implicit synchronization of the start. Whether 10 μs can be achieved depends on the LCU schedules (activity according to network, data transfer, interrupt frequencies,...). The clock will appear retarded on the LCU with the higher load.

Attempts to tie the local time basis tighter to atomic clocks would be not of much use since the intrinsic clocking "speed" of the Earth rotation axis is generally also not known better than 10 μs (Fig. 50).

The fundamental data reduction scenario in this model is that both ABCD patterns are independently reduced to delays D—roughly demonstrated in Section 6.3 in [120]—, and then subtracted at a common point on the time axis; PRIMET and DDL data are ignored. Since the diurnal motion is equivalent to 360° in 24 hours or 15 μarcsec in 1 μs, a drift of the order of 10–20 μs between both LCU clocks limits the accuracy of the separation determination (in α) to 150–300 μarcsec, as both stars are "assigned" to their LCUs.

29.2.2 VLBI Model

In the VLBI model, the fundamental datum generated by the instrument is a time sequence of PRIMET readouts. Based on some generic trust in that the MDL and DDL positions are faithfully adjusting their optical path differences with a "good" fringe tracker, the PRIMET DOPD is a sinusoidal function of 24 hour period as the one shown in Fig. 45. A fit to this reveals the product of the equatorial and polar components of the baseline and the star separation in the fitted amplitude and zero-offset, see Section D.3.2. Given the baseline vector, no dependence is left on the accuracy of the PRIMET clock. [The diurnal fit with amplitude, offset and phase would ignore its phase output, which can be interpreted as a measure of the absolute clock or knowledge of the telescope's geographical longitude— in 10 μs the baseline moves 5 mm to the East, see Eq. (85).]

The clock bias problem explained in Section 29.2 has disappeared because PRIMET has taken a snapshot at one point in time. We note that this is a *model* as the following points are deliberately kept aside: (i) The predictable dropouts of the observations mean that the fit deteriorates gradually

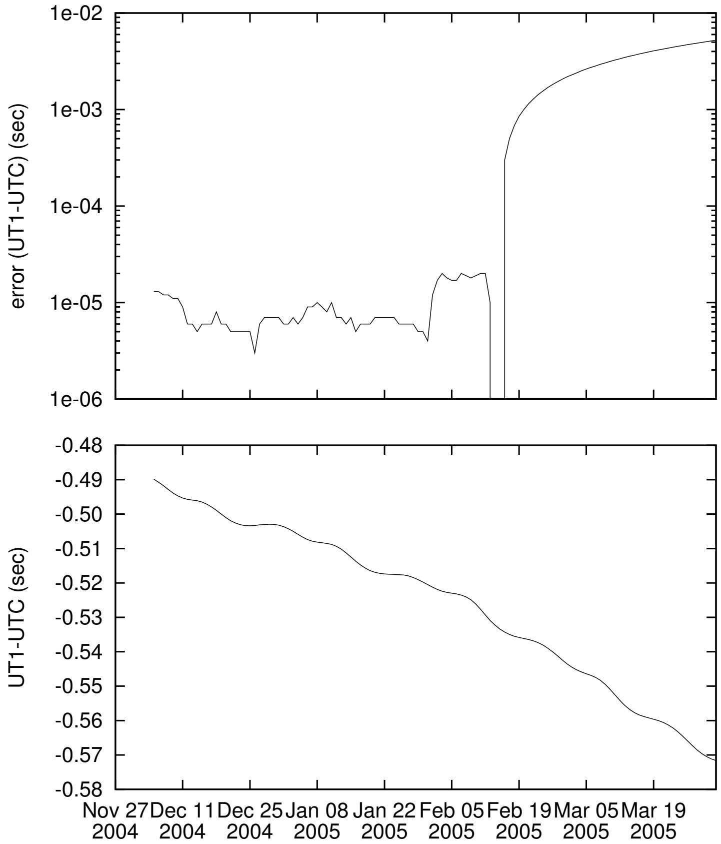

Figure 50: The time difference between UT1 and UTC—past and predictions—and their estimated errors published by Bulletin A of the IERS on Feb 14, 2005.

as less and less observation time covers pieces of one or more 24 hour periods of ΔD. (ii) Due to non-stationarity of the Earth axis (App. C), lensing effects as cited in Section 26.1, etc., the data reduction cannot use strictly sinusoidal fits to the ΔD. (iii) The PRIMET light needs 0.3 μs to move each 100 m of delay, which translates into an equivalent fuzziness of its "absolute" clock. The relevant analysis for the astrometry with super-heterodyne methodology for the phase meter is the time needed to travel the *differential* OPD of up to 0.12 m; this obviously becomes negligible compared to the requirement of knowing the difference between the two beam's clocks to 0.67 μs for 10 μarcsec accuracy in $\Delta\alpha$.

29.3 Baseline Calibration

As noted above in Section 29.2.2, the application to the science case needs two of the three components of the baseline vector to allow separation of the two components of the star separation vector; if the orientation of the star separation is known by other means, this reduces even further to the knowledge of the vector length, Eq. (59). There is no indication that the baseline calibration needs to determine the full time-dependent 6-component vector mentioned in [152, Sec. 4.1]. The reduction of the baseline calibration to the two components does not depend on the offset of the MDL clock from some "global" clock; in particular, the aim to know the calibrator stars to better than $\approx 0.2''$—Section D.5— does *not* demand an absolute synchronization of the MDL clocks on some sub-second timescale. However, to provide an effective resolution for each individual star visited during the calibration to $\approx 0.2''$ with the aim to keep the number of stars low in the sense of Fig. 53, the clock axis during the baseline calibration should stay linear on the 10 ms scale according to the standard scale factor of $15''/s$.

29.4 Impact on astrometry

The actual data reduction uses a hybrid of both approaches, since the PRIMET DOPD merely is a representation of some mirror locations, with no strict binding to the fringe phases reported by the two FSUs. The interpretation of the mirror positions depends on the fringe tracker methodology (phase tracking, group delay tracking,... see for example the discussion in [124]), and any attempt to re-interpret the ABCD phases in terms of models of the refractive indices in the tunnel also involves finding the two detector frames (by interpolation) that are valid at the clock reported by PRIMET (ie, re-alignment of the three clocks). The fringes are virtually "frozen" as seen by the ABCD values due to the tracker's activity, so the bias pointed out in Section 29.2 does not exist to first order.

The residual effects follow from the two corrections of the PRIMET values M pointed out in (25) and from adjustment according to the phase differences reported by the FSUs:

- The time drift in the star color difference term $D\left(n_{\lambda_{ses}} - n_{\lambda_{ps}}\right)$ during a period Δt in time becomes $\Delta t \frac{\partial D}{\partial t}\left(n_{\lambda_{ses}} - n_{\lambda_{ps}}\right)$. As in Section 9.3 we assume that the difference in the refractive indices is not larger than $9 \cdot 10^{-10}$ for any difference in the star colors. Similar to the calculation in Section 28.4, the OPD velocity is limited to $\partial D/\partial t < 0.012$ m/s since OPD amplitudes are limited to 170 m. This keeps the product $\frac{\partial D}{\partial t}\left(n_{\lambda_{ses}} - n_{\lambda_{ps}}\right)$ smaller than $1.1 \cdot 10^{-11}$ m/s. The time drift in this term is less than 1 nm in 100 s, so this accuracy in the timing becomes not a concern.

- The time drift in the reduction of the PRIMET wavelength to the K band, $M\left(n_{\lambda_{ses}} - n_{\lambda_m}\right)$, follows in the same manner from the maximum sidereal motion $\partial M/\partial t < 8.5$ μm/s (Section 28.4) and a difference in the refractive indices between the two bands. It is simply obtained by multiplying the value in Table 7 of [119] by ω_L of Section 28.4, some pm/s, and therefore even less a concern.

- A scholar example of the adjustment of the PRIMET records following from the phase differences of the FSUs is the case where the FSU tracking the MDL is a phase tracker on the nodes of the fringe to minimize fringe jumps, whereas the DDL would be tracking on some maximum, $\varphi = 0$. This would need a systematic counter-rotation of the PRIMET values by a quarter of a fringe, roughly 500 nm. (It is exactly for this a posteriori analysis with Eq. (6) of [120] that the `IMAGING_DATA` tables [185] will be used.) In this case, the correction involves no time-dependence at all. In another example one might think of adjusting the PRIMET data by subtracting jitters in the observed phases (as those from the tunnel seeing) explicitly on a frame-by-frame basis. In this case the granularity on the time axis is set by the detector integration times of the order of 1 ms or more. However the corrections appear as noise of zero mean; they also have no potency to introduce a systematic bias in these apparent two subsystem's clocks.

A slower effective control on a LCU steers the DDL such that the differential delay reported by PRIMET refers to a time associated with earlier ABCD values. If the PRIMET absolute clock is not used using some VLBI data reduction model in the sense introduced above, this does not harm, because this control loop lag is absorbed in the phase (time axis offset) of the diurnal motion of the DOPD.

30 SOLAR SYSTEM EFFECTS

30.1 Introduction

The velocity of Paranal must be taken into account when performing astrometric observations with PRIMA. Existing Solar System models will be adequate for this. Major planets in the Solar System may impact the observations if targets are selected which are close to these planets on the sky [171, 3.1.3].

30.2 Dependencies

30.2.1 Error terms effected by this

Error term	Relevant subsection

The date and time of the observations determines:

1. The position of the Earth
2. The velocity of the Earth
3. The position of the Sun
4. The position of Jupiter
5. The position of Saturn

30.3 Detailed contributions

This contribution results from relativistic effects within the Solar System. These relativistic effects on angles are due to the velocity of Earth, and gravitational effects due to the influence of the largest masses in the Solar System [57].

30.3.1 Velocity of Paranal relative to Solar System centre

Special relativistic effect

30.3.2 Gravitational effect of Sun

General relativistic effect

30.3.3 Gravitational effect of Jupiter

General relativistic effect

30.3.4 Gravitational effect of Saturn

General relativistic effect

31 GALACTIC EFFECTS

31.1 Introduction

Motions of the PS and SS can introduce complex differential astrometry signals. The effects of perspective acceleration and the Corriolis effect (if multiple SS are used with one PS) will have to be studied in detail.

31.2 Dependencies

31.3 Detailed contributions

The galactic effects can be broken down into several contributions to the astrometric error:

1. Perspective acceleration due to proper motion of stars
2. Corriolis effect for rotating frame of reference for those targets with two reference stars

31.3.1 Perspective acceleration due to proper motion of stars

Any object having a component of its velocity in the plane of the sky will appear to accelerate or decelerate as the angle towards the object changes [10].

31.3.2 Corriolis effect for rotating frame of reference

This effect only applies when there are two or more reference stars around a target. These two stars define a coordinate frame which will rotate with time, producing an apparent acceleration of the target.

32 TOTAL ASTROMETRIC ERROR

32.1 Introduction

In this section it will be necessary to combine the effects from all the other error terms in this document, and look for inter-dependencies between different error terms.

32.2 Dependencies

The fundamental error calculation for the angular separation τ between two stars at direction vectors $\mathbf{s}_1$ and $\mathbf{s}_2$ is summarized follows: let a baseline vector $\mathbf{b}$ be given that at the same time specifies the x-coordinate of a Cartesian coordinate system. The zenith angles z_i and azimuth angles A_i of the two stars could be defined relative to the baseline vector:

$$\mathbf{s}_i = \begin{pmatrix} \cos A_i \sin z_i \\ \sin A_i \sin z_i \\ \cos z_i \end{pmatrix}; \qquad \mathbf{b} = \begin{pmatrix} b \\ 0 \\ 0 \end{pmatrix}. \tag{53}$$

The star separation becomes

$$\cos\tau = \mathbf{s}_1 \cdot \mathbf{s}_2 = \sin z_1 \sin z_2 \cos(A_1 - A_2) + \cos z_1 \cos z_2, \tag{54}$$

which for small separations Δz and ΔA

$$z_1 \equiv \bar{z} - \Delta z/2;\ z_2 \equiv \bar{z} + \Delta z/2;\ A_1 \equiv \bar{A} - \Delta A/2;\ A_2 \equiv \bar{A} + \Delta A/2; \tag{55}$$

is to lowest order in Δz and ΔA (see Section 28.3.5)

$$\tau^2 = (\Delta z)^2 + \sin^2 \bar{z} (\Delta A)^2 + \cdots \tag{56}$$

The two OPD's are $\mathbf{s}_1 \cdot \mathbf{b} = b \cos A_1 \sin z_1$ and $\mathbf{s}_2 \cdot \mathbf{b} = b \cos A_2 \sin z_2$, and the ratio of the differential OPD $\Delta D \equiv D_1 - D_2$ over the baseline length b is

$$\frac{\Delta D}{b} = \cos A_1 \sin z_1 - \cos A_2 \sin z_2 \approx \sin \bar{A} \sin \bar{z} \Delta A - \cos \bar{A} \cos \bar{z} \Delta z. \tag{57}$$

Assuming that we know the direction of the SS relative to the PS parametrized by an angle φ [123],

$$\tau \sin\varphi \equiv \sin \bar{z} \Delta A; \qquad \tau \cos\varphi \equiv \Delta z, \tag{58}$$

the angle τ is related to the measured $\Delta D/b$ via

$$\tau = \frac{\Delta D}{b} \frac{1}{\sin \bar{A} \sin\varphi - \cos \bar{A} \cos \bar{z} \cos\varphi}. \tag{59}$$

Fig. 51 visualizes this geometry for a case $\Delta A > 0$ and $\Delta z > 0$: In the spherical right triangle with corners at the PS and the SS, the horizontal base that starts at the SS has a length of $|\Delta A \sin \bar{z}|$, the other cathetus has a length of Δz, and the hypotenuse has a length of τ. φ is the angle at PS between the meridian and the direction to the SS.

As a consequence of (59), observations at times that move the stars to alt-az positions (measured relative to the baseline direction) that are close to the pole of the fraction ought be avoided. This

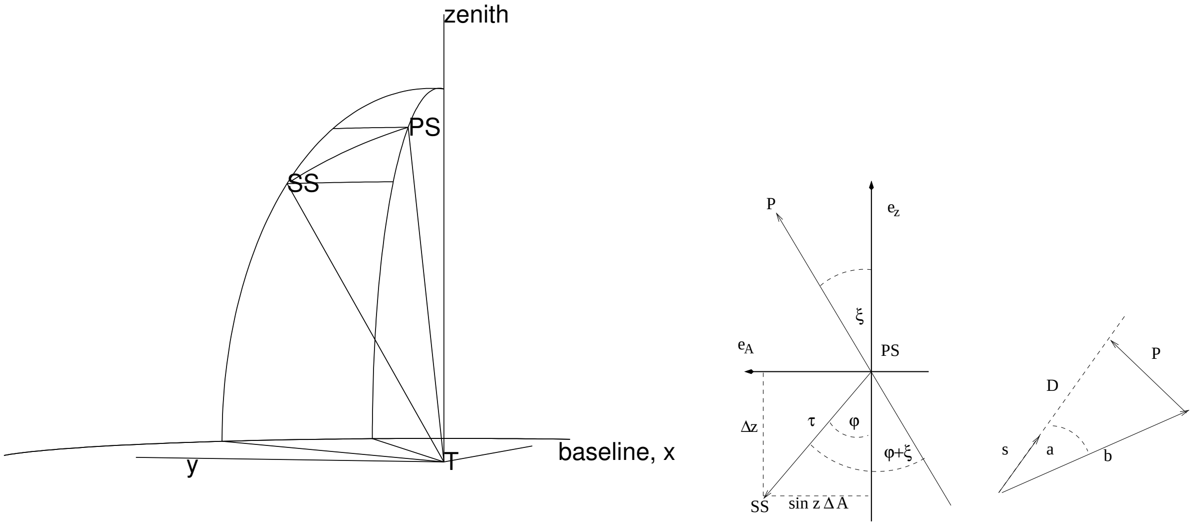

Figure 51: Left: The meridians and zenith angles of the PS and SS define a spherical triangle as seen from the telescope T, related to Eq. (58). Middle: The length of the horizontal section of the arc that starts at SS is $\Delta A \sin \bar{z}$. The distance along the great circle of the Celestial Sphere between PS and SS is τ. The length of the great circle section (meridian) that starts at the PS and ends at the zenith of the SS is $\Delta z = z_2 - z_1$. Right: The projected baseline $\mathbf{P}$ starts at the end of the baseline vector $\mathbf{b}$ and is perpendicular to $\mathbf{s}$.

is detailed in Sec. 28. In more generic, qualitative interferometric terms the argument is that the resolution of a point source at some sky position depends on the projected baseline; for a 2-dish setup used here, good resolution is achieved along the projected baseline vector, and if the distance vector between the pair of stars happens to point orthogonal to this, the interferometric resolution to measure the length of this vector becomes disastrous. For the same reason, the *a priori* knowledge of the global position $(\bar{z}, \bar{A})$ on the sky has one “forgiving” and another “unlucky” component which change during the course of the night.

Another consequence of (59) is a preference for long baselines, caused by the factor $\propto 1/b$. Another, independent request for long baselines stems from a factor $\propto 1/b^{2/3}$ in the statistical error from the turbulent atmosphere [42, 165].

32.2.1 This error term is effected by

Error term	Relevant subsection
Effect of aberrations in image plane optical components	14.3
Effect of aberrations in pupil plane optical components	16.3
Refractive index of air and colour of correlated flux	9.3
VLTI baseline geometry	11.4
Fringe jumps and group tracking errors	27.4
Galactic effects	31.3
Solar System effects	30.3
Systematic effects from the atmosphere	26.3
Image plane optics in the star separator	15.3
Systematic errors in the FSU phase	19.3

32.3 Error Tree

The variables involved can be listed in form of an error tree. Variables on a higher level depend on lists of variables on lower levels that can be recursively split into even more fundamental variables.

In overview, the data reduction computes the terrestrial differential OPD and baseline vector as measured on the earth, corrects both independently for the lensing effects by the earth atmosphere and for the geology of a non-rigid earth crust, optionally builds an intermediate astrometric triangle above the atmosphere, and continues with corrections needed to account for transformations from terrestrial to celestial coordinates.

1 2 3 4 5 6 7 8 9

- Astrometric Angle *The "distance" between the PS and the SS, ie, one component of the separation vector*
  - Astrometric Angle (geocentric) *as measured above the atmosphere*
    - Differential delay *on the ground, stretching between the baseline terminal points*
      - IR metrology *representing the scale which unwinds the OPD positions*
        - raw IR metrology *read by the phase meters*
        - finite aperture *correction according to Sect. 18.1*
        - zero point *to be calibrated by beam swapping*
          - symmetry of derotator swap *quality of the symmetric beam swap*
            - derot STS axis alignment *optical placement after beam rotation by* π
            - FSM pickup precision *ability to pick the same sky position with the other FS*
      - white light phase *the actual delay line positions represented by the fringes*
        - detector readout *quality of representing the fringe (correlated photon) intensity*
          - calibration *knowledge of actual quantum efficiency*
            - linearity
            - bias
        - noise *not originating from the star*
          - detector
            - readout mode
          - photonic *in the sense of Poissonic count statistics*
            - VLTI emissivity
            - sky temperature
            - tunnel temperature
        - signal
          - photonic
            - star magnitude
            - PWV
          - detector
            - efficiency
        - $s-p$ polarization *the ability to calibrate the phasors on the real and imaginary axis*
          - sky *contributions before arrival at the telescope*
            - source
            - atmosphere *polarizing or depolarizing*
          - VLTI train [131]
          - FSU [119]
            - chromatic K-prism
            - absorbing beam combiner
      - Unkerning the chromatic phase *decoupling from the intensity factor, not a deconvolution*
        - 1.3 μm to K-band dispersion *alignment of the 2 scales*
          - static chromatic corrections (glass) *all material passed by metrology and science bea*
            - mismatch K-prism compensator [119]
            - IR dichroic thickness FSU
            - IR dichroic thickness M9

        - DDL vacuum *only if DDL evacuated*
          - mismatch DDL vacuum window
            - static chromatic
            - temperature-dependent chromatic
          - mismatch vacuum dispersion *for counter-correction for the vacuum*
            - Theory 633 nm→2.2 μm *between the DDL metrology and the infra*
            - precision low vacuum *knowledge of the residual gas density*
            - operational overhead DDL metrology data *the software aspect*
        - dynamic chromatic corrections (glass) *due to temperature drifts*
          - mismatch K-prism compensator
        - air dispersion *in the tunnel, ducts*
          - generic molecular *the theory*
            - N_2,O_2, CO_2, Ar *major constituents*
            - H_2O *the variable part*
          - tunnel gradients *gas densities along the beam paths*
            - sensor network coverage
            - 2-color calibration (IR + VLTI DL metrology) *if used for portion inside the DL tunnel*
            - lateral: both IR metrology data *not measured by phase meter, accuracy 1.3 μm*
              - separation from DOPD: swapping *relevant is what survive the beam swap*
          - virials *defining equations-of-state for the gas mixtures*
      - net star temperature *relevant in the tunnels*
        - Star spectrum *above the atmosphere*
        - atmospheric transmission
          - air mass
          - PWV
        - VLTI transmission
          - gradient through mirror hopping *ie, the mirror transmissions are chromat*
          - AT filter wheel *optionally before the STS*
          - M9 transmission *dichroic*
      - on-line tracker software models *including fringe jumps and the online dispersion models*
    - AT off-axis leakage *Sect. 12.3*
      - difference ray optics and elliptical PSF *elliptical aperture for off-axis beams*
      - motions M1-M3 *mirrors rotating with the dome*
        - wind pressure
        - zenith angle
      - motions M4-M10 *nominally fixed*
      - overschooting M9-RR3 *IR metrology dangling path*
  - Baseline (ground)
    - Statistics and Quality of references *wide-angle baseline, frequency and sky coverage*
    - wide-to-narrow angle (M3 to M11) *translation seen in Fig. 27*
    - Earth tide residual *Sect C*
    - slewing: loss of IR metrology *if the calibration slewing out-paces the metrology*
      - Glitches synching with VLTI metr *in case the VLTI DL metrology is used to resume*
  - atmospheric lensing *[118, 119]*
    - scale height (O2,N2,CO2)
    - scale height O3
    - scale height water vapor
    - Ionosphere (F2) *plasma theory beyond the low-dispersive dielectric theory*
    - TAD, ie, star spectrum
    - atmospheric dispersion
- Astrophysical

Reference Frames *including by definition tide effects with periods* > 2 *days*
Astrometric Orientation *Direction angle between PS and SS from the phase in Fig. 45*

In this display, the error tree is equivalent to a top-down view on the DAF [93]. There is no one-to-one correspondence between the reduction steps and the error budget. A list of reasons, which likely is incomplete, is

- A variety of error sources ought become zero-mean, typically scintillation and detector noise. There is no associated recipe to correct these but to accumulate observation time on the sky. Low signal-to-noise ratios [120] must be dealt with on the observation-preparation level, eliminating attempts to observe the unobservable. In the DRS, these noise terms are only represented by output statistics and a design that allows error propagation.
- Error sources that do not follow known trends cannot be corrected. Note the difference between "correction," and "fitting" at this place: One *can* fit trends in pointing up to spherical harmonics up angular momentum quantum number $l = 20$ without having any clue whether the components/residuals relate to air-mass, telescope mechanics/optics or unaccounted terms in the pointing software.
- Some error sources are modeled to the degree that one compute corrections, but will be buried under noise of unknown categories such that corrections on minuscule levels are void.
- Other error sources may have known causes, but are not tractable numerically; there will be no attempt to re-run the Beam Warrior on the VLTI train.
- Some error terms have already been investigated numerically here, with the result that their precise modeling is computationally too expensive to be incorporated in a full-fledged version into pipeline procedures that have time constraints such as being run in the morning. (This does explicitly *not* refer to the efficiency of any compression pipeline.)

A MASTER EQUATIONS

Observables are the instantaneous ABCD values for both stars (written for one spectral channel out of three here), split into a correlated flux written as an integral over the spectrum and an uncorrelated flux with label u. A and C represent the p polarization, B and D the s polarization:

$$\begin{aligned}
A_{\rm PS} &= \int e_{\rm PS}\left\{1+\cos[n_{\rm PS}(k)kD_t - kD_{\rm PS}(k) + \varphi^A_{\rm PS}]dk\right\} + A^u_{\rm PS}, && (60)\\
B_{\rm PS} &= \int e_{\rm PS}\left\{1+\cos[n_{\rm PS}(k)kD_t - kD_{\rm PS}(k) + \frac{\pi}{2} + \varphi^B_{\rm PS}]dk\right\} + B^u_{\rm PS}, && (61)\\
C_{\rm PS} &= \int e_{\rm PS}\left\{1+\cos[n_{\rm PS}(k)kD_t - kD_{\rm PS}(k) + \pi + \varphi^C_{\rm PS}]dk\right\} + C^u_{\rm PS}, && (62)\\
D_{\rm PS} &= \int e_{\rm PS}\left\{1+\cos[n_{\rm PS}(k)kD_t - kD_{\rm PS}(k) + \frac{3\pi}{2} + \varphi^D_{\rm PS}]dk\right\} + D^u_{\rm PS}, && (63)\\
A_{\rm SS} &= \int e_{\rm SS}\left\{1+\cos[n_{\rm SS}(k)k(D_t-l) - kD_{\rm SS}(k) + \varphi^A_{\rm SS}]dk\right\} + A^u_{\rm SS}, && (64)\\
B_{\rm SS} &= \int e_{\rm SS}\left\{1+\cos[n_{\rm SS}(k)k(D_t-l) - kD_{\rm SS}(k) + \frac{\pi}{2} + \varphi^B_{\rm SS}]dk\right\} + B^u_{\rm SS}, && (65)\\
C_{\rm SS} &= \int e_{\rm SS}\left\{1+\cos[n_{\rm SS}(k)k(D_t-l) - kD_{\rm SS}(k) + \pi + \varphi^C_{\rm SS}]dk\right\} + C^u_{\rm SS}, && (66)\\
D_{\rm SS} &= \int e_{\rm SS}\left\{1+\cos[n_{\rm SS}(k)k(D_t-l) - kD_{\rm SS}(k) + \frac{3\pi}{2} + \varphi^D_{\rm SS}]dk\right\} + D^u_{\rm SS}. && (67)
\end{aligned}$$

The notation for the SS differs by an OPD $X \sim 2n(k)l$ set by the DDL; this includes any "leakage" due to differential mirror motion of M1–M10. The integration limits are different for both stars, because the fiber heads, FSU prism and camera lens will be aligned slightly different relative to the detector pixels. The uncorrelated energies are written as different $A^u, \ldots, D^u$ and include detector and background noise, effects of detector efficiency and detector bias. The intensities are products of star spectra, atmospheric transmission, mirror reflectivities, beam combiner conversion coefficients (including the decorrelation factor for PSF overlap), FSU fiber coupling efficiency, and detector quantum efficiency, all chromatic:

$$e_{\rm PS}(k) = e^*_{\rm PS}(k)T^{\rm atm}(k)R(k)C(k)T^{\rm fsu}(k)Q(k). \qquad (68)$$

Polarization effects are taken into account in a lightsome fashion, hidden in the additional phases φ. A better notation might assemble the explicit FSU phase factors and $T^{\rm atm}R$ into Jones matrices. The extraordinary phases contain a differential piston $\varphi^{\rm pst}$ (atmospheric and tunnel combined), the K-prism chromaticities $\varphi^{\rm qpI}(k)$ (Fig. 18 in [119]) and $\varphi^{\rm qpII}(k)$ (Fig. 20 in [119]), a phase lag $\varphi^{\rm bc}(k)$ because the beam combiner layer thickness can match only one wavelength at a time [181]:

$$\begin{aligned}
\varphi^A_{\rm PS} &= \varphi^{\rm qpI} + \varphi^{\rm qpII}, && (69)\\
\varphi^B_{\rm PS} &= \varphi^{\rm qpII}, && (70)\\
\varphi^C_{\rm PS} &= \varphi^{\rm bc} + \varphi^{\rm qpI} + \varphi^{\rm qpII}, && (71)\\
\varphi^D_{\rm PS} &= \varphi^{\rm bc} + \varphi^{\rm qpII}, && (72)\\
\varphi^A_{\rm SS} &= \varphi^{\rm pst} + \varphi^{\rm qpI} + \varphi^{\rm qpII}, && (73)\\
\varphi^B_{\rm SS} &= \varphi^{\rm pst} + \varphi^{\rm qpII}, && (74)\\
\varphi^C_{\rm SS} &= \varphi^{\rm pst} + \varphi^{\rm qpI} + \varphi^{\rm bc} + \varphi^{\rm qpII}, && (75)\\
\varphi^D_{\rm SS} &= \varphi^{\rm pst} + \varphi^{\rm bc} + \varphi^{\rm qpII}. && (76)
\end{aligned}$$

The "internal" metrology PRIMET measures a differential OPD at 1.3 μm,

$$M^{\mathrm{PRI}} = n_{\mathrm{PS}}(J)k(J)D_t - n_{\mathrm{SS}}(J)k(J)(D_t - l). \tag{77}$$

With the current design (a single phase meter), the two terms in this equation are not individually available. Products of indices of refraction and geometric path lengths are to be read as integrals (mean values) over the combined paths through the optics, for the metrology phase as well as in the arguments of the trigonometric functions of the ABCD values:

$$n_{\mathrm{PS,SS}}D_t \sim \int_{\mathrm{T1}} n_{\mathrm{PS,SS}}dx - \int_{\mathrm{T2}} n_{\mathrm{PS,SS}}dx, \text{ etc.} \tag{78}$$

The value of M is the value closest to a difference in some phases of the kernel of the ABCD integrals; dispersion correction in the narrow sense is the art of translating this differential delay from the J- to the K-band.

The delay at arrival at the telescope has been modified by atmospheric lensing as a function of wavelength, zenith angle, baseline and atmospheric composition; above the atmosphere, we assume an achromatic delay D^*_{PS}:

$$D_{\mathrm{PS}}(k) = D^*_{\mathrm{PS}} + D^{\mathrm{atm}}_{\mathrm{PS}}(k, z, b, K). \tag{79}$$

Baseline calibration is a repeated application of Eq. (60). A redundant pair of phases read by the VLTI metrology and PRIMET after fringe acquisition of each star is:

$$M^{\mathrm{PRI}} = n(J)k(J)(D_t + L^{\mathrm{PRI}}); \quad M^{\mathrm{VLTI}} = n(R)k(R)(D_t + L^{\mathrm{VLTI}}). \tag{80}$$

The PRIMA metrology senses changes up to the STS; fake dilations in the ducts or in the VLTI laboratory are detected by correlation of both metrologies. Because this yields lengths between the laser heads and their retro-mirrors, these measurements are producing sets of delays up to some arbitrary constants $L^{\cdots}$; this reduces the number of the calibrator stars visited effectively by one, and enhances sensitivity to drifts in the tunnel climate.

The DDL control loop monitors the differential delay X with a red laser,

$$M_{\mathrm{DDL}} = n(R)k(R)l \xrightarrow{vac} k(R)l. \tag{81}$$

This does not play a role in the astrometric data analysis.

B AIR FLOW THROUGH THE VLTI

B.1 Introduction

We set up a web site plotting ambient and VLTI tunnel humidty and temperature data at `http://www.strw.leidenuniv.nl/~mathar/vlti/` [148] summarized in Sect. 6.1 of [119].

B.2 Dependencies

B.2.1 This error term is effected by

Error term	Relevant subsection
Wind velocity profile	E.3.1
Ground level temperature, humidity and pressure fluctuations	E.3.2

B.2.2 Error terms effected by this

Error term	Relevant subsection
Atmospheric scintillation and thermal background fluctuations	25.3
Internal seeing within the VLTI	23.3

B.3 Detailed contributions

The air exchange pace (chimney effect) resulting from a temperature difference between the inside and the outside can naïvely be calculated as follows: We set the internal energy of n moles of air filling a volume V at pressure p, temperature T and gas constant $R \approx 8.3$ J/mol/K to $pV = nRT$, and equate this to a kinetic energy of $\frac{1}{2}mv^2$. This assumes exchange through a horizontal duct causing no gravitational energy difference, and neglects any losses represented by non-zero Reynolds numbers. Using $m = n\rho_{\text{mol}}$ and $R_{\text{spec}} = R/\rho_{\text{mol}}$, the velocity becomes

$$v = \pm\sqrt{2nR\Delta T/m} = \pm\sqrt{2\Delta T\, R_{\text{spec}}}. \tag{82}$$

The volume exchange rate is

$$\partial V/\partial t = Av = d^2\sqrt{2\Delta T\, R_{\text{spec}}} \tag{83}$$

for ducts of height and width d. The specific R_{spec} for dry air is 287.05 J/kg/T, the AT duct dimension $d = 0.6$ m, and the DL tunnel size $V \approx (119.5 \times 8.6 \times \times 2.3)$ m^3 ≈ 2364 m^3. (The volume of the VLTI laboratory would add ≈ 700 m^3.) We can include the effect of different heights between the inlet and outlet by adding an energy term gmh, where $g \approx 9.8$ m/s^2 is the gravitational acceleration:

$$\frac{1}{2}v^2 + gh + R_{\text{spec}}T = \text{const.} \tag{84}$$

If we count v positive for inward flow, T negative if it is warmer inside, and h positive if the duct ends up higher at the telescope than in the tunnel, this predicts the following duct wind velocities v and times $t = V/(\partial V/\partial t)$ for a full air replacement:

h (m)	ΔT (°C)	v (m/s)	t (min)
0	-1	-23.96	4.6
+0.2	-1	-23.88	4.6
+0.6	-1	-23.71	4.6

We see that these theoretical values are very large—the *measured* velocities for the UT light ducts of $d = 0.7$ m are between 0.5 and 4 m/s, typically 1 m/s [105]—which points at the importance of turbulence to diffuse thermal energy in air. At 1 m/s and $d = 0.6$ m for AT ducts, the Reynolds number is $Re \approx 4 \cdot 10^4$, at an estimated critical threshold of $Re \approx 3 \cdot 10^3$ for the transition from laminar to turbulent flow; a reduction to ≈ 0.1 m/s is needed to get into the laminar regime.

B.3.1 Minimising airflow using windows

The recent dumping of plans to extend MIDI to the Q-band ought have simplified the selection of window materials.

B.3.2 Minimising airflow without using windows

C EARTH ROTATION MODEL

C.1 Introduction

The coordinate definition of the telescope site to celestial coordinates starts from corrections for motions of the earth crust (due to ocean and atmospheric tides [97, 112]), from there to a rigid terrestrial reference frame, and from there to the celestial frame [82].

C.2 Dependencies

C.2.1 Error terms effected by this

Error term	Relevant subsection
VLTI baseline geometry	11.4

C.3 Detailed contributions

One contribution of the definition of the telescope coordinates in a extra-terrestrial coordinate system is given by the influence by the ocean tides that load and release the non-rigid earth crust [170]. According to the `GOt00.2` model provided by Bos and Scherneck [21], the amplitude for the Paranal geographcial coordinates is < 2 cm in vertical and < 0.7 cm in horizontal directions. Strictly speaking, there is no contribution to the astrometric error if the measurement of the baseline vector and the associated differential OPD are made at the same time.

A time lag between these needs correction for this type of slow motion of the baseline direction. The maximum influence on the measurement of an OPD generated by this tidal motion of amplitude $A \approx 1.5$ cm is equivalent to a clocking error of the order of

$$\Delta t = AL/(2\pi\rho\cos\Phi) \tag{85}$$

≈ 36 μs, where $L = 24 \cdot 3600$s is 1 day, and $2\pi\rho\cos\Phi$ the motion of one point of geographical latitude $\Phi = -0.4298$ rad (Paranal) on the surface of the earth sphere of radius $\rho = 6380$ km. Whe can paraphrase this with the help of Fig. 45 into a maximum equivalent baseline *length* error, assuming we happen to measure on one of the steepest parts of the sinusoidal curve $D \sim D_m \sin[t/(24 \cdot 3600\text{s})]$: the amplitude D_m of this curve is limited to $D_m < 202$ m, which is the maximum baseline between B5 and J6—note there is no factor $\sin z$ here—, which limits the baseline error to $D_m\Delta t/L$ or $D_m A/(2\pi\rho\cos\Phi) < 202 \cdot 1.5 \cdot 10^{-2}\text{m}/72.9 \cdot 10^6 \approx 83$ nm. In summary, if the delay between the baseline calibration and the actual astrometric measurement is taken into account on fundamental geometrical grounds, the additonal residual error from neglecting the homogeneous tidal motion of the entire mountain is small compared to the estimated requirement of 50 μm to the baseline accuracy.

For the description of earth nutation and precession [26, 27, 84, 96, 97, 109, 125] we will refer to the IERS Service established under `http://maia.usno.navy.mil/` which publishes the polar motion coordinates on a daily basis (Fig. 52). The obvious importance to PRIMA is in limiting the accuracy of the baseline calibration, Section D.5, in any DRS recipes executed directly after observations, because these can only be founded on predicted rather than consolidated earth rotation parameters.

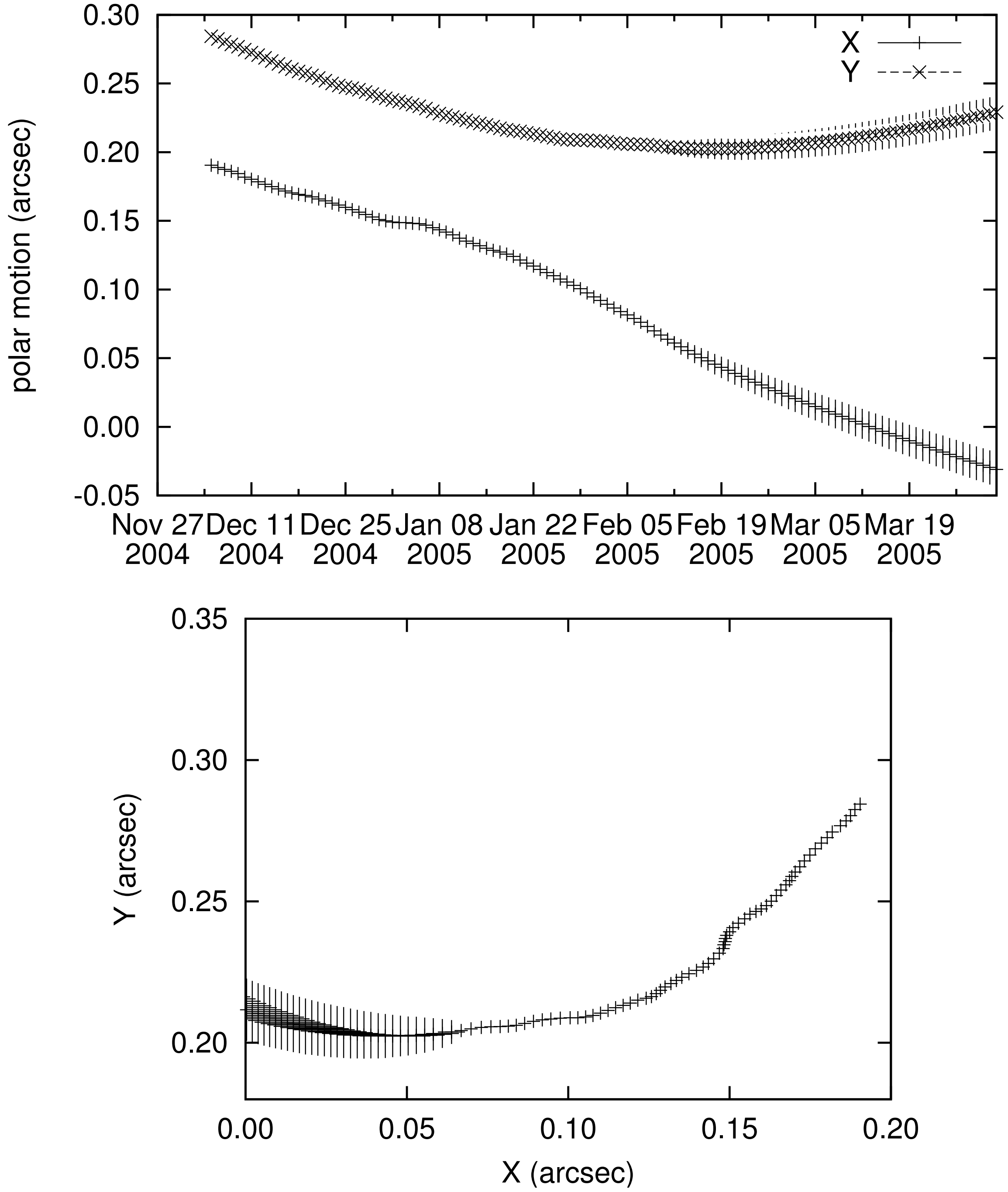

Figure 52: Example of the earth orientation parameters published by the Bulletin A of the IERS on Feb 14, 2005, which includes 90-day predictions. The error lines for data in the past are generally < 100 μas, and are plotted exaggerated [161]. See [56, Fig 2] for a plot showing the wobble over 8 years, and also the figures in [84, §5.].

D POSITION AND SEPARATION OF STARS

D.1 Introduction

One aspect to be mentioned is the potential of baseline length calibration by reverse large-angle astrometry described in the next Section. Supposedly this is well known at ESO for a history of UT baseline calibrations with VINCI; an early statement of intent is found in [106] and a remark in [186] indicates that `IPHASE` [184] is in use.

D.2 Baseline calibration

The baseline length is encoded in the phase and amplitude of the OPD plotted over time (Fig. 45). The basic numerical analysis restarts from Eq. (53) in the more general geometric coordinate system with zenith angle z, azimuth angle A starting at zero in the North direction and turning positive to the West, hour angle h, and declination δ. (The azimuth definition of [147, p 26] may be different.) The baseline directional cosines are $b_{x,y,z}$ with $b_x^2+b_y^2+b_z^2=1$; the baseline terminal point is represented by its geographical latitude Φ. We consider one star only and whence drop the index i.

$$\mathbf{s}=\begin{pmatrix}\cos A\sin z\\ \sin A\sin z\\ \cos z\end{pmatrix}=\begin{pmatrix}\cos\Phi\sin\delta-\sin\Phi\cos\delta\cos h\\ \cos\delta\sin h\\ \sin\Phi\sin\delta+\cos\Phi\cos\delta\cos h\end{pmatrix};\qquad \mathbf{b}=b\begin{pmatrix}b_x\\ b_y\\ b_z\end{pmatrix}. \tag{86}$$

The OPD D is split into an offset $b\sin\delta\cos\Phi_b$ and a sinusoidal function of time $\propto\cos h_b$ [123],

$$D=\mathbf{s}\cdot\mathbf{b}=b(\sin\delta\cos\Phi_b+\cos\delta\cos h_b), \tag{87}$$

where

$$\begin{aligned}\cos\Phi_b &\equiv b_x\cos\Phi+b_z\sin\Phi, &(88)\\ \cos h_b &\equiv -b_x\sin\Phi\cos h+b_y\sin h+b_z\cos\Phi\cos h\\ &= \sqrt{b_y^2+(b_z\cos\Phi-b_x\sin\Phi)^2}\cos(h-h_0)=\sin\Phi_b\cos(h-h_0), &(89)\\ \tan h_0 &= \frac{b_y}{-b_x\sin\Phi+b_z\cos\Phi}. &(90)\end{aligned}$$

The offset $b\sin\delta\cos\Phi_b$ and the amplitude $b\cos\delta\sin\Phi_b$ allow reconstruction of b; the error depends on knowledge of the star coordinate δ and of the baseline alignment angle Φ_b.

If b is the only variable assumed unknown, a least squares fit of b to a series D_i of measurements at hour angles h_i is

$$b=\frac{\sum_i^N D_i[\sin\delta\cos\Phi_b+\cos\delta\sin\Phi_b\cos(h_i-h_0)]}{\sum_i^N[\sin\delta\cos\Phi_b+\cos\delta\sin\Phi_b\cos(h_i-h_0)]^2}. \tag{91}$$

The variance (error) obtained in b this way is

$$\sigma_b^2=\sigma_D^2\left(\frac{\sum_i^N[\sin\delta\cos\Phi_b+\cos\delta\sin\Phi_b\cos(h_i-h_0)]}{\sum_i^N[\sin\delta\cos\Phi_b+\cos\delta\sin\Phi_b\cos(h_i-h_0)]^2}\right)^2 \tag{92}$$

where σ_D^2 is the variance in each individual D_i, assumed to be uncorrelated between and the same for all measurements made. [The $\sum_i\cos(h_i-h_0)$ will not average to zero mean because the statistics of observations is biased towards arcs of star positions above the horizon.]

If the time base h_0 is another fitting variable, the least squares fit to both b and h_0 involves solutions of two non-linear equations and can proceed iteratively as proposed in [136, p. 133]. The error propagation of the results obtained for such a Fourier analysis has been discussed in [168, §7.04] and [73, 153].

D.3 Diurnal Differential OPD

D.3.1 Projection on polar and equatorial axes

If we write down (86) for two stars with coordinates δ_i and α_i, the differential OPD becomes a sinusoidal function of time t, too,

$$\Delta D = (\mathbf{s}_1 - \mathbf{s}_2)\cdot \mathbf{b} \equiv o + p\cos(\omega_L t + \varphi_0), \tag{93}$$

with a coordinate offset/base of o, a daily amplitude p, and a squared daily amplitude of

$$p^2 = \left[\cos^2\delta_1 + \cos^2\delta_2 - 2\cos\delta_1\cos\delta_2\cos(\alpha_1-\alpha_2)\right]\left[b_y^2 + (b_x\sin\Phi - b_z\cos\Phi)^2\right] b^2. \tag{94}$$

The second factor, depending on the baseline length b, its components $b_{x,y,z}$ and the geographical latitude Φ, is the square of the vector $b(b_x\sin\Phi, b_y, -b_z\cos\Phi)$, the equatorial component of the baseline vector. The first factor, which characterizes the star position and separation, can be expanded for small $\Delta\delta \equiv \delta_2 - \delta_1$ and small $\Delta\alpha \equiv \alpha_2 - \alpha_1$:

$$\begin{aligned}
&\cos^2\delta_1 + \cos^2\delta_2 - 2\cos\delta_1\cos\delta_2\cos(\alpha_1-\alpha_2)\\
&\quad\approx \sin^2\delta_1(\Delta\delta)^2 + \cos^2\delta_1(\Delta\alpha)^2 + \cos\delta_1\sin\delta_1\Delta\delta[(\Delta\delta)^2-(\Delta\alpha)^2]\\
&\qquad -\frac{1}{2}\cos^2\delta_1(\Delta\delta)^2(\Delta\alpha)^2 + \frac{1}{3}(\Delta\delta)^4[\frac{3}{4}\cos^2\delta_1 - \sin^2\delta_1] - \frac{1}{12}\cos^2\delta_1(\Delta\alpha)^4 + \ldots
\end{aligned} \tag{95}$$

The cosine of the star separation of (54) is

$$\begin{aligned}
\cos\tau &= \cos\delta_1\cos\delta_2\cos(\alpha_1-\alpha_2) + \sin\delta_1\sin\delta_2 &(96)\\
&\approx 1 - \frac{1}{2}(\Delta\delta)^2 - \frac{1}{2}\cos^2\delta_1(\Delta\alpha)^2 + \frac{1}{2}\cos\delta_1\sin\delta_1(\Delta\alpha)^2\Delta\delta + \cdots &(97)
\end{aligned}$$

in these coordinates, and time-independent. Comparison of (95) with (97) using (49), ie, the additional factor $\sin^2\delta_1$ in (95), shows that this factor in p^2 measures the equatorial component of τ. The time-independent term o (“daily mean”) of ΔD is read off (86) setting the terms $\propto \cos h$ and $\propto \sin h$ to zero:

$$o = b[b_x\cos(\Phi) + b_z\sin(\Phi)][\underbrace{\sin\delta_1 - \sin\delta_2}_{-\cos\delta_1\Delta\delta + \frac{1}{2}\sin\delta_1(\Delta\delta)^2 + \cdots}], \tag{98}$$

and non-zero in general (see Fig. 45). It measures a product of polar components of the baseline and the star separation [167][145, App A]. The phase φ_0 in (93) is

$$\begin{aligned}
\frac{o}{b}\cos\varphi_0 &= [-b_x\sin\Phi + b_z\cos\Phi][\cos\delta_1\cos\alpha_1 - \cos\delta_2\cos\alpha_2] - b_y[\cos\delta_1\sin\alpha_1 - \cos\delta_2\sin\alpha_2], &(99)\\
-\frac{o}{b}\sin\varphi_0 &= [-b_x\sin\Phi + b_z\cos\Phi][\cos\delta_1\sin\alpha_1 - \cos\delta_2\sin\alpha_2] + b_y[\cos\delta_1\cos\alpha_1 - \cos\delta_2\cos\alpha_2] &(100)
\end{aligned}$$

D.3.2 24 hrs Fit

For any sequence of DOPD observations ΔD_i at points t_i in time, (93) can be fitted with three parameters o, p and φ_0 in the least squares sense:

$$\sum_i [p\cos(\omega_L t_i + \varphi_0) + o - \Delta D_i]^2 \longrightarrow \min . \tag{101}$$

Explicit notation of the partial derivatives does not make much sense here, but since the system of 3 equations that follows is linear in p and o, the numercial solution is straight forward (and already implemented in the pipeline coding). The error analysis—the dependence of $\epsilon(p)$ and $\epsilon(o)$ on noise $\epsilon(\Delta D_i)$—leads to a linear problem; the result of such statistics is summarized in Table 14 assuming that the point measurements have been made at equidistant time intervals, $t_{i+1} - t_i$=const shown in the second column (which may not be the optimum scheduling [160]), and have been started at a phase φ_0 (first column) measured in hours from the point of maximum ΔD.

Start φ_0 (h)	Det. Int. (s)	# Det. Int.	Obs. Block (h)	$\epsilon(p)/\epsilon(\Delta D)$	$\epsilon(o)/\epsilon(\Delta D)$
0	1	3600	1	6.5	6.5
3	1	3600	1	4.0	6.5
6	1	3600	1	0.88	6.5
0	2	1800	1	9.1	9.2
3	2	1800	1	5.6	9.2
6	2	1800	1	1.2	9.2
0	4	3600	4	0.36	0.40
3	4	3600	4	0.12	0.40
6	4	3600	4	0.21	0.40
6	1	14 400	4	0.11	0.20

Table 14: The errors $\epsilon(p)$ and $\epsilon(o)$ of the 24 hrs fits to the diurnal motion (101) in units of the error $\epsilon(\Delta D)$ of the individual point measurements, as a function of starting point φ_0 on the periodic curve, measured in units of hours, as a function of the distance between two measurements (in seconds), and total number of point measurements. The column headed “Obs. Block” is simply the product of the number of measurements and the stride between the measurements.

The fourth column, the total time spent on the observation, is in this case generally limited to typically 9 hrs (the length of the night), and in practise limited by scheduling policies on the mountain. The first group of table entries shows that observation for 1 hour with a total of 3600 point measurements generates an error in the fitted offset o which is approximately 6 times the error of the individual measurements of ΔD. The error in the fitted amplitude p depends on whether this hour is scheduled during an extremum of the curve (yielding an error in p of the same order) or closer to the point of transversing the offset point. The second group of entries in Table 14 shows how the error is inversely proportional to the square root of the number of point measurements—doubling the distance between the point measurements to 2 seconds. The third group of entries demonstrates that the errors can be greatly reduced if the observation scans a period of 4 hours such that it is able to sense the variable slope of the sinusoidal function.

The application of this error analysis for the baseline C3–J4 in Fig. 45 would look as follows: The DOPD has an amplitude $p = 807$ μm (stroke from -1207 μm to +409 μm) with a maximum at $\varphi_0 \approx 15.96$ hours and an offset of $o = -399$ μm. If we observe this 3 hours later for 1 hour (second line in Table 14) with an error $\epsilon(\Delta D) = 300$ nm in each of the 3600 measurements of the DOPD, we will be able to fit p with an accuracy of 4×300 nm=1.2μm or a relative error of $1.2/807 \approx 1.5 \cdot 10^{-3}$. Assuming no error in the equatorial component of the baseline vector, we have measured $\sin\delta\Delta\delta$ in (95) to a relative precision of $1.5 \cdot 10^{-3}$. The δ component of the star separation has been determined with a relative accuracy of $1.5 \cdot 10^{-3}$, here with an absolute accuracy of 1.1 mas since the star separation $\Delta\delta$ was $0.7''$ in this example.

The main strategical difference in comparison to the use of (59) is

- The period fitting approach includes the determination of the "metrology zero," the origin of the ΔD coordinate system, if the fitted o is discarded, whereas the use of (59) needs a calibrated ΔD.
- The period fitting approach yields two components of τ, whereas (59) is a scalar equation which generates an estimate of τ multiplied with the trigonometric expression in the denominator (projection of the star separation onto the projected baseline vector). Essentially, Fig. 44 plays no immediate role for the fitting approach, since the orientation angle itself has become an (implicit) fitting parameter.

D.4 Dependencies

D.4.1 Error terms effected by this

Error term	Relevant subsection
Wavefront amplitude and phase fluctuations above M1	5.3
Effect of aberrations in image plane optical components	14.3
Effect of aberrations in pupil plane optical components	16.3
Galactic effects	31.3
Solar System effects	30.3

D.5 Detailed contributions

D.5.1 Baseline Length Calibration

The estimated error σ_b in the baseline length obtained by the 1-parametric least squares fit (91) after visiting N stars on the sky that are rather homogeneously distributed in the range $z < 60$ deg is shown in Figure 53: If the position of the stars is known to $\sigma_a = 0.2''$, measuring $N \approx 5$–7 of them achieves an accuracy of ≈ 40 μm for $b = 100$ m; if the accuracy is only $\sigma_a = 0.4''$, one must measure $N \approx 30$ for the same goal. Figure 54 uses a more constrained region of the sky with $z < 40$ deg and achieves inferiour accuracy for equivalent numbers of stars. (AT tests cover $z < 50$ deg [86]). Global fits to both heuristic data sets are

$$\sigma_b \approx 462.3\mu\mathrm{m}\,\sigma_a/''/N^{0.43839} \quad , \quad z < 60^\circ, \tag{102}$$

$$\sigma_b \approx 1206\mu\mathrm{m}\,\sigma_a/''/N^{0.5813} \quad , \quad z < 40^\circ. \tag{103}$$

assuming that the error in D remains negligible.

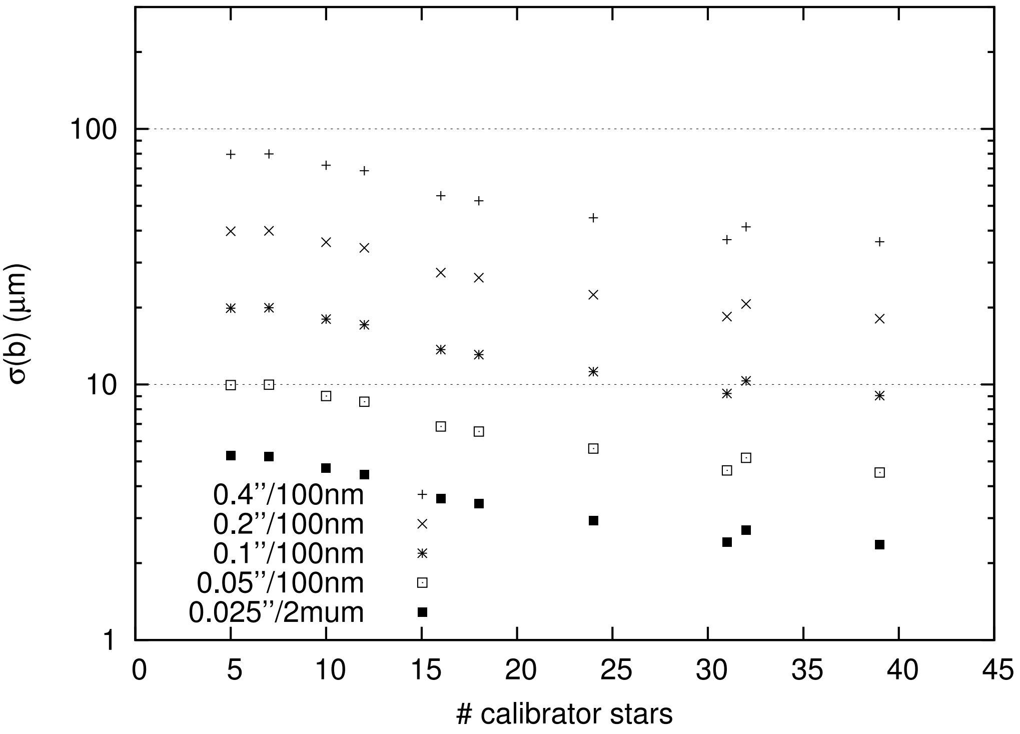

Figure 53: The error σ_b to a baseline length $b = 100$ m from a least-squares fit to N measured delays D for N stars, $N \geq 5$, with errors of $\sigma_D = 100$ nm or $\sigma_D = 2$ μm. The N positions have been rather homogeneously distributed over the sky in the zenith range $z < 60°$, taking subsets of the Hardin-Sloan-Smith points [76], and have been displaced by angles with five different Gaussian widths between $0.025''$ and $0.4''$ to simulate imprecise knowledge of their positions in the sub-arcsec range. ($0.02''$ is the expected tracking error [44, §6.2] and also the maximum K band splitting by the TAD [119].)

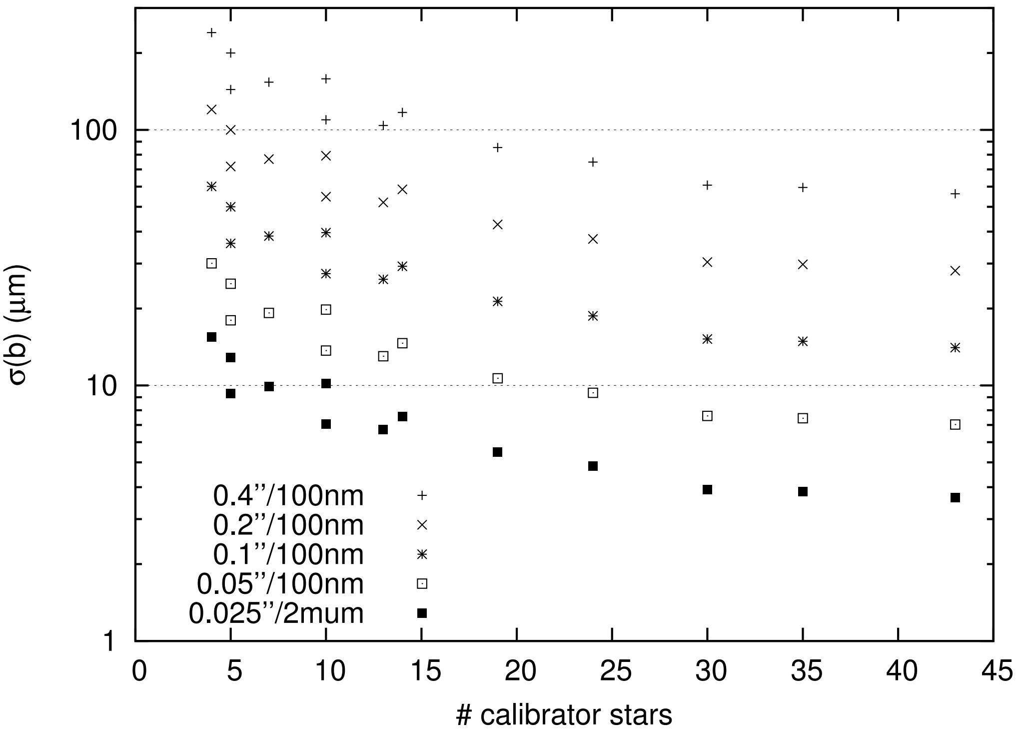

Figure 54: The errors of Figure 53 if only baseline calibrator stars in the zenith range $z < 40°$ are used.

D.5.2 Baseline Vector Calibration

The calibration in the previous section considered a model of a baseline vector attached to a precisely clocking "reference frame." It assumes that neither the motions of App. C nor the baseline pointing direction need calibration and ends up in one free parameter b. The full baseline vector contains three coordinates, so the next more complex situation is calibration of all of these.

Fig. 55 are results of a least squares fit of the 3 degrees of freedom of the baseline vector to a series of delay measurements. Technically speaking, this has been done by writing (86) as

$$b_x = \cos\phi\cos a; \quad b_y = \sin\phi\cos a; \quad b_z = \sin a, \tag{104}$$

minimizing $\sum_i^N [D_i - \mathbf{s}_i \cdot \mathbf{b}]^2$ in the least squares sense over a set of "noisy" star positions A_i and z_i and building a r.m.s. statistics over the variables b, ϕ and a. The accuracy in the baseline length b is the same as obtained with the 1-parameter fits of Fig. 53.

The elevation angle a (tilt of the baseline versus the horizontal) is obtained with double the accuracy of the azimuth angle ϕ. The interpretation of this bias is: the even distribution of the calibrator stars along azimuths and their clumpy, "overhead" distribution along zenith angles means that a measurement via the projections D achieves low resolution along the horizontal for the two subsets of stars in the two opposite pointing directions of the baseline [132, Fig 2-8]. The coupling along the vertical coordinate is simply stiffer on the average, and the information contained in the delays better distributed to deduce the baseline tilt versus the horizon than the baseline rotation around the zenith.

The unbalanced accuracy in the three Cartesian baseline coordinates after fitting a set of measured delays to the baseline vector does not have a negative impact, since the application of the coordinates attained from the baseline calibration (ie, the interpretation of measured delays for known baseline back to sky coordinates) follows a reciprocity theorem for the statistics of the errors in sky and baseline parameters: the errors in the baseline reflect in a statistical sense the errors in the calibrator's positions (that I choose to be the same for all calibrators and homogeneous in the tangential plane at the sky coordinate). The differences in the knowledge of the baseline coordinates mean that *no* bias in terms of star azimuth or elivation exists when delays of "science" objects are interpreted based on calibrated baselines.

The baseline vector calibration is in a general sense equivalent to determining the geographic longitude and latitude of either the head or the tail of the baseline vector: one can change the orientation of the baseline by either tilting it explicitly or keeping it always horizontal and sliding it with the tangent plane across the earth surface. Introducing the geographical latitude Φ or longitude λ as additional fitting parameters into the minimization procedure would define an ill-conditioned problem.

D.5.3 Seismic Activity

A general overview of earthquakes in Chile is given by `http://www.eso.org/gen-fac/pubs/astclim/earthqua` and `http://www.eso.org/paranal/site/paranal.html#GeoInfo`. Intensity spectra have been provided in Section 3.7.6 and 9.3 of [147].

There seems to be no study to correlate the changes in the VINCI baselines with seismic activity or with VLTI rail alignment activities. From that perspective, the frequency of baseline re-calibrations related to repositioning of the mountain foundation or the concrete after earthquakes is unknown.

There seem to be no plans to feed the data of the seismic monitoring system [80] into the ASM to

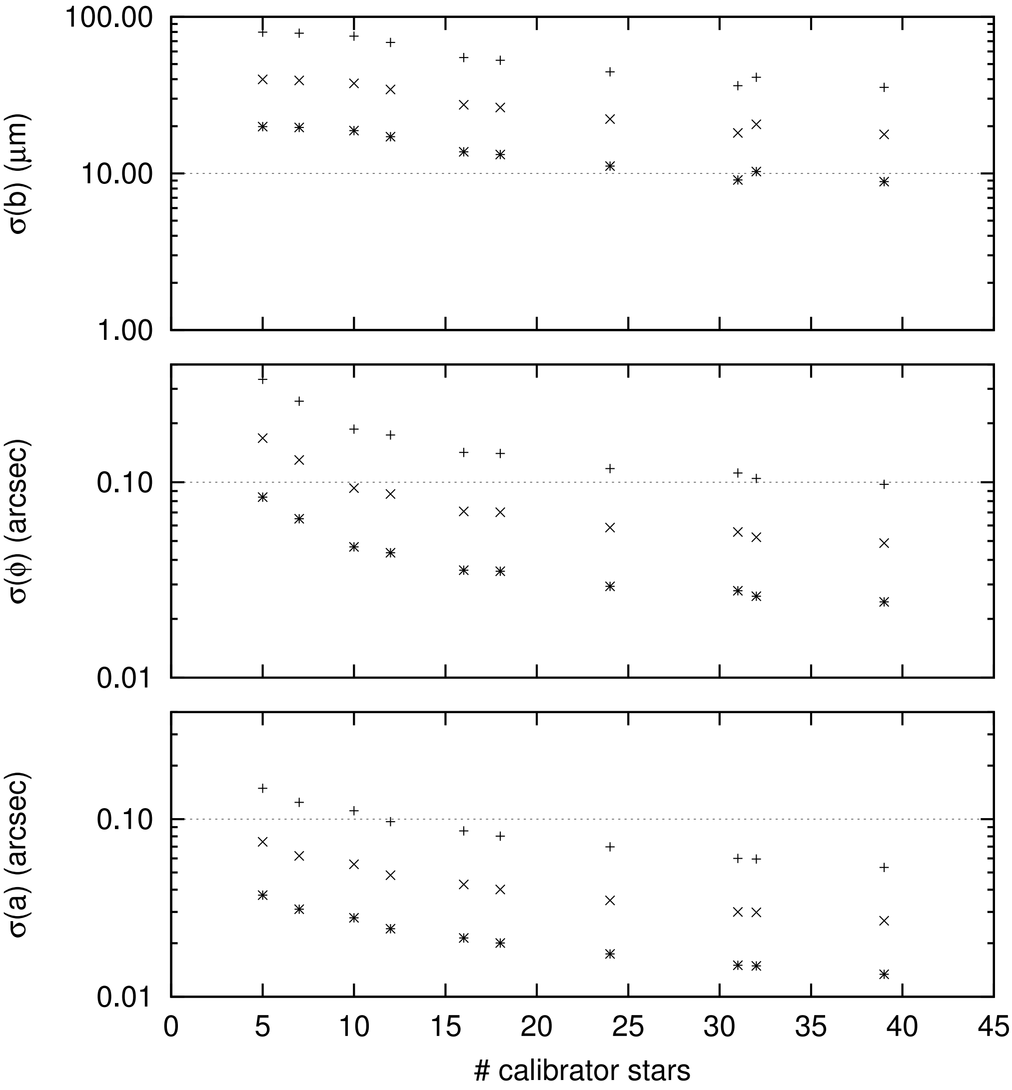

Figure 55: The error σ_b to a baseline length $b = 100$ m, to the baseline orientation in the horizontal σ_ϕ, and to the baseline orientation in the vertcial σ_a from a 3-parametric least-squares fit to N measured delays D of $N \geq 5$ calibrator stars, assuming no errors in the measured delay. The N positions have been rather homogeneously distributed over the sky as in Fig. 53 in the zenith range $z < 60°$, and have been randomly displaced by angles with different Gaussian widths of $0.4''$ (plusses), $0.2''$ (crosses) or $0.1''$ (stars) to simulate imprecise knowledge of their positions in the sub-arcsec range. $0.1''$ over $b = 100$ m is equivalent to 48 μm sideways.

allow a a posteriori analysis of VLTI baseline solutions in terms of seismic activities.

D.6 Impact on astrometry

Repointing the telescope axis to each calibrator star may cost up to 3 minutes if the sequence is not optimized to shorten the path in the "traveling salesman" style [86, §7.2]. Additional time is spent on closing the tracking loop at the Coudé focus, then acquiring the star by the fringe tracker.

E LARGE SCALE STRUCTURE IN THE ATMOSPHERE ABOVE PARANAL

E.1 Introduction

E.2 Dependencies

E.2.1 This error term is effected by

Error term	Relevant subsection

E.2.2 Error terms effected by this

Error term	Relevant subsection
Systematic effects from the atmosphere	26.3
Air flow through the VLTI	B.3
Atmospheric scintillation and thermal background fluctuations	25.3
VLTI baseline geometry	11.4

E.3 Detailed contributions

E.3.1 Wind velocity profile

E.3.2 Ground level temperature, humidity and pressure fluctuations

E.3.3 CN-squared profile from air density fluctuations

E.3.4 CN-squared profile from humidity fluctuations

E.3.5 CN-squared power spectrum and outer scale

E.3.6 CN-squared spatial intermittency

E.3.7 Timescale for evolution of turbulence within each layer

oOo